Volume 8, Number 1, Winter 2022

ACERP
Advanced Ceramics Progress

ISSN 2423-7477
e-ISSN 2423-7485

Advanced Ceramics Progress

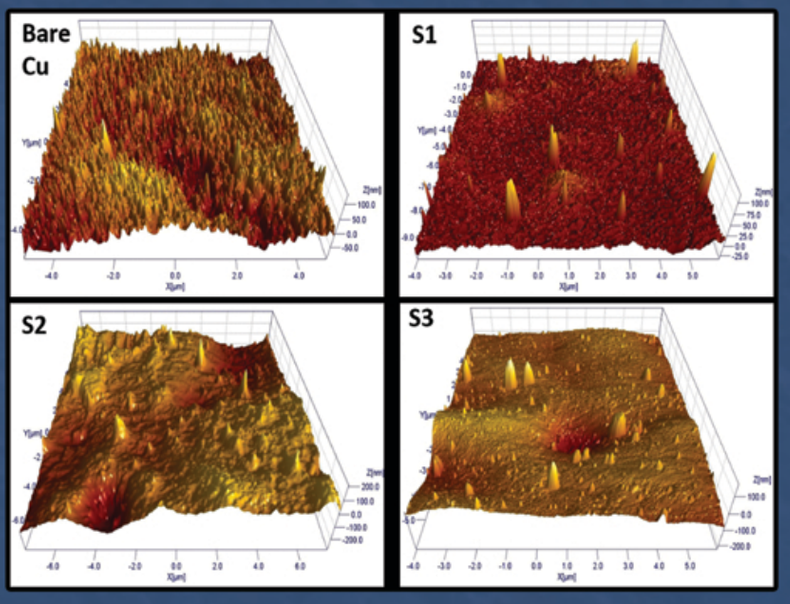

Materials and Energy
Research Center

Iranian Ceramic Society

In The name of God

Advanced Ceramics Progress

DISCLAIMER

The publication of articles in Advanced Ceramics Progress does not imply that the editorial board, editorial advisory board, reviewers or the publisher accept, approve or endorse the data and conclusions of authors.

Advanced **Cer**amics **P**rogress (ISSN 2423-7477) (e-ISSN 2423-7485)
Web Site: www.acerp.ir, E-mail: office@acerp.ir
Tel: +98 (0) 26 36280040-7 ext.: 382, Fax: +98 (0) 26 36201888
Tel:+98 (0)21 88771626-7 ext.: 8931, Fax: +98 (0)21 88773352
Materials and Energy Research Center (MERC); Iranian Ceramic Society (ICERS)

ISSN: 2423-7477; e-ISSN: 2423-7485

Advanced Ceramics Progress: Vol. 8, No. 1, (Winter 2022) 1-55

CONTENTS

Advanced Ceramics Progress: Vol. 8, No. 1, (Winter 2022) 1-8

Materials and Energy Research Center
MERC

Contents lists available at ACERP

Advanced Ceramics Progress

Journal Homepage: www.acerp.ir

Original Research Article

Synthesis of CuO and CuO/ZnO Composite Powders for Antibacterial, Photocatalytic, and Pigment-Related Applications

Moshkan Dokht Khosravi [a], Mehdi Ghahari [b,*], Mahdi Shafiee Afarani [c], Amir Masoud Arabi [d]

[a] *MSc, Department of Materials Engineering, Faculty of Engineering, University of Sistan and Baluchestan, Zahedan, Sistan and Baluchestan, Iran*
[b] *Associate Professor, Department of Nano Materials and Nano Coatings, Institute for Color Science and Technology (ICST), Tehran, Tehran, Iran*
[c] *Professor, Department of Materials Engineering, Faculty of Engineering, University of Sistan and Baluchestan, Zahedan, Sistan and Baluchestan, Iran*
[d] *Associate Professor, Department of Inorganic Pigments and Glazes, Institute for Color Science and Technology (ICST), Tehran, Tehran, Iran*

* Corresponding Author Email: maghahari@icrc.ac.ir (M. Ghahari)

URL: https://www.acerp.ir/article_147533.html

ARTICLE INFO

Article History:

Received 15 February 2022
Received in revised form 17 March 2022
Accepted 5 April 2022

Keywords:

CuO/ZnO Composite
Surfactants
Chromatic Characterization
Antibacterial
Photocatalytic Activity

ABSTRACT

Incorporation of CuO into ZnO contributes to the formation of CuO/ZnO composite, thus enhancing some properties of individual oxides such as antibacterial and photocatalytic activities. The current study evaluated the effect of both synthesis and in-situ syntheses of copper oxide on the zinc oxide particles using Copper(II) nitrate trihydrate as the starting material as well as acetic acid, D200, SHMP, PVP, CTAB, SDS, urea, and M2P surfactants. The impact of surfactants on the microstructure and chromatic properties of the samples was also investigated. The results from scanning electron micrographs showed different morphologies of copper oxide particles in the forms of needle, round, and flake depending on the type of surfactant. Moreover, the chromatic properties of the powders showed that the pigment synthesized in the presence of SHMP was in a better and darker black color than the others. Further, copper oxide powders exhibited more proper anti-bacterial behavior than the copper oxide/zinc oxide composite powders. In addition, copper oxide/zinc oxide particles had higher photocatalytic activity (up to 95 %) than copper oxide powders (about 65 %).

https://doi.org/10.30501/acp.2022.329820.1082

1. INTRODUCTION

The increasing growth of population has negatively affected water quality by releasing a variety of pollutants into water sources. It is predicted that more than 50 % of the countries around the globe will face water crisis by 2025 [1]. Different pollutants such as heavy metal ions, organic dyes, industrial wastes, pesticides, and pharmaceutical wastes are considered seious threats to water quality. This is the reason why application of efficient water purification technologies such as photocatalysis, electrochemical treatment, membrane filtration, ozonation, and flocculation for water treatment have gained significance. For a long time, photocatalysis has used as a simple and efficient technique for water purification. Nowadays, using composite materials has

Please cite this article as: Khosravi, M. D., Ghahari, M., Shafiee Afarani, M., Arabi, A. M., "Synthesis of CuO And CuO/ZnO Composite Powders for Antibacterial, Photocatalytic and Pigment-Related Applications", ***Advanced Ceramics Progress***, Vol. 8, No. 1, (2022), 1-8. https://doi.org/10.30501/acp.2022.329820.1082

significantly contributed to developing highly efficient materials and removing a wide range of pollutants [2].

Synthesis, coating, and fabrication of copper (II) oxide and copper (I) oxide materials have considerably drawn researchers' attention in the last decades due to their numerous applications. They are employed in different fields of ceramic applications such as producing inks for FET transistors [3], antibacterial materials for medical and biological applications [4-6], solar cells [7-9], gas sensors [10,11], electrochemical sensors [12,13], photocatalysts [14-16], and pigments [17].

Copper oxide was synthesized through several methods such as thermal decomposition [18,19], sonochemical [20,21] and hydrothermal [22,23], milling [24,25], electrodeposition [26,27], ultrasonic spray pyrolysis [25,28], solution combustion [25,29], electrochemical oxidation [30], and precipitation [28,31]. The precipitation method as an easy-eco route was employed to prepare copper oxide particles in many studies. Several investigations evaluated the effects of different surfactants on the microstructure and properties of copper oxide particles [32]. Of note, addition of CuO to ZnO can form CuO-ZnO composite that increases the particle size and decreases the bandgap energy. In other words, the higher the concentration of CuO in the composite, the smaller the bandgap energy. It can also increase the stability of the photocatalytic reaction and radical species such as superoxide anion radical ($^{\bullet}O^{2-}$), ($HO_2^{\bullet}$) and (HO_2^-) which can inhibit the growth of bacteria [33]. Some researchers have evaluated the effects of antibacterial and photocatalytic properties of CuO/ZnO composites on different pollutants under UV or visible irradiation [2].

The main objective of the current study was to synthesize copper oxide and copper oxide/zinc oxide composite particles based on the precipitation method in the presence of different surfactants. To the best of the authors' knowledge, the effect of these surfactants on the morphology of CuO/ZnO particles was investigated for the first time. In this regard, the structure, microstructure, and antibacterial and optical properties of the powders were examined. In addition, the photocatalytic properties of the synthesized composite were studied on DR23 dye for the first time.

2. MATERIALS AND METHODS

CuO and CuO/ZnO composite powders were synthesized using Copper (II) nitrate trihydrate ($Cu(NO_3)_2.3H_2O$, Merck), Manganese (II) acetate tetrahydrate ($Mn(CH_3COO)_2{\cdot}4H_2O$, Merck), Zinc nitrate hexa-hydrate ($Zn(NO_3)_2.6H_2O$, Merck) as the starting materials. In addition, Glycine ($C_2H_5NO_2$, Merck) and Glucose ($C_6H_{12}O_6$, Merck) were used as the fuels. Moreover, Cetyl trimethyl ammonium bromide ($((C_{16}H_{33})N(CH_3)_3]Br$, CTAB, Merck), Polyvinyl-pyrrolidone ($(C_6H_9NO)_n$, PVP, Rahavard Tamin Pharmaceutical Co.), Sodium hexametaphosphate ($(NaPO_3)_6$, SHMP, Dai Viet Chem), Sodium dodecyl sulfate ($NaC_{12}H_{25}SO_4$, SDS, Merck), acetic acid (CH_3COOH, Merck), Urea (CH_4N_2O, Merck), Acrylic homopolymer (D200, MW=5000, Simab Rezin Co.), dispersants (MP, ICST), Anionic PEG acrylate homopolymer dispersants (M2P, ICST) were used as the surfactants.

Copper oxide powders were synthesized through the precipitation method in the presence of different surfactants. To this end, first, 0.97 g copper nitrate tri-hydrated and 0.0194 g Manganese acetate tetra-hydrate (0.02 wt. % of Cu precursor) were dissolved in 250 mL water. Then, the surfactants were added to the solution and agitated under magnetic stirring to dissolve completely. The weight ratio of the surfactant to copper precursor was assumed to be 1:2. Next, NaOH solution (1 molar, Merck) was added drop wise to the solution up to the pH adjustment of 9 and mixed for 15 min followed by more heating at 100 °C for an hour until a black precipitate was obtained. Finally, the obtained sample was washed three times and dried at 100 °C in an electric oven for one hour.

Zinc oxide particles were synthesized through solution combustion synthesis method. To this end, first, 5 g zinc nitrate hexahydrate, 1.15 g glucose, and 0.1 g glycine were dissolved in 20 mL deionized water under magnetic stirring. The transparent solutions were heated at 80 °C under magnetic stirring until yellowish gel-like precipitates were obtained.

The combustion reaction of samples occurred in a commercial microwave oven (SAMSUNG) with the frequency of 50 Hz and power of 900 W for one min, and spongy-foam like agglomerated particles were obtained. To complete the reaction and remove the residual organic matters, the samples were transferred to an electric furnace and calcined (post-heated) at 500 °C at the soaking time of one hour and heating rate of 10 °C min^{-1}.

The mentioned CuO synthesis process was repeated in the presence of synthesized ZnO particles to obtain CuO/ZnO composite. All other synthesized processes are similar to those of CuO synthesis.

The microstructure and structural characteristcs of the samples were identified using Scanning Electron Microscopy (SEM, LEO 1455 VP) and XRD (Siemens D-500) methods. The mean particle size of the powder samples was determined using an image processing software, i.e., ImageJ 1.44p.

The mean diameter ($d_{Scherrer}$) of zinc aluminate (gahnite) crystallite was determined considering the half-height width (β) of the (311) diffraction peak of gahnite using Scherrer equation ($d_{Scherrer}=0.9\lambda/\beta\cos\theta$). In addition, WQF-510 FT-IR (RAYLEIGH) Spectrometer was used to study the bonding structures. Photoluminescence (PL) studies were conducted using a

PerkinElmer LS 55 Fluorescence Spectrometer (phosphorescence mode) with the exciting wavelength of 360 nm. Chromaticity color index (CIE) calculations were performed based on the photoluminescence spectra using MATLAB programming.

Broth microdilution method was used in the anti-bacterial tests with E. coli and S. aureus bacteria which were Gram-negative and Gram-positive, respectively.

The photocatalytic activities of the prepared CuO and CuO/ZnO powders were evaluated based on the degradation of Direct Red 23 (RD23) under UV light source in a prototype photocatalytic agitated reactor. Suspensions were prepared by adding 0.4 g of the synthesized powders to 500 mL standard solution of DR23 with the concentration of 20 mg/L. First, suspensions were kept in a dark medium under agitating for 30 min to complete the absorption/desorption process. Then, the DR23 photodegradation yield was obtained during 210 min of suspension irradiation. Photodegradation reactions occured in a 500 mL volumetric glass where a transparent silica glass tube containing a 15 Watt UV lamp was located. The suspension was agitated by a magnet stirrer rotating at 500 rpm during the test. Two mL of suspensions were obtained at each 15 min interval, and their absorbency was measured using a UV–vis spectrophotometer (Perkin-Elmer Lambda 25) at the maximum absorption wavelength of 503 nm.

3. RESULTS AND DISCUSSION

Figure 1 depicts the XRD patterns of the synthesized copper oxide and copper oxide/zinc oxide powder samples. As shown in this figure, copper oxide powder contained CuO phase characterized by a monoclinic structure (card no. 01-080-1916). Apparently, NaOH and surfactant function locally as a redox in the synthesis process that leads to the Cu_2O minor phase. Moreover, ZnO with wurtzite structure (card no.01-076-0704) was formed in addition to these phases in copper oxide/zinc oxide composite powder samples.

Figures 2 (a-h) show the SEM micrographs of copper oxide particles synthesized in the presence of different surfactants. As shown in Figures 2 (a-b), the presence of acetic acid and D200 surfactants contributes to the formation of highly agglomerated particles. Moreover, some spherical nanoparticles of the particle sizes of 50-70 nm were formed.

In comparison with the synthesis of case in the presence of acetic acid and D200, synthesis in the presence of Sodium Hexametaphosphate (SHMP) led to formation of very fine spherical particles with less agglomeration (Figure 2(c)). In addition, PVP and CTAB surfactants made the synthesis of particles with flake-like microstructures (Figures 2 (d-e)) feasible. Moreover, synthesis in the presence of amine containing surfactants, i.e., SDS, urea, and M2P, resulted in a combination of needle- and flake-shaped morphologies, as illustrated in Figures 2 (f-h), respectively.

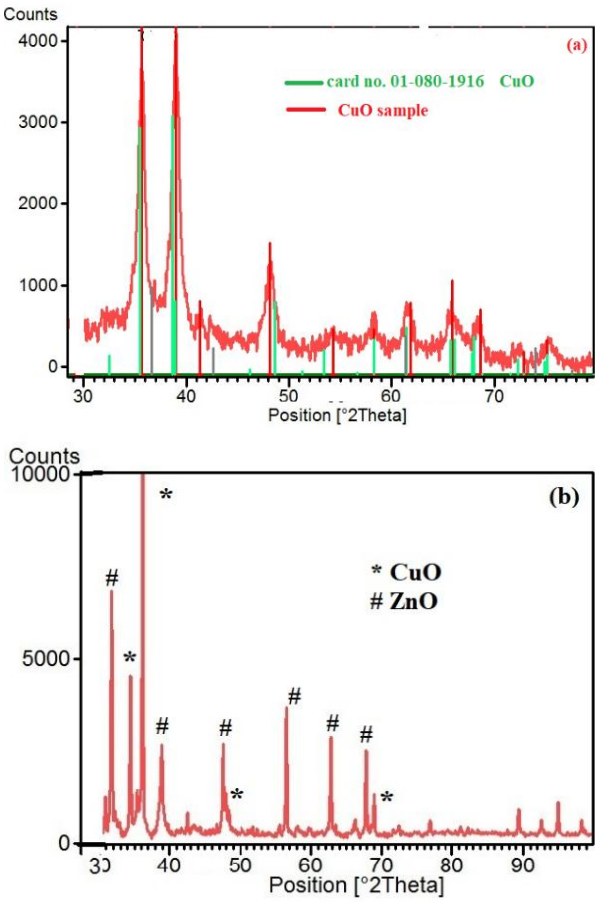

Figure 1. XRD pattern of the synthesized copper oxide (a) and (b) copper oxide/zinc oxide powders

Figure 3 presents the macro images of the synthesized particles using different surfactants. Based on these images, darker powders were selected for chromatic characterization (Table 1). Powder samples synthesized in the presence of SHMP surfactant are shown in darker colors than the other ones.

The anti-bacterial properties of ZnO/CuO composite and CuO powders synthesized in the presence of SHMP surfactant were studied using two E. coli and S. aureus bacteria. Table 2 lists the MBC values where both CuO and CuO/ZnO composite materials affect the S. aureus bacteria. However, the CuO samples failed in properly elimintaing the E. coli bacteria. Malwal et al. pointed out to the effect of ZnO/CuO composite on S. aureus instead of E. coli [2]. Sakib et al. reported that upon increasing the amount of CuO in ZnO/CuO composites, the antibacterial activities of both bacteria would increase [34].

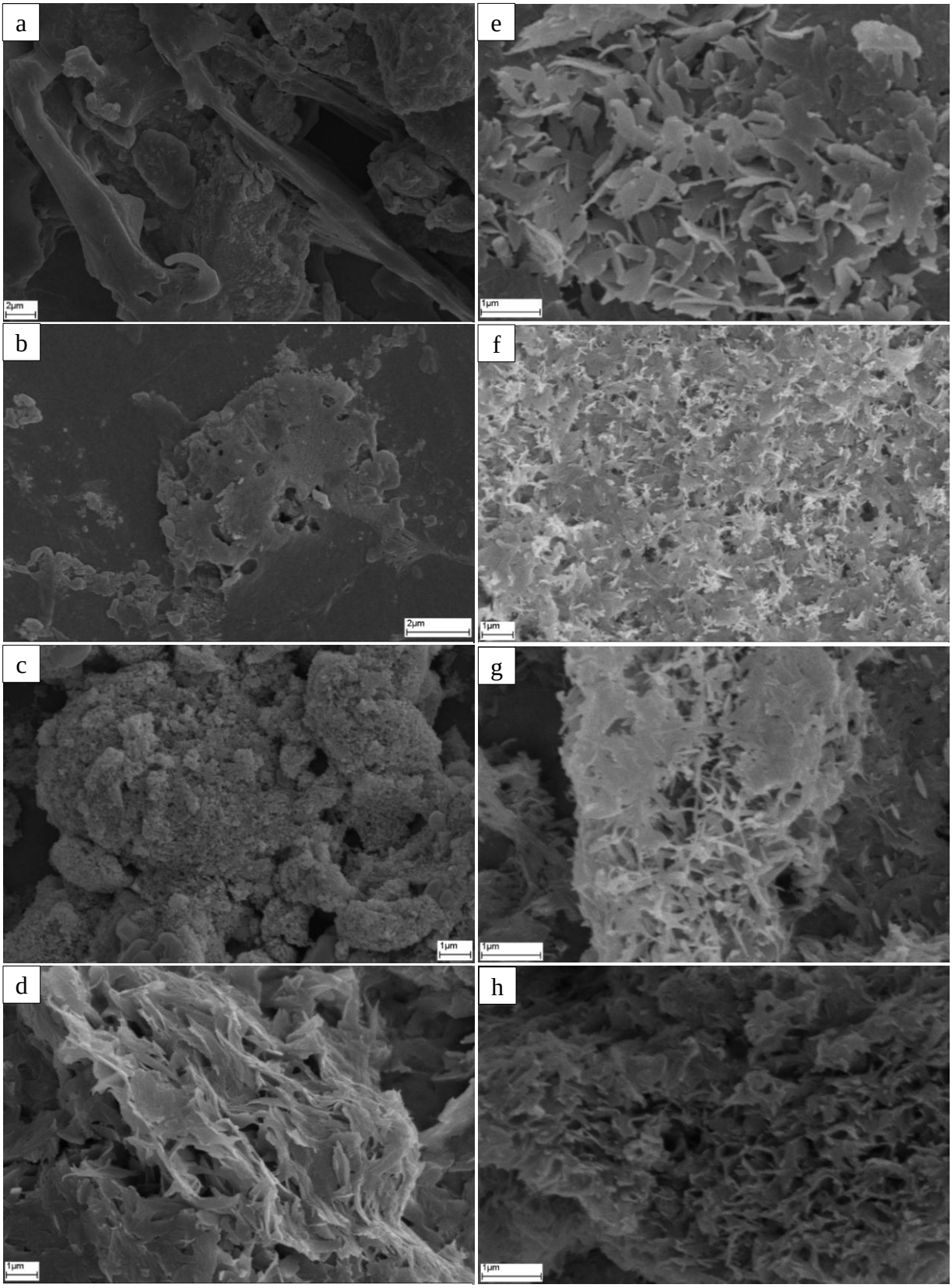

Figure 2. SEM micrographs of the copper oxide particles synthesized in the presence of different surfactants: a) acetic acid, b) D200, c) SHMP, d) PVP, e) CTAB, f) SDS, g) urea, and h) M2P

The composite samples exhibted better performance in terms of removing bacteria than the individual oxide [35]. He et al. remarked that the antibacterial properties of CZ-ESM indicated improvement in their activity against S. aureus and E. coli, compared to single components, mainly due to the synergistic interaction of Zn^{2+} and Cu^{2+} ions [36].

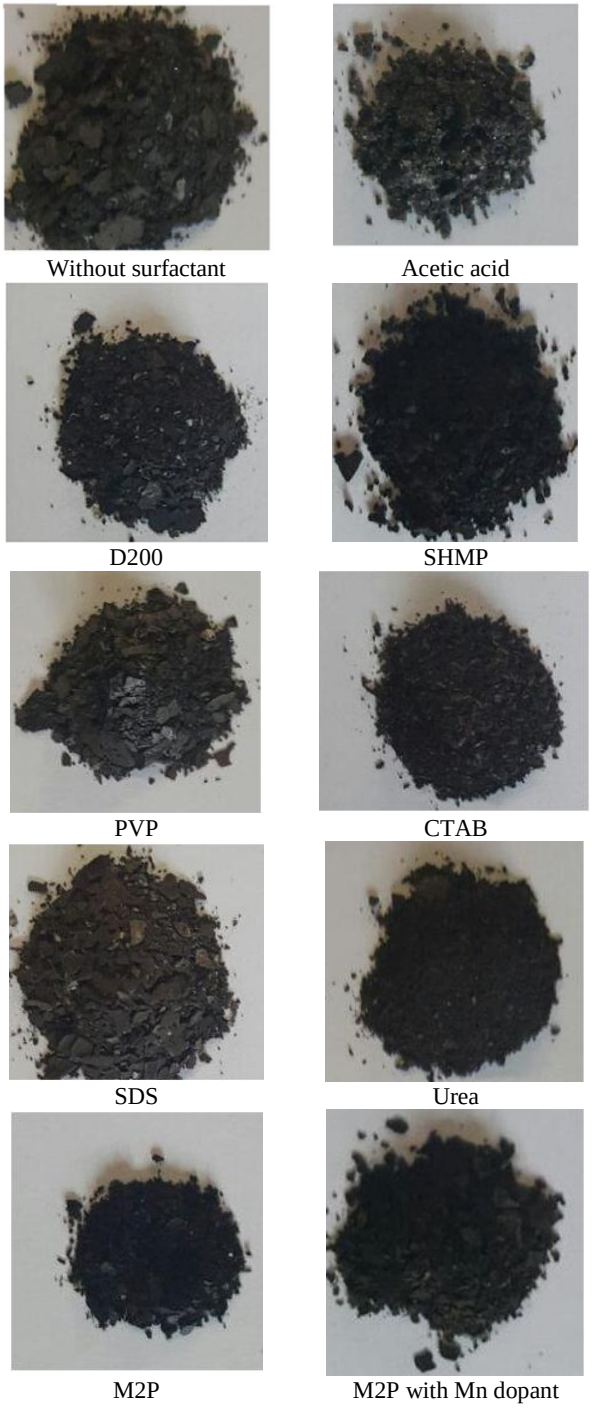

Figure 3. Macro images of synthesized particles synthesized with different surfactants

TABLE 1. Chromatic properties of the samples synthesized in the presence of different surfactants

	L*	a*	b*	c*	h*
M2P with Mn dopant	37.26	-0.34	-0.25	0.43	216.21
M2P	36.31	-0.24	-0.21	0.32	220.37
D200	36.01	-0.34	-0.25	0.42	215.98
SHMP	35.26	-0.06	0.38	-0.38	99.24

TABLE 2. Chromatic properties of the samples synthesized in the presence of different surfactants

Bacteria	S. aureus		E. coli	
	Remained	Yield (%)	Remained	Yield (%)
ZnO/CuO	0	100	0	100
	3.5×10^4	99.5	0	100
	0	100	0	100
CuO	0	100	3.5×10^4	99
	0	100	3.5×10^4	97
	0	100	5.5×10^4	92

Figure 4a shows the concentration changes (C/C_0) of DR23 with pH=9 as a function of illumination time in the reactor under UV irradiation for ZnO/CuO composite and CuO powders synthesized in the presence of SHMP surfactants. The initial 30 min was considered as the dark interval. As illustrated, photocatlitic yield of ZnO/CuO composite powder (about 90 %) was more than that of CuO particles (about 64 %) mainly due to the narrower band gap of CuO (1.2-1.7) than that of ZnO (3.7 eV) [37]. ZnO with a wide band gap can absorb UV irradiation properly and increase photocatalytic activity. The decrease in the DR23 concentration resulting from degradation was taken into account in the kinetic study. Given the low initial concentration of the DR23 solution, the reaction rate can be considered apparently first-ordered, as presented in following equation:

$$\text{Rate} = -dC/dt = K_\alpha C \quad (1)$$

where K_α is the apparent rate constant, and C the concentration of DR23. The kinetic degradation order for the process using CuO and CuO–ZnO composite powders as photocatalysts was calculated by plotting ($Ln(C/C_0)$ versus irradiation time (Fig. 4b). The rate constants of the CuO–ZnO and CuO photocatalysis processes were calculated from the slopes which fitted the first-order kinetic equation ($-Ln(C/C_0)=kt$). According to the findings, CuO and CuO–ZnO samples under UV irradiation represented the constant photocatalytic activity values equal to 0.23×10^{-2} and 1.2×10^{-2} min^{-1}, respectively. P. Muhambihai et al. reported that NiO/CuO composite showed a higher degradation ability on Direct Red 80 dyes than that of ZnO/CuO [38]. Wei et al. also reported that the photocatalytic reduction of Cr(VI) was obtained over the composite films with 0.73 atomic Cu/Zn ratios. The

enhanced activity of CuO/ZnO composite films could be mainly attributed to the efficient separation of charges photogenerated in CuO/ZnO heterostructures [39]. Zhu et al. remarked that the photocatalytic removal efficiency of phenol, in comaparison to that of the CuO/ZnO composite, was up to 78 % under the irradiation of the light, which was ~2 and ~4 times higher than those of the pristine ZnO and CuO, respectively [40].

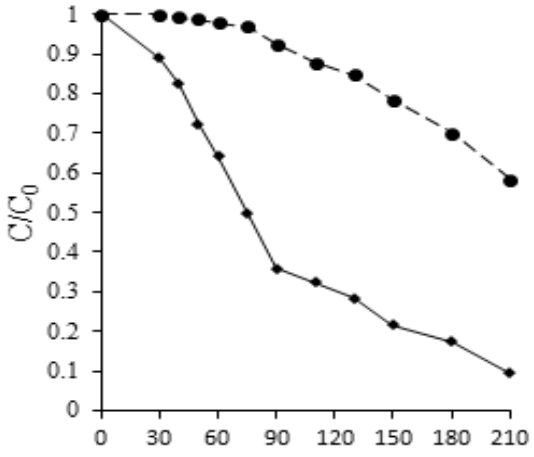

Figure 4. a) concentration changes (C/C_0) and b) -$Ln(C/C_0)$ versus irradiation time of DR23 with pH=9 versus irradiation time UV irradiation for ZnO/CuO composite and CuO powders synthesized in the presence of SHMP surfactants

4. CONCLUSIONS

In the present study, copper oxide and copper oxide/zinc oxide particles were successfully synthesized in the presence of different surfactants to investigate their effect on the morphology of particles. The main results are suammarized in the following:

1) Copper oxide powders with different morphologies in the forms of needle, round, and flake were synthesized in the presence of acetic acid, D200, SHMP, PVP, CTAB, SDS, urea, and M2P surfactants.
2) The chromatic properties of the powders indicated that the pigment synthesized in the presence of SHMP had a better and darker black color than that of the others. Therefore, it could be a suitable candidate for the black pigment in the ceramic industry.
3) Copper oxide powders exhibted a more proper anti-bacterial behavior than copper oxide/zinc oxide powders in dealing with S. aureus bacteria. However, ZnO/CuO composite was more effective than CuO in removing E. coli bacteria.
4) Copper oxide/zinc oxide particles demonstrated higher photocatalytic activity than copper oxide powders.

ACKNOWLEDGEMENTS

The acknowledgment section helps identify the contributors responsible for specific parts of the research. It lists authors, non-authors, funding sources, editing services, or even administrative staff. It should only mention people directly involved with the research.

REFERENCES

1. Thavasi, V., Singh, G., Ramakrishna, S., "Electrospun nanofibers in energy and environmental applications", ***Energy & Environmental Science***, Vol. 1, No. 2, (2008), 205–221. https://doi.org/10.1039/B809074M
2. Malwal, D., Gopinath, P., "Efficient adsorption and antibacterial properties of electrospun CuO-ZnO composite nanofibers for water remediation", ***Journal of Hazardous Materials***, Vol. 321, (2017), 611–621. https://doi.org/10.1016/j.jhazmat.2016.09.050
3. Vaseem, M., Hong, A. R., Kim, R. T., Hahn, Y. B., "Copper oxide quantum dot ink for inkjet-driven digitally controlled high mobility field effect transistors", ***Journal of Materials Chemistry C***, Vol. 1, No. 11, (2013), 2112–2120. https://doi.org/10.1039/C3TC00869J
4. Dadi, R., Azouani, R., Traore, M., Mielcarek, C., Kanaev, A., "Antibacterial activity of ZnO and CuO nanoparticles against gram positive and gram negative strains", ***Materials Science and Engineering: C***, Vol. 104, (2019), 109968. https://doi.org/10.1016/j.msec.2019.109968
5. Mirhosseini, M., Houshmand Marvasti, S., "Antibacterial Activities of Copper Oxide (CuO) Nanoparticles in Combination With Nisin and Ultrasound Against Foodborne Pathogens", ***Iranian Journal of Medical Microbiology***, Vol. 11, No. 5, (2017), 125–135. http://ijmm.ir/article-1-742-en.html
6. Bezza, F. A., Tichapondwa, S. M., Chirwa, E., "Fabrication of monodispersed copper oxide nanoparticles with potential application as antimicrobial agents", ***Scientific Reports***, Vol. 10, No. 1, (2020), 1–18. https://doi.org/10.1038/s41598-020-73497-z
7. Kumar, N., Parui, S. S., Limbu, S., Mahato, D. K., Tiwari, N., Chauhan, R. N., "Structural and optical properties of sol–gel

derived CuO and Cu_2O nanoparticles", ***Materials Today: Proceedings***, Vol. 41, (2021), 237–241. https://doi.org/10.1016/j.matpr.2020.08.800

8. Masudy-Panah, S., Dalapati, G. K., Radhakrishnan, K., Kumar, A., Tan, H. R., "Reduction of Cu-rich interfacial layer and improvement of bulk CuO property through two-step sputtering for p-CuO/n-Si heterojunction solar cell", ***Journal of Applied Physics***, Vol. 116, No. 7, (2014), 074501. https://doi.org/10.1063/1.4893321
9. Iqbal, K., Ikram, M., Afzal, M., Ali, S., "Efficient, low-dimensional nanocomposite bilayer CuO/ZnO solar cell at various annealing temperatures", ***Materials for Renewable and Sustainable Energy***, Vol. 7, No. 2, (2018), 1–7. https://doi.org/10.1007/s40243-018-0111-2
10. Steinhauer, S., "Gas sensors based on copper oxide nanomaterials: A review", ***Chemosensors***, Vol. 9, No. 3, (2021), 51. https://doi.org/10.3390/chemosensors9030051
11. Peng, G., Wu, S., Ellis, J. E., Xu, X., Xu, G., Yu, C., Star, A., "Single-walled carbon nanotubes templated CuO networks for gas sensing", ***Journal of Materials Chemistry C***, Vol. 4, No. 27, (2016), 6575–6580. https://doi.org/10.1039/C6TC01722C
12. Avinash, B., Ravikumar, C. R., Kumar, M. A., Nagaswarupa, H. P., Santosh, M. S., Bhatt, A. S., Kuznetsov, D., "Nano CuO: Electrochemical sensor for the determination of paracetamol and D-glucose", ***Journal of Physics and Chemistry of Solids***, Vol. 134, (2019), 193–200. https://doi.org/10.1016/j.jpcs.2019.06.012
13. Buledi, J. A., Ameen, S., Memon, S. A., Fatima, A., Solangi, A. R., Mallah, A., Karimi, F., Malakmohammadi, S., Agarwal, S., Gupta, V. K., "An improved non-enzymatic electrochemical sensor amplified with CuO nanostructures for sensitive determination of uric acid. Open Chemistry", ***Open Chemistry***, Vol. 19, No. 1, (2021), 481–491. https://doi.org/10.1515/chem-2021-0029
14. Tadjarodi, A., Akhavan, O., Bijanzad, K., "Photocatalytic activity of CuO nanoparticles incorporated in mesoporous structure prepared from bis (2-aminonicotinato) copper (II) microflakes", ***Transactions of Nonferrous Metals Society of China***, Vol. 25, No. 11, (2015), 3634–3642. https://doi.org/10.1016/S1003-6326(15)64004-3
15. Senobari, S., Nezamzadeh-Ejhieh, A., "A comprehensive study on the photocatalytic activity of coupled copper oxide-cadmium sulfide nanoparticles", ***Spectrochimica Acta Part A: Molecular and Biomolecular Spectroscopy***, Vol. 196, (2018), 334–343. https://doi.org/10.1016/j.saa.2018.02.043
16. Aminzadeh, H., Shahabi Nejad, M., Mohammadzadeh, I., Sheibani, H., "Assembly of CuO nanorods onto poly (glycidylmethacrylate)@ polyaniline core–shell microspheres: Photocatalytic degradation of paracetamol", ***Applied Organometallic Chemistry***, Vol. 35, No. 12, (2021), e6423. https://doi.org/10.1002/aoc.6423
17. Wu, S., Reddy, G. K., Banerjee, D., "Pitch-Black Nanostructured Copper Oxide as an Alternative to Carbon Black for Autonomous Environments", ***Advanced Intelligent Systems***, Vol. 3, No. 9, (2021), 2100049. https://doi.org/10.1002/aisy.202100049
18. Fukuda, M., Koga, N., "Kinetics and mechanisms of the thermal decomposition of copper (II) hydroxide: A consecutive process comprising induction period, surface reaction, and phase boundary-controlled reaction", ***The Journal of Physical Chemistry C***, Vol. 122, No. 24, (2018), 12869–12879. https://doi.org/10.1021/acs.jpcc.8b03260
19. Al-Gaashani, R., Radiman, S., Tabet, N., Daud, A. R., "Synthesis and optical properties of CuO nanostructures obtained via a novel thermal decomposition method", ***Journal of Alloys and Compounds***, Vol. 509, No. 35, (2011), 8761–8769. https://doi.org/10.1016/j.jallcom.2011.06.056
20. Ranjbar-Karimi, R., Bazmandegan-Shamili, A., Aslani, A., Kaviani, K., "Sonochemical synthesis, characterization and thermal and optical analysis of CuO nanoparticles", ***Physica B: Condensed Matter. Matter***, Vol. 405, No. 15, (2010), 3096–3100. https://doi.org/10.1016/j.physb.2010.04.021
21. Pandiyarajan, T., Saravanan, R., Karthikeyan, B., Gracia, F., Mansilla, H. D., Gracia-Pinilla, M. A., Mangalaraja, R. V., "Sonochemical synthesis of CuO nanostructures and their morphology dependent optical and visible light driven photocatalytic properties", ***Journal of Materials Science: Materials in Electronics***, Vol. 28, No. 3, (2017), 2448–2457. https://doi.org/10.1007/s10854-016-5817-2
22. Sonia, S., Poongodi, S., Kumar, P.S., Mangalaraj, D., Ponpandian, N. and Viswanathan, C., "Hydrothermal synthesis of highly stable CuO nanostructures for efficient photocatalytic degradation of organic dyes", ***Materials Science in Semiconductor Processing***, Vol. 30, (2015), 585–591. https://doi.org/10.1016/j.mssp.2014.10.012
23. Bosigo, R., Lepodise, L. M., Kuvarega, A., Muiva, C., "Hydrothermal synthesis of CuO and CeO2/CuO nanostructures: spectroscopic and temperature dependent electrical properties", ***Journal of Materials Science: Materials in Electronics***, Vol. 32, No. 6, (2021), 7136–7152. https://doi.org/10.1007/s10854-021-05423-6
24. Zheng, X. G., Xu, C. N., Nishikubo, K., Nishiyama, K., Higemoto, W., Moon, W. J., Tanaka, E., Otabe, E. S., "Finite-size effect on Néel temperature in antiferromagnetic nanoparticles", ***Physical Review B***, Vol. 72, No. 1, (2005), 014464. https://doi.org/10.1103/PhysRevB.72.014464
25. Wang, Y., Jiang, T., Meng, D., Yang, J., Li, Y., Ma, Q., Han, J., "Fabrication of nanostructured CuO films by electrodeposition and their photocatalytic properties", ***Applied Surface Science***, Vol. 317, (2014), 414–421. https://doi.org/10.1016/j.apsusc.2014.08.144
26. Yang, Y., Xu, D., Wu, Q., Diao, P., "Cu_2O/CuO bilayered composite as a high-efficiency photocathode for photoelectrochemical hydrogen evolution reaction", ***Scientific Reports***, Vol. 6, No. 1, (2016), 1–13. https://doi.org/10.1038/srep35158
27. Sadabadi, H., Aftabtalab, A., Zafarian, S., Chakra, S., Rao, K. V., Shaker, S., "Influence of fuel and condition in combustion synthesis on properties of copper (II) oxide nanoparticle", ***Advanced Materials Research***, Vol. 829, (2013), 152-156. https://doi.org/10.4028/www.scientific.net/AMR.829.152
28. Xu, C., Manukyan, K. V., Adams, R. A., Pol, V. G., Chen, P., Varma, A., "One-step solution combustion synthesis of CuO/Cu2O/C anode for long cycle life Li-ion batteries", ***Carbon***, Vol. 142, (2019), 51–59. https://doi.org/10.1016/j.carbon.2018.10.016
29. Zuo, Y., Liu, Y., Li, J., Du, R., Han, X., Zhang, T., Arbiol, J., Divins, N. J., Llorca, J., Guijarro, N., Sivula, K., "In situ electrochemical oxidation of Cu2S into CuO nanowires as a durable and efficient electrocatalyst for oxygen evolution reaction", ***Chemistry of Materials***, Vol. 31, No. 18, (2019), 7732–7743. https://doi.org/10.1021/acs.chemmater.9b02790
30. Luna, I. Z., Bangladesh Atomic Energy Commission, "Preparation and characterization of copper oxide nanoparticles synthesized via chemical precipitation method", ***Open Access Library Journal***, Vol. 2, No. 03, (2015), 1. http://doi.org/10.4236/oalib.1101409
31. Rahnama, A., Gharagozlou, M., "Preparation and properties of semiconductor CuO nanoparticles via a simple precipitation method at different reaction temperatures", ***Optical and Quantum Electronics***, Vol. 44, No. 6, (2012), 313–322. https://doi.org/10.1007/s11082-011-9540-1
32. Siddiqui, H., Qureshi, M. S., Haque, F. Z., "Surfactant assisted wet chemical synthesis of copper oxide (CuO) nanostructures and their spectroscopic analysis", ***Optik***, Vol. 127, No. 5, (2016), 2740–2747. https://doi.org/10.1016/j.ijleo.2015.11.220
33. Widiarti, N., Sae, J. K., Wahyuni, S., "Synthesis CuO-ZnO nanocomposite and its application as an antibacterial agent", In

IOP Conference Series: Materials Science and Engineering, February 2017, IOP Publishing, Vol. 172, No. 1, (2017), 012036. https://doi.org/10.1088/1757-899X/172/1/012036

34. Sakib, A. A. M., Masum, S. M., Hoinkis, J., Islam, R., Molla, M., Islam, A., "Synthesis of CuO/ZnO nanocomposites and their application in photodegradation of toxic textile dye", ***Journal of Composites Science***, Vol. 3, No. 3, (2019), 91. https://doi.org/10.3390/jcs3030091
35. Raizada, P., Sudhaik, A., Patial, S., Hasija, V., Khan, A. A. P., Singh, P., Gautam, S., Kaur, M., Nguyen, V. H., "Engineering nanostructures of CuO-based photocatalysts for water treatment: current progress and future challenges", ***Arabian Journal of Chemistry***, Vol. 13, No. 11, (2020), 8424–8457. https://doi.org/10.1016/j.arabjc.2020.06.031
36. He, X., Yang, D. P., Zhang, X., Liu, M., Kang, Z., Lin, C., Jia, N., Luque, R., "Waste eggshell membrane-templated CuO-ZnO nanocomposites with enhanced adsorption, catalysis and antibacterial properties for water purification", ***Chemical Engineering Journal***, Vol. 369, (2019), 621-633. https://doi.org/10.1016/j.cej.2019.03.047
37. Kumaresan, N., Sinthiya, M. M. A., Ramamurthi, K., Babu, R. R., Sethuraman, K., "Visible light driven photocatalytic activity of ZnO/CuO nanocomposites coupled with rGO heterostructures synthesized by solid-state method for RhB dye degradation", ***Arabian Journal of Chemistry***, Vol. 13, No. 2, (2020), 3910–3928. https://doi.org/10.1016/j.arabjc.2019.03.002
38. Muhambihai, P., Rama, V., Subramaniam, P., "Photocatalytic degradation of aniline blue, brilliant green and direct red 80 using NiO/CuO, CuO/ZnO and ZnO/NiO nanocomposites", ***Environmental Nanotechnology, Monitoring & Management***, Vol. 14, (2020), 100360. https://doi.org/10.1016/j.enmm.2020.100360
39. Wei, S., Chen, Y., Ma, Y., Shao, Z., "Fabrication of CuO/ZnO composite films with cathodic co-electrodeposition and their photocatalytic performance", ***Journal of Molecular Catalysis A: Chemical***, Vol. 331, No. 1–2, (2010), 112-116. https://doi.org/10.1016/j.molcata.2010.08.011
40. Zhu, L., Li, H., Liu, Z., Xia, P., Xie, Y., Xiong, D., "Synthesis of the 0D/3D CuO/ZnO heterojunction with enhanced photocatalytic activity", ***The Journal of Physical Chemistry C***, Vol. 122, No. 17, (2018), 9531–9539. https://doi.org/10.1021/acs.jpcc.8b01933

Advanced Ceramics Progress: Vol. 8, No. 1, (Winter 2022) 9-17

Materials and Energy Research Center
MERC

Contents lists available at ACERP

Advanced Ceramics Progress

Journal Homepage: www.acerp.ir

Original Research Article

Oxidation Behavior of Spark Plasma Sintered HfB_2-SiC-Graphite Composite at 1400 °C

Mohammad Sakvand [a], Maryam Shojaie-Bahaabad [b,*], Leila Nikzad [c]

[a] *MSc Student , Faculty of Chemical and Materials Engineering, Shahrood University of Technology, Shahrood, Semnan, Iran*
[b] *Assistant Professor, Faculty of Chemical and Materials Engineering, Shahrood University of Technology, Shahrood, Semnan, Iran*
[c] *Assistant Professor, Department of Ceramics, Materials, and Energy Research Center (MERC), Meshkindasht, Alborz, Iran*

* Corresponding Author Email: mshojaieb@shahroodut.ac.ir (M. Shojaie-Bahaabad)
URL: https://www.acerp.ir/article_147536.html

ARTICLE INFO

Article History:

Received 04 March 2022
Received in revised form 20 March 2022
Accepted 05 April 2022

Keywords:

HfB_2-SiC-Graphite Composite
Spark Plasma Sintering (SPS)
Ultra-High Temperature Ceramic (UHTC)
Oxidation Behavior
Kinetic

ABSTRACT

The current study aims to fabricate the HfB_2-SiC-graphite composite through Spark Plasma Sintering (SPS) method at 1950 °C for 10 min. The oxidation behavior of the prepared composites was investigated at 1400 °C and different times of 4, 8, 12, and 16 h. In addition, the weight changes and thickness of the generated oxide layer were measured. The relative density, hardness, toughness, and strength of the composite made through the SPS method were calculated as 99.39 %, 10.16 GPa, 4.73 MPa.$m^{1/2}$, and 464.12 MPa, respectively. The oxidation kinetic results of the composite exhibited linear-parabolic behavior. The chemical reaction during the oxidation process controlled the oxidation rate after 8 h. Followed by oxidation for more 12 h, the thickness of the oxide scale slowly increased, thus following a parabolic trend as a result of a decrease in the oxygen diffusion when HfO_xC_y and SiO_xC_y phases were formed. Therefore, it was concluded that the oxygen diffusion rate could control the oxidation process.

https://doi.org/10.30501/acp.2022.332396.1083

1. INTRODUCTION

Ultra-High Temperature Ceramics (UHTCs) consist of nitrides, carbides, and borides of transition metal [1-3]. UHTCs have recently drawn researchers' attention owing to their ablation resistance and high oxidation at quite high temperatures while applied in Thermal Protection Systems (TPSs) such as nosecone, propulsion system, sharp leading edge, and rocket nozzle [3]. Among all types of UHTCs, HfB_2 has received considerbale attention compared to other deborides due to its advantagous characteristics such as higher melting temperature (3380 °C), thermal conductivity (104 W/m.K), Young's modulus (480 GPa), high resistance against oxidation, good hardness (28 GPa), and high chemical resistance [4].

Owing to the robust covalent bonds, low self-diffusion coefficient, presence of oxygen contaminants of non-oxide raw materials, and high temperature, mechanical pressure is often require d during a long period to achieve full density [3].

Numerous approaches such as hot pressing, pressureless sintering, reactive hot pressing, and plasma spark sintering, to name a few, are commonly used used

Please cite this article as: Sakvand M., Shojaie-Bahaabad M., Nikzad. L., "Oxidation Behavior of Spark Plasma Sintered HfB_2-SiC-Graphite Composite at 1400 °C", ***Advanced Ceramics Progress***, Vol. 8, No. 1, (2022), 9-17. https://doi.org/ 10.30501/acp.2022.332396.1083

for sintering HfB_2 composites [5-7].

The spark plasma process requires low sintering temperature and shorter soaking time due to its higher heating rate than that of other methods [3]. Therefore, it is possible to make ceramics at high temperatures and speeds, i.e., a homogeneous fine grain structure with full density that requires less sintering. Upon adding the metallic additives (Fe, Ni, Co, W), carbides (SiC, HfC, WC, VC), nitrides (AlN, HfN, Si_3N_4), and desilicides ($MoSi_2$, $HfSi_2$, $TiSi_2$, $TaSi_2$) [3, 8-10], both sinterability and mechanical characteristics of HfB_2 ceramics will be greatly improved.

Some recent studies pointed out to the necessity of the presence of 10-30 vol. % SiC to achieve high oxidation resistance at high temperatures. Silicon carbide can improve the oxidation resistance of HfB_2 ceramics by forming a B_2O_3-SiO_2 glass layer above 1200 °C on the surface of the HfB_2 matrix and inhibition oxygen diffusion into the bulk [11]. Followed by the oxidation of HfB_2 at 800 °C, HfO_2 (s) and B_2O_3 (l) will be formed. At 1200 °C, SiC is oxidized, and the liquid-formed SiO_2 react with B_2O_3 (l) to produce borosilicate layer on the surface.

This borosilicate layer fascilitates passive oxidation, which results in a parabolic mass gain, and decreases the oxidation rate of HfB_2-SiC composites compared to pure HfB_2 [12,13]. In this regard, many studies have been conducted on the optimization of the properties of HfB_2-SiC ceramic composite compound and coatings in the past years [14-16]. However, low fracture toughness of HfB_2-SiC ceramic composites is an obstacle to their wide applications, especially in harsh environments. It was observed that both sinterability and fracture toughness of HfB_2-SiC composites were enhanced by adding geraphen or short carbon fibers [17,18].

To the best of the authors' knowledge, the impact of SiC and graphite co-addition on the densification as well as the mechanical and oxidation behavior of HfB_2 ceramics produced through the SPS method has not been examined yet. The previous study on the effect of the graphite addition on the mechanical properties of HfB_2-30 vol. % SiC composites confirmed the good mechanical properties of the HfB_2-20 vol. % SiC-6 vol. % graphite composite. In this research, the spark plasma sintering method was employed to fabricate HfB_2-30 vol. % SiC composite combined with 6 vol. % graphite. In addition, both densification and oxidation behavior as well as the mechanical characteristics of the mentioned composite at 1400 °C for 4, 8, 12, and 16 h were studied.

2. MATERIALS AND METHODS

Commercial HfB_2, SiC, and graphite flakes were used to synthesize the HfB_2-20 vol. % SiC-graphite (6 vol. %) composite. Table 1 shows the properties of the starting powders.

TABLE 1. Characteristics of starting materials

Materials	Supplier	Dimension	Purity
HfB_2	Beijing Cerametek Materials Co., China	D < 2 µm	97 %
SiC	Xuzhou Co., China	D < 10 µm	99 %
Graphite	Qingdao Tiansheng Graphite Co.,China	D < 50 nm L < 30 µm	99.9 %

In order to mill HfB_2 and SiC powder mixtures, first, high-energy planetary milling was applied using balls and a WC-Co cup at 300 rpm in ethanol medium with the ball-powder weight ratio of 10:1 for 3 h. The graphite nano-flakes were then ultrasonically stirred in 100 mL diluted ethanol for 1 h, and the mixture of HfB_2 and SiC powder was added to the slurry and stirred for 30 min. Next, the slurry was dried on a hot plate equipped with magnetic stirring at 60 °C for 2 h. HfB_2-30SiC-graphite composites were fabricated through the SPS method (Nanozint 10i, Khala Poushan Felez Co., Iran) at 1950 °C for 10 min under 40 MPa pressure in the vacuum of 0.05 mbar.

The relative density of the composite and porosity values were calculated in the distilled water using Archimedes technique. The theoretical density was also measured based on the mixture law using the theoretical density of 11.2 g/cm^3 for HfB_2, 3.2 g/cm^3 for SiC, and 2.26 g/cm^3 for graphite. Phase analysis of composites was conducted using X-Ray Diffraction (XRD, Philips, Model: X'Pert MPD, Tube: Co, and λ: 1.78897 Å) pattern. Further, the surface and microstructure of the composite were examined using Field Emission Scanning Electron Microscope (FESEM, TESCAN, Model: MIRA) equipped with Energy Dispersive X-Ray spectroscopy (EDS) detector. The microstructure of the composite was investigated neglecting the thermal or chemical etching. The average grain size of the composite was measured by MIP Cloud software. The composite hardness was also measured using a Vickers hardness tester under 1 kg at the loading time of 10 s. In addition, the toughness of the composites was calculated through Equation (1) [14]:

$$K_{IC} = 0.073\ (P/c^{1.5}) \quad (1)$$

where K_{IC} denotes the fracture toughness (MPa.m$^{1/2}$), P the applied load (N), and c the average half-length of the crack (µm). The composite flexural strength was evaluated by a three-point flexural machine (Zwick Roell SP600, Germany) at the loading rate of 0.05 mm/min. The oxidation tests were carried out in an electric furnace at 1400 °C for 4, 8, 12, and 16 h. The composite oxidation resistance was evaluated considering the weight changes and thickness of the oxide layer after oxidation.

3. RESULTS AND DISCUSSION

Figure 1 shows the ram displacement and densification behavior of HfB_2-30 SiC-graphite composite during the SPS process.

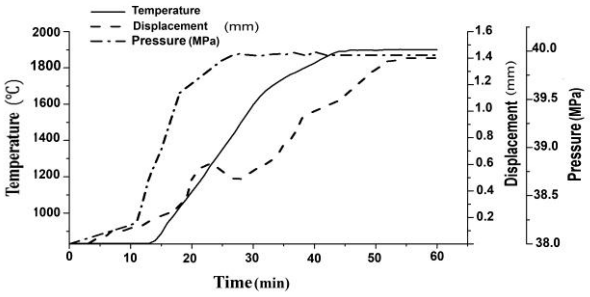

Figure 1. Displacement-Temperature-Time (DTT) curves of the HfB_2-30 SiC-graphite composite

The compaction processes include three steps: (1) compaction resulting from the rearrangement of the powder particles, increase in the contact surface of the particles, formation of more sparks, and increase in the thermal efficiency due to an increase in both pressure and temperature [17,19,20]; (2) First a decrease and then an increase in the displacement at 1100 °C: the initial decrease was indicative of the expansion caused by the gases produced by the evaporation of impurities and surface oxide contaminants in the presence of graphite additive. The second increase was caused by an increase in the pressure on the powder particles up to a final pressure of 40 MPa. Bulk deformation is caused by high temperature, neck growth among the particles, complete contact of particles, and noticeable compaction in this area; (3) A very slow increase in the slope of the curve and smooth displacement-time curves which are indicative of the complete compaction of this composite [21,22].

Apparently, the contact surface of the HfB_2 particles increased during the reaction of oxygen impurities (HfO_2 and B_2O_3) with SiC and graphite. As a result of this chemical reaction, gaseous products such as SiO, CO, and B_xO_y were produced which, prior to the production of gaseous products, caused the formation of the liquid phase and increased the sinterability of the HfB_2 powder [23].

Table 2 lists the physical and mechanical characteristics of the composite produce through SPS method. According to the results, the density of the obtained composite in this study was higher than the values reported by [24-27]. Since graphite can remove surface impurities on the SiC and HfB_2 particles and promote the densification of the composite, its addition to the composite would increase density and decrease the porosity percentage.

TABLE 2. Physical and mechanical properties of the HfB_2-30SiC-graphite composite

Material composition	HfB_2 average grain size (µm)	Relative density (%)	Apparent porosity (%)	Hardness (GPa)	K_{IC} (MPa $m^{1/2}$)	Strength (MPa)	Ref
HfB_2-20 vol. % SiC-10 vol. % $TaSi_2$	-	98.9	-	-	3.6	-	[24]
HfB_2-10 vol.% SiC	-	-	-	20.4	4.7		[25]
HfB_2-20 vol. % SiC-10 wt. % WC	6.9	99.1	-	10.6	3.36	563	[26]
HfB_2-20 vol. % SiC-20 vol. % HfC	2.57	98.8	-	21.07	3.72	585	[27]
HfB_2-15 vol. % SiC-15 vol. % $MoSi_2$	3.25	98.6	-	18	3	-	[28]
HfB_2-20 vol. % SiC-8 vol. % HfC	2.07	99.2	-	19	3.59	545	[29]
HfB_2-30 vol. % SiC-6 vol. % Graphite	HfB_2: 3.268 SiC: 2.155 Graphite: 0.125	99.39	0.61	10.16	4.73	464.12	Peresent work

The hardness of HfB_2-30 SiC-graphite composite was lower than that of HfB_2-SiC composite (18-20.4 GPa) in other researches [25,27-29]. Although this composite is characterized by a high density due to the inherent softness of graphite, its hardness is reduced.

The toughness and bending strength of HfB_2-20 SiC-graphite composite was higher and similar to those values reported in the literature, i.e., 4.65 MPa.$m^{1/2}$ and 465 MPa, respectively [24], mainly due to the laminar structure of the graphite and its role in siterability improvement of the composite. The effect of carbon fibers on the toughness of HfB_2 composites was also reported in [17].

Figure 2 shows the XRD pattern of the composite after the SPS process according to which, both HfB_2 and SiC phases can be observed in the samples, and there are no unwanted phases in the composites.

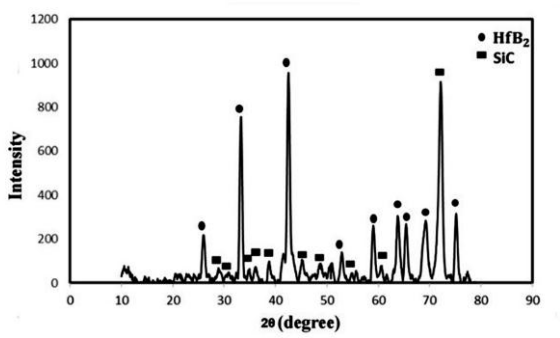

Figure 2. XRD pattern of the HfB_2-30 SiC-graphite composite sintered at 1950 °C for 10 min

Figure 3 shows the SEM images with elemental analysis (EDS) of the composite surface after the SPS process. According to EDS analysis, the dark and light areas represent the SiC and HfB_2 phases, respectively.

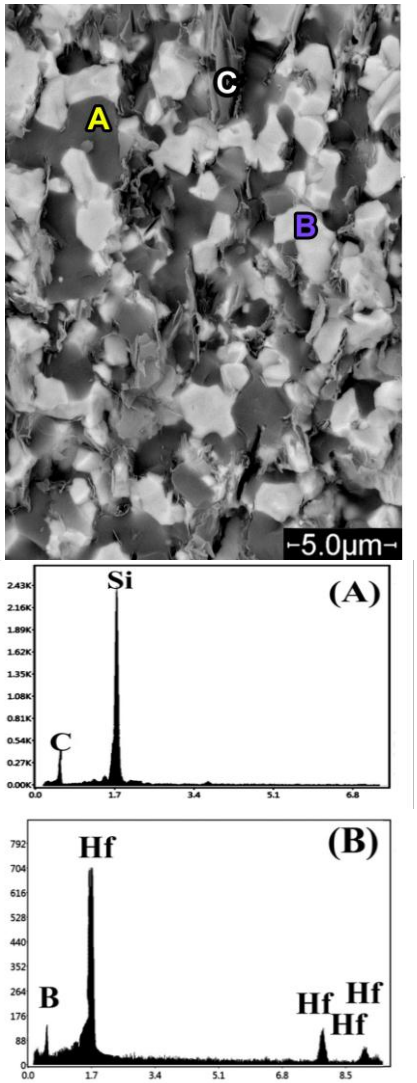

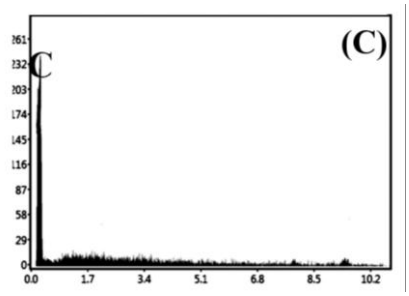

Figure 3. SEM images analysis (EDS) of the composite surface after the SPS process at 1950 °C for 10 min

Figure 4 depicts the SEM images of the fracture cross-section of the composite after the SPS process. The fracture surface of the sintered composite was a combination of the intergranular fractures. Particles pull-out and sharp edges observed in the images are possibly related to the intergranular fracture that occurred in grain boundaries (thin arrows). Certain areas, particularly in the compared surfaces with a typical grain growth compared to others, represent wide and smooth surfaces, indicating the intragranular fracture (thick arrows). An oxide layer on the surface of non-oxide particles (such as HfO_2, SiO_2, and B_2O_3) causes the generation of borosilicate glass phases. In their research work on the HfB_2-SiC composite sintered through hot pressing technique, Monteverde et al. stated that the glass phase in the SEM images was visible in the forms of coating, uniform and brittle fracture surface or a low thickness layer [30]. Such a glass phase was clearly visible in the SEM images of the cross-section of the composite prepared in the present research work (dashed flash).

In the cross-section images of HfB_2-SiC composites, graphite layers in different amounts can be observed in the cross-section, indicating that the graphite was not converted into new phases. Therefore, it can be concluded that the sintering and compressibility in the HfB_2-30 SiC-graphite systems was non-reactive.

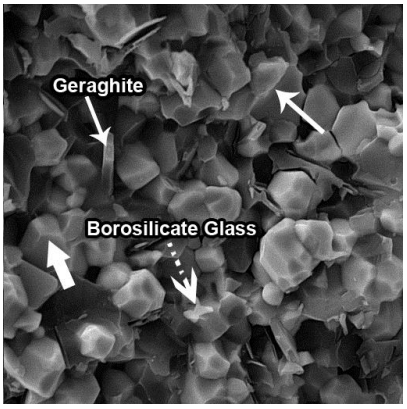

Figure 4. SEM of the fracture cross-section of the composite after the SPS process at 1950 °C for 10 min

Figure 5 presents the SEM image of the composite surface after oxidation at 1400 °C and different times according to which, the composite surface is coated with a glass layer. Oxidation of SiC particles according to reaction (2) at the temperatures above 1100 °C would form a glass layer of SiO_2 on the surface of the composite [31-35].

$$2\ SiC\ (s) + 3\ O_2\ (g) = 2\ SiO_2\ (l) + 2\ CO\ (g) \quad (2)$$

The glass layer is evenly distributed on the HfB_2-30 SiC-garaphite composite surface after oxidation for 12 and 16 h. As observed in the EDS analysis, the glass layer is evenly composed of Si and O. In addition, the white crystals of different sizes and shapes were found on the surface of composites after oxidation. According to the EDS analysis, the spherical crystals with high amounts of Hf and O and angular crystals with equal amounts of Hf and Si were HfO_2 and $HfSiO_4$ crystals, respectively.

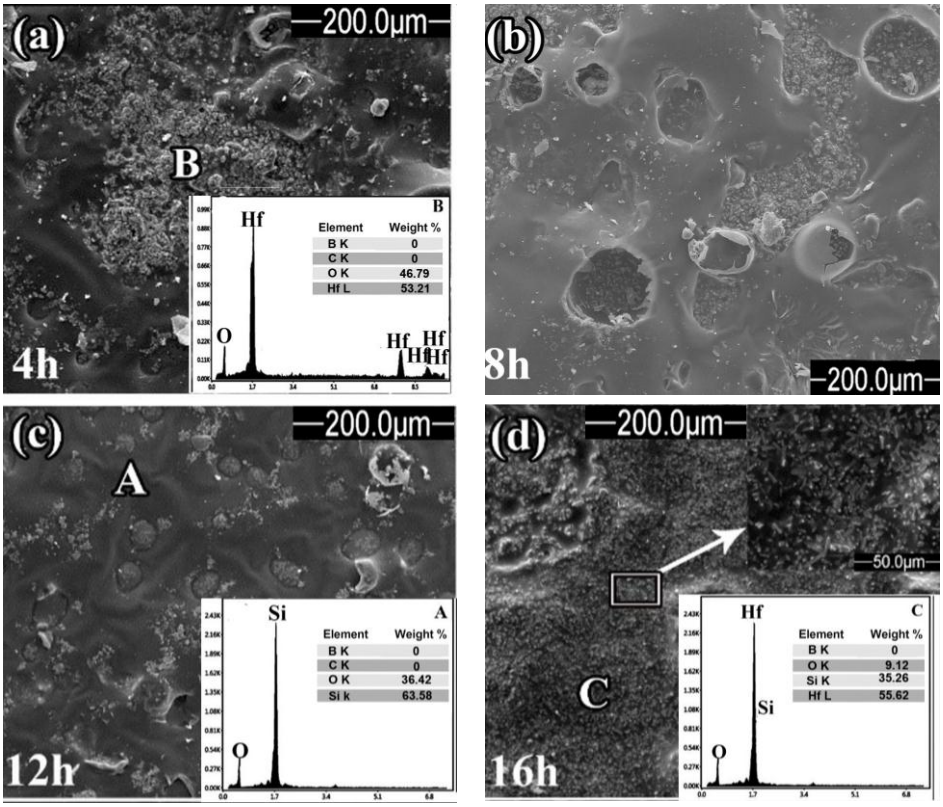

Figure 5. SEM image of the surface of the HfB_2-30 SiC-graphite composite after oxidation at 1400 °C for different Times, (a) 4 h, (b) 8 h, (c)12 h, and (d) 16 h

The formation of crystalline phases in the present study can be elaborated base on thermodynamic calculations (Figure 6) [31]. To be specific, followed by the formation of SiO_2 (reaction (2)) and HfO_2 (after oxidation at 800-1700 °C according to reaction (3)) [31], HfO_2 was first dissolved in the borosilicate melt, thus forming SiO_2-B_2O_3 (HSB) liquid in the glass layer.

As the oxidation process continued, the HSB liquid would flow from the top of the glass layer. In the case of B_2O_3 evaporation, HfO_2 particles were precipated from the HSB liquid. In addition, HfO_2 reacted with SiO_2 at temperatures above 1200 °C, according to reaction (4), thus forming $HfSiO_4$ particles [35].

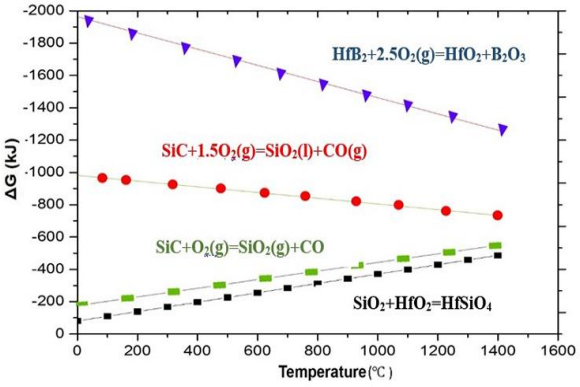

Figure 6. Gibbs free rnergy versus temperature for possible reactions in this study

$$2\ HfB_2\ (s) + 5\ O_2\ (g) = 2\ HfO_2\ (s) + 2\ B_2O_3\ (l) \quad (3)$$

$$SiO_2\ (l) + HfO_2\ (s) = HfSiO_4\ (s) \quad (4)$$

$$SiC\ (s) + O_2\ (g) = SiO\ (g) + CO\ (g) \quad (5)$$

$$B_2O_3\ (l) = B_2O_3(g) \quad (6)$$

$$3\ C\ (s) + O_2\ (g) = 2\ CO\ (g) \quad (7)$$

Two types of bubbles were observed on the surface of this oxide layer some of which grew to the surface, yet the others could not find their way to the surface. Researchers believe that this layer cannot flow near these bubbles and cover the open bubbles owing to the high viscosity of the glass layer. These bubbles can be formed by the accumulation of gaseous products resulting from active oxidation of SiC at the high temperature of 1400 °C (reaction (5)) and B_2O_3 evaporation at the temprature of above 1100 °C (reaction (6)) and oxidation of graphite at 500 °C (reaction (6)) [2, 34].

Figure 7 illustrates the cross-section of the composite after the oxidation test at different times.

According to the EDS analysis (Figure 8), the first layer was rich in Si while the second one had moderate amount of Si and Hf.

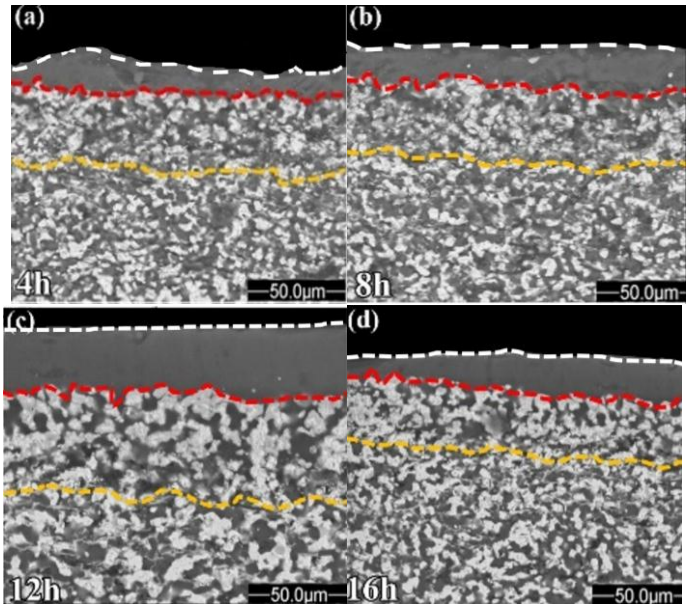

Figure 7. cross-section of the HfB_2-30 SiC-graphite composite sample after oxidation test for different times

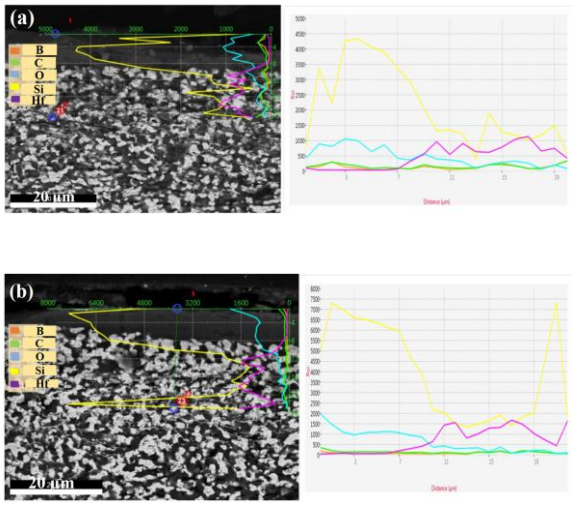

Figure 8. Line EDS analysis of the HfB_2-30 SiC-graphite composite sample after oxidation test for (a) 8 and (b) 16 h

Figure 9 shows the thickness of each layer formed on the surface of the HfB_2-30 SiC-graphite composite followed by conducting the oxidation test. The obtained results showed that followed by increasing the time of graphite oxidation during the oxidation process at 1400 °C and forming new channels for oxygen to better penetrate into the composite, the oxidation rate and thickness of SiO_2 rich layer would increase. Given that the formation of the thicker glass layer as a result of a decrease in the oxygen penetration into the composite after oxidation for 12 h, the thickness of SiO_2 rich layer would slowly increase.As observed in the EDS analysis (Figure 10), HfO_2, HfO_xC_y, and SiO_xC_y phases were formed followed by oxidation for 12 h. Zapata et al. reported the formation of MeO_xC_y (Si, Zr,Hf) after oxidation of MeB_2-SiC (Zr,Hf) composites at 1500 °C for 3 h [36,37].

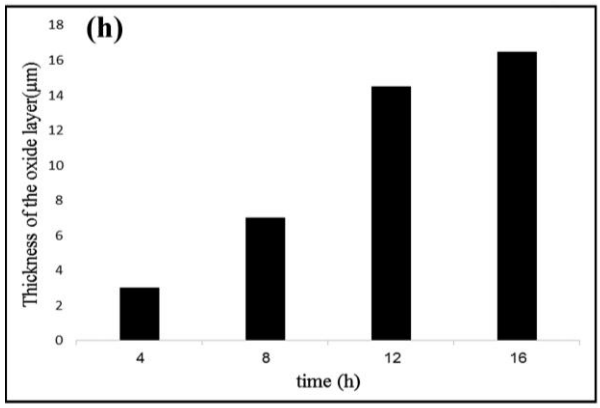

Figure 9. Thickness of the oxide layer formed on the surface after conducting the oxidation test at different times

MeO_xC_y phases were proposed as the novel protective coatings for UHTCs in cases where the oxygen diffusion

coefficients were reduced, and oxidation resistance of composites was improved for a long exposure time. In this study, followed by the formation of the HfO_xC_y and SiO_xC_y phases and their oxidation, oxygen diffusion into the composite would decrease after 12 h. As a result, the thickness of the SiO_2 layer slowly increased. Therefore, it can be expected that the composite will follow a stabilized trend at long exposure times.

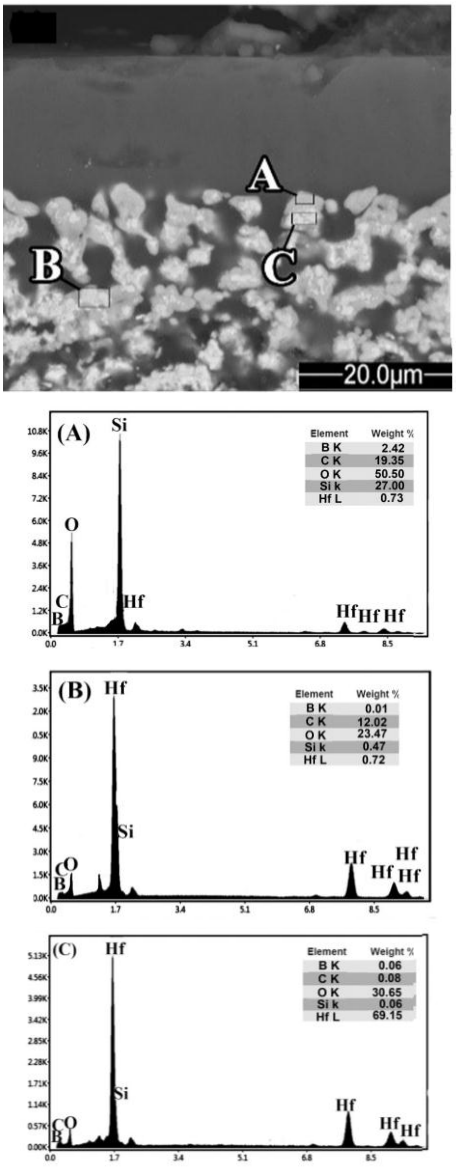

Figure 10. cross-section of the HfB_2-30 SiC-graphite composite sample after the oxidation test for 16 h

Figure 11 illustrates the oxidation kinetics of HfB_2–30 SiC–graphite composites oxidized at 1400 °C.

The oxidation mechanism is determined by the changes in the weight gain per unit surface area (ΔW/S) as an oxidation time function.

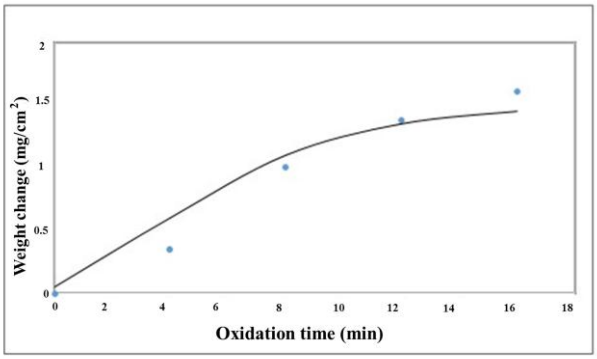

Figure 11. Oxidation kinetics of HfB_2-30 SiC-graphite composites oxidized at 1400 °C

The oxidation kinetic variables, x and k, are calculated using Equation (8):

$$(\Delta W/S)^x = kt \quad (8)$$

where x is the oxidation exponent, and k the constant of the oxidation rate.

According to the literature, while the linear trend (x=1) is indicative of the reaction rate-controlled kinetics, the parabolic one (x=2) is indicative of the diffusion rate-controlled kinetics. The value of x in the current study was calculated as 1.563 which was indicative of a linear-parabolic behavior. While the linear oxidation kinetics were observed for 8 h, the parabolic oxidation kinetics were observed for up to 16 h. The thickness of the oxide scale rapidly increased 8 h past the oxidation, thus making the trend linear.

According to Figure 5, HfO_2 and $HfSiO_4$ were the main phases on the top oxide layer at the oxidation time of less than 12 h, suggesting that under this condition, the oxidation was controlled by the reaction rate. After 12 h of oxidation, the thickness of the oxide scale gradually increased, following a parabolic trend mainly due to the impact of the produced HfO_xC_y and SiO_xC_y phases that reduced the oxygen transport. With the development of these phases, the rate of oxidation began to increase steadily. As a result, the diffusion rate determined the oxidation rate. There was a barrier for oxygen diffusion in this stage. The oxidation rate was liner at first; however, after the formation of HfO_xC_y and SiO_xC_y phases, oxygen was used for oxidation of these phases. Consequently, the oxygen diffiusion rate in the bulk decreased, hence improvement in the oxidation resistance of the composite and gradual increase in the oxidation rate.

4. CONCLUSION

In the current research, HfB_2-30 vol. % SiC-6 vol. %

graphite composite was fabricated through SPS method. The obtained composite was charaterized by high relative density (99.39 %) and good mechanical properties (the toughness and strength values were obtained as 4.73 MPa.$m^{1/2}$ and 464.12 MPa, respectively). The oxidation behavior of the composite was studied at 1400 °C and different times. The thickness of the oxide layer formed on the surface of the HfB_2-30 SiC-graphite composite increased from 3.2 µm to 16.1 µm upon increasing the oxidation time. The composite exhibited a linear-parabolic behavior during the the oxidation test, and the oxidation exponent was obtained as 1.563. The results from the elemental analysis revealed that HfO_2 and $HfSiO_4$ were the main oxide specieses on the top oxide layer at the oxidation time below 12 h, suggesting that under this condition, the oxidation was controlled by the reaction rate. After oxidation for more 12 h, the thickness of the oxide scale slowly increased, thus making the trend parabolic mainly due to the impact of the decreasing oxygen diffusion on the formed HfO_xC_y and SiO_xC_y solid solutions. Of note, the oxidation was controlled by the diffusion rate. For this reason, it expected that the composite would follow a stabilized trend at long exposure times.

ACKNOWLEDGEMENTS

The authors would like to acknowledge Sharood University of Technology and Materials and Energy Research Center for their supports throughout this study.

REFERENCES

1. Shojaie-Bahaabad, M., Hasani-Arefi, A., "Ablation properties of ZrC-SiC-HfB_2 ceramic with different amount of carbon fiber under an oxyacetylene flame", ***Materials Research Express***, Vol. 7, No. 2, (2020), 025604. https://doi.org/10.1088/2053-1591/ab70db
2. Hassan, R., Kundu, R., Balani, K., "Oxidation behaviour of coarse and fine SiC reinforced ZrB_2 at re-entry and atmospheric oxygen pressures", ***Ceramics International***, Vol. 46, No. 8, (2020), 11056-11065. https://doi.org/10.1016/j.ceramint.2020.01.125
3. Binner, J., Porter, M., Baker, B., Zou, J., Venkatachalam, V., Diaz, V. R., D'Angio, A., Ramanujam, P., Zhang, T., Murthy, T. S. R. C., "Selection, processing, properties and applications of ultra-high temperature ceramic matrix composites, UHTCMCs – a review", ***International Materials Reviews***, Vol. 65, No. 7, (2019), 389-444. https://doi.org/10.1080/09506608.2019.1652006
4. Ghelich, R., Jahannama, M. R., Abdizadeh, H., Torknik, F. S., Vaezi, M. R., "Hafnium diboride nonwoven mats with porosity/morphology tuned via different heat treatments", ***Materials Chemistry and Physics***, Vol. 248, (2020), 122876. https://doi.org/10.1016/j.matchemphys.2020.122876
5. Ni, D. W., Zhang, G. J., Kan, Y. M.,Wang, P. L., "Synthesis of monodispersed fine hafnium diboride powders using carbo/borothermal reduction of hafnium dioxide", ***Journal of the American Ceramic Society***, Vol. 91, No. 8, (2008), 2709-2712. https://doi.org/10.1111/j.1551-2916.2008.02466.x
6. Wang, H., Lee, S. H., Kim, H. D., Oh, H. C., "Synthesis of ultrafine hafnium diboride powders using solution-based processing and spark plasma sintering", ***International Journal of Applied Ceramic Technology***, Vol. 11, No. 2, (2014), 359-363. https://doi.org/10.1111/ijac.12016
7. Zou, J., Zhang, G. J., Kan, Y. M., Ohji, T., "Pressureless sintering mechanisms and mechanical properties of hafnium diboride ceramics with pre-sintering heat treatment", ***Scripta Materialia***, Vol. 62, No. 3, (2010), 159-162. https://doi.org/10.1016/j.scriptamat.2009.10.014
8. Monteverde, F., Bellosi, A., "Efficacy of HfN as sintering aid in the manufacture of ultrahigh-temperature metal diborides-matrix ceramics", ***Journal of Materials Research***, Vol. 19, No. 12, (2004), 3576-3585. https://doi.org/10.1557/JMR.2004.0460
9. Hu, D. L., Zheng, Q., Gu, H., Ni, D. W., Zhang, G. J., "Role of WC additive on reaction, solid-solution and densification in HfB_2-SiC ceramics", ***Journal of the European Ceamic Society***, Vol. 34, No. 3, (2014), 611-619. https://doi.org/10.1016/j.jeurceramsoc.2013.10.007
10. Monteverde, F., "Hot pressing of hafnium diboride aided by different sinter additives", ***Journal of Materials Science***, Vol. 43, No. 3, (2008), 1002–1007. https://doi.org/10.1007/s10853-007-2247-9
11. Mashayekh, S., Baharvandi, H. R., "Effects of SiC or $MoSi_2$ second phase on the oxide layers structureof HfB_2-based composites", ***Ceramics International***, Vol. 43, No. 17, (2017), 15053-15059. https://doi.org/10.1016/j.ceramint.2017.08.031
12. Ren, X., Shang, T., Wang, W., Feng, P., Guo, L., Zhang, P., Li, Z., "Dynamic oxidation protective behaviors and mechanisms of HfB_2-20wt%SiC composite coating for carbon materials", ***Journal of the European Ceramic Society***, Vol. 39, No. 6, (2019), 1955-1964. https://doi.org/10.1016/j.jeurceramsoc.2019.01.033
13. Guérineau, V., Vilmart, G., Dorval, N., Julian-Jankowiak, A., "Comparison of ZrB_2-SiC, HfB_2-SiC and HfB_2-SiC-Y_2O_3 oxidation mechanisms in air using LIF of BO_2 (g)", ***Corrosion Science***, Vol. 163, (2019), 108278. https://doi.org/10.1016/j.corsci.2019.108278
14. Ghadami, S., Taheri-Nassaj, E., Baharvandi, H. R., Ghadami, F., "Effect of in situ VSi_2 and SiC phases on the sintering behavior and the mechanical properties of HfB_2-based composites", ***Scientific Reports***, Vol. 10, No. 1, (2020), 1-13. https://doi.org/10.1038/s41598-020-73295-7
15. Simonenko, E. P., Simonenko, N. P., Lysenkov, A. S., Sevast'yanov, V. G., Kuznetsov, N. T., "Reactive Hot Pressing of HfB_2–SiC–Ta_4HfC_5 Ultra-High Temperature Ceramics", ***Journal of Inorganic Chemistry***, Vol. 65, No. 3, (2020), 446-457. https://doi.org/10.1134/S0036023620030146
16. Simonenko, E. P., Simonenko, N. P., Nagornov, I. A., Sevastyanov, V. G., Kuznetsov, N.T., "Production and oxidation resistance of HfB_2–30 vol % SiC composite powders modified with $Y_3Al_5O_{12}$", ***Russian Journal of Inorganic Chemistry***, Vol. 65, No. 9, (2020), 1416–1423. https://doi.org/10.1134/S003602362009020X
17. Guo, S., Naito, K., Kagawa, Y., "Mechanical and physical behaviors of short pitch-based carbon fiber-reinforced HfB_2–SiC matrix composites", ***Ceramics International***, Vol. 39, No. 2, (2013), 1567–1574. https://doi.org/10.1016/j.ceramint.2012.07.108
18. Simonenko, E. P., Simonenko, N. P., Kolesnikov, A. F., Chaplygin, A. V., Lysenkov, A. S., Nagornov, I. A., Simonenko, T. L., Gubin, S. P., Sevastyanov, V. G., Kuznetsov, N. T., "Oxidation of graphene-modified HfB_2-SiC ceramics by supersonic dissociated air flow", ***Journal of the European Ceramic Society***, Vol. 42, No. 1, (2022), 30-42. https://doi.org/10.1016/j.jeurceramsoc.2021.09.020
19. Shahriari, M., Zakeri, M., Razavi, M., Rahimipour, M. R., "Investigation on microstructure and mechanical properties of HfB_2-SiC-HfC ternary system with different HfC content prepared by spark plasma sintering", ***International Journal of Refractory Metals and Hard Materials***, Vol. 93, (2020), 105350. https://doi.org/10.1016/j.ijrmhm.2020.105350

20. Emami, S. M., Salahi, E., Zakeri, M., Tayebifard, S. A., "Effect of composition on spark plasma sintering of ZrB_2–SiC–ZrC nanocomposite synthesized by SPS", ***Ceramics International***, Vol. 43, No. 1, (2017), 111-115. https://doi.org/10.1016/j.ceramint.2016.09.118
21. Ghadami, S., Taheri-Nassaj, E., Baharvandi, H. R., Ghadami, F., "Improvement of mechanical properties of HfB_2 -based composites by incorporating in situ SiC reinforcement", ***Scientific Reports***, Vol. 11, No. 1, (2021), 1-11. https://doi.org/10.1038/s41598-021-88566-0
22. Ghasali, E., Pakseresht, A., Safari-kooshali, F., Agheli, M., Ebadzadeh, T., "Investigation on microstructure and mechanical behavior of Al-ZrB_2 composite prepared by microwave and spark plasma sintering", ***Materials Science and Engineering: A***, Vol. 627, (2015), 27-30. https://doi.org/10.1016/j.msea.2014.12.096
23. Grigoriev, S. N., Pristinskiy, Y., Soe, T. N., Malakhinsky, A., Mosyanov, M., Podrabinnik, P., Smirnov, A., Solís Pinargote, N. W., "Processing and characterization of spark plasma sintered SiC-TiB_2-TiC powders", ***Materials***, Vol. 15, No. 5, (2022), 1946. https://doi.org/10.3390/ma15051946
24. Monteverde, F., "Ultra-high temperature HfB_2–SiC ceramics consolidated by hot-pressing and spark plasma sintering", ***Journal of Alloys and Compounds***, Vol. 428, No. 1-2, (2007), 197-205. https://doi.org/10.1016/j.jallcom.2006.01.107
25. Wang, H., Lee, S. H., Feng, L., "HfB_2-SiC composite prepared by reactive spark plasma sintering", ***Ceramics International***, Vol. 40, No. 7, (2014), 11009–11013. https://doi.org/10.1016/j.ceramint.2014.03.107
26. Yuan, Y., Liu, J. X., Zhang, G. J., "Effect of HfC and SiC on microstructure and mechanical properties of HfB_2-based ceramics", ***Ceramics International***, Vol. 42, No. 6, (2016), 7861-7867. https://doi.org/10.1016/j.ceramint.2016.01.067
27. Ghadami, S., Taheri-Nassaj, E., Baharvandi, H. R., "Novel HfB_2-SiC-$MoSi_2$ composites by reactive spark plasma sintering", ***Journal of Alloys and Compounds***, Vol. 809, (2019), 151705. https://doi.org/10.1016/j.jallcom.2019.151705
28. Sakkaki, M., Moghanlou, F. S., Vajdi, M., Shahedi Asl, M., "Numerical simulation of heat transfer during spark plasma sintering of zirconium diboride", ***Ceramics International***, Vol. 46, No. 4, (2020), 4998-5007. https://doi.org/10.1016/j.ceramint.2019.10.240
29. Shahedi Asl, M., "Microstructure, hardness and fracture toughness of spark plasma sintered ZrB_2–SiC–C_f composites", ***Ceramics International***, Vol. 43, No. 17, (2017), 15047-15052. https://doi.org/10.1016/j.ceramint.2017.08.030
30. Monteverde, F., "Progress in the fabrication of ultra-high-temperature ceramics: "In situ" synthesis, microstructure and properties of a reactive hot-pressed HfB_2-SiC composite", ***Composites Science and Technology***, Vol. 65, No. 11-12, (2005), 1869-1879. https://doi.org/10.1016/j.compscitech.2005.04.003
31. Ghadami, S., Taheri-Nassaj, E., Baharvandi, H. R., Ghadami, F., "Effect of in situ SiC and $MoSi_2$ phases on the oxidation behavior of HfB_2- based composites", ***Ceramics International***, Vol. 46, No. 12, (2020), 20299-20305. https://doi.org/10.1016/j.ceramint.2020.05.116
32. Wang, P., Li, H., Sun, J.,Yuan, R., Zhang, L., Zhang, Y., Li, T., "The effect of HfB_2 content on the oxidation and thermal shock resistance of SiC coating", ***Surface and Coatings Technology***, Vol. 339, (2018), 124-131. https://doi.org/10.1016/j.surfcoat.2018.02.029
33. Simonenko, E. P., Simonenko, N. P., Gordeev, A. N., Kolesnikov, A. F., Chaplygin, A. V., Lysenkov, A. S., Nagornov, I. A., Sevastyanov, V. G., Kuznetsov, N. T., "Oxidation of HfB_2-SiC-Ta_4HfC_5 ceramic material by a supersonic flow of dissociated air", ***Journal of the European Ceramic Society***, Vol. 41, No. 2, (2021), 1088-1098. https://doi.org/10.1016/j.jeurceramsoc.2020.10.001
34. Gürcan, K., Derin, B., Ayas, E., "Effect of SiC particle size on the microstructural, mechanical and oxidation properties of In-situ synthesized HfB_2-SiC composites", ***Politeknik Dergisi***, Vol. 24, No. 2, (2021), 503-510. https://doi.org/10.2339/politeknik.682256
35. Ren, X., Mo, H., Wang, W., Feng, P., Guo, L., Li, Z., "Ultrahigh temperature ceramic HfB_2-SiC coating by liquid phase sintering method to protect carbon materials from oxidation", ***Materials Chemistry and Physics***, Vol. 217, (2018), 504–512. https://doi.org/10.1016/j.matchemphys.2018.07.018
36. Zapata-solvas, E., Jayaseelan, D. D., Brown, P. M., Lee, W. E., "Effect of La_2O_3 addition on long-term oxidation kinetics of ZrB_2–SiC and HfB_2–SiC ultra-high temperature ceramics", Journal of the European Ceramic Society, Vol. 34, (2014), 3535–3548. https://doi.org/10.1016/j.jeurceramsoc.2014.06.004
37. Guo, S., "Oxidation and strength retention of HfB_2−SiC composite with La_2O_3 additives", ***Advances in Applied Ceramics***, Vol. 119, No. 4, (2020), 218-223. https://doi.org/10.1080/17436753.2020.1755510

Advanced Ceramics Progress: Vol. 8, No. 1, (Winter 2022) 18-26

Materials and Energy Research Center
MERC

Contents lists available at ACERP

Advanced Ceramics Progress

Journal Homepage: www.acerp.ir

Original Research Article

Evaluating the Effect of the Constituent Content on the Mechanical and Biological Properties of Gelatin/Tragacanth/Nano-Hydroxyapatite Scaffolds

Parisa Madani [a], Saeed Hesaraki [b,*], Maryam Saeidifar [c], Navid Ahmadi Nasab [d,e]

[a] *PhD Candidate, Department of Nanotechnology and Advanced Materials, Materials and Energy Research Center (MERC), Meshkindasht, Alborz, Iran*

[b] *Professor, Department of Nanotechnology and Advanced Materials, Materials and Energy Research Center (MERC), Meshkindasht, Alborz, Iran*

[c] *Associate Professor, Department of Nanotechnology and Advanced Materials, Materials and Energy Research Center (MERC), Meshkindasht, Alborz, Iran*

[d] *Assistant Professor, Department of Marine Biology, Faculty of Marine Science and Technologies, University of Hormozgan, Bandar Abbas, Hormozgan, Iran*

[e] *Assistant Professor, Hormoz Research Center, University of Hormozgan, Bandar Abbas, Hormozgan, Iran*

* Corresponding Author Email: s-hesaraki@merc.ac.ir (S. Hesaraki)

URL: https://www.acerp.ir/article_150699.html

ARTICLE INFO

Article History:

Received 23 April 2022
Received in revised form 21 May 2022
Accepted 31 May 2022

Keywords:

Gelatin
Tragacanth
Nano-Hydroxyapatite
Bone
Mechanical Properties

ABSTRACT

Scaffolds made of three components containing Gelatin (30.3-64.7 wt. %), Tragacanth (23.5-60.6 wt. %) and nano-Hydroxyapatite (9.09-11.67 wt. %) were fabricated through the freeze drying process. Among the scaffolds with the components in the mentioned range, three scaffolds were selected for comparison based on pre-test steps including washout and soaking in SBF for 28 days to evaluate their consistency. At the end, two scaffolds with the maximum and moderate wt. % of gelatin were selected for further studies. The same pre-tests were done to select one of the cross-linkers namely GPTMS, $CaCl_2$, and Glutaraldehyde. As a result, GPTMS with the total amount of 10 % of the total polymers wt. % was selected as the cross-linker. The mechanical properties of the scaffolds were investigated through the compressive test, and the one with higher Gelatin content had the highest Elastic modulus. In addition, the biodegradability of the scaffolds was studied by soaking them in the PBS for 1, 3, 7, 14, 21, and 28 days and measuring the weight loss. Higher contents of Gelatin resulted in less degradation. In this research, the biocompatibility of the samples was surveyed by soaking them in the SBF for 1, 3, 7, 14, 21, and 28 days, and the formation of the apatite layer on the scaffold surface was studied using the XRD, FTIR, and SEM techniques. Of note, the apatite layer can be finely formed on the sample with moderate Gelatin content. Other two scaffolds with the maximum and minimum Gelatin contents were completely deteriorated in the SBF.

https://doi.org/10.30501/acp.2022.338756.1087

1. INTRODUCTION

Bone is a highly vascularized tissue that is able to remodel itself to maintain skeletal integration. However, in some cases, when bone loses this ability, bone mass loss and osteoporosis would occur. One of the major

Please cite this article as: Madani, P., Hesaraki, S., Saeidifar, M., Ahmadi Nasab, N., "Evaluating the Effect of the Constituent Content on the Mechanical and Biological Properties of Gelatin/Tragacanth/Nano-hydroxyapatite Scaffolds", ***Advanced Ceramics Progress***, Vol. 8, No. 1, (2022), 18-26. https://doi.org/10.30501/acp.2022.338756.1087

causes of osteoporosis is the lack of balance between the osteoblast and osteoclast activities that cause bone formation and bone resorption, respectively, hence a decrease in the bone mass and its vulnerability against trauma. Traditional therapies such as bone autografts, in addition to being invasive, may cause some problems such as infection. Given the considerable advantages of bone tissue engineering methods including low costs, less trauma, and immunotoxicity, they have drawn a great deal of attention due to their different applications. For instance, bone tissue engineering scaffolds have been widely used in the past few years in order to prevent the progression of osteoporosis and treat the damages to the bone. These scaffolds are required to have some physical and mechanical properties similar to those of bones namely the bioactivity, biocompatibility, non-toxicity, and cell attachment to stimulate bone formation [1]. Given that the damaged and porous bones are less able to remodel themselves, there are only a few cases of bone tissue engineering scaffolds that have succeeded in bone remodeling. Therefore, choosing the proper components of the bone tissue engineering scaffold and determining the ratio of the components are the major challenges in this regard. Since the natural bone is composed of organic and inorganic nano-composites, the elemental texture of the bone is stiff, mainly containing inorganic calcium hydroxyapatite with the chemical formula of $Ca_{10}(PO_4)_6(OH)_2$ as Nano-crystals, which is the main causes of bone stiffness. The organic phase of the bone matrix is mainly composed of Type I collagen which is an elastic protein that optimizes fracture strength and strengthens the attachment, growth, and differentiation cells. Other organic components existing in the bone tissue are glycosaminoglycans, osteocalcin, osteonectin, bone sialoproteins, and osteopontin. Despite the high strength of the inorganic matrix of the bone, it is still fragile. On the contrary, the organic matrix (like Collagen fibrils) is flexible yet less strong. The combination of these two phases form a matrix with high strength and flexibility that is not brittle.

Since the bone matrix is made of different components with the mentioned properties, the tissue engineering scaffolds designed to mimic the bone behaviors and properties must be composed of different ingredients. Therefore, choosing the best materials for fabricating the bone tissue engineering scaffold is an improtant challenge to be taken into account. In addition, the weight percentage of the scaffold components is another factor that affects the scaffold function when used in bones with osteoporosis or trauma. The currsent study put its main focus on these two challenges in order to design and fabricate a scaffold used in non-load bearing bones or bones with osteoporosis issues.

The main constituent of the scaffold in this study is Gelatin which is a natural polymer that can mimic extracellular matrix and provide a convinient microenvironment for cell growth and proliferation [2] since it is composed of amino acids and peptides obtained from minor hydrolysis of triple helix bonds of Collagen. Among these amino acids, Arginine, Glycine, and Aspartic acid (RGD sequence) provide the necessary signals for the proliferation, adhesion and differentiation of cells. However, Gelatin has high degradation rate and low compressive strength of about 0.03 MPa, hence not suitable for bone tissue engineering applications. Therefore, Gelatin must be utilized in a combination with other components such as chitosan, hyaloronic acid or collagen (proteins and polysaccharids) which are used in several bone tissue engineering applications due to their proper degradation rate and less immunological responses [3]. Among these natural biopolymers, polysaccharids, specifically natural gums, have significantly drawn attention due to their availability, low preparation costs, hydrophilicity, appropriate biological responses, resembling extracellular matrix properties, and high binding capability [4].

One of these natural gums is Gum Tragacanth (GT) which is a heterogeneous branched anionic polysaccharid obtained from a native Iranian herb that simulates bone features in the scaffold [5]. It is an antibacterial polymer with high molecular weight that is easily solved or well dispersed in water. It is also highly resistant against heat, acidity, and aging. It has been proved that using GT-based hydrogels would increase osteoconductivity, compared to Collagen hydrogels and tissue culture plate. Tragacanth is a non-toxic material with the highest ALP activity and bone mineralization with the highest expression of Runx-2, osteonectin, and osteocalcin by the bone mesenchymal stem cells, which are the main factors contributing to bone formation and osteogenic differentiation. GT also plays a key role as a binder that helps omit toxic crosslinkers [6]. Moreover, adding it to the common matrices used for encapsulation of bone cells used in bone tissue engineering such as Calcium Alginate (CA) beads improves degradation and swelling of the beads and stimulates cell proliferation and differentiation. Due to the abundant hydroxyl (OH) and carboxyl (COOH) groups existing in the GT, it provides suitable sites for crosslinking and Hydrogen binding with other molecules with the same functional groups [7]. Of note, the presence of active functional groups in the GT chains as the binding sites is another notable characteristic of this gum that makes it suitable for conjuction of drugs. In addition, its swelling ability, which creates a three dimensional network, makes it a proper choice for drug encapsulation that turns it into a desirable drug delivery system [8]. Moreover, GT is anti-microbial, anti-inflammation, non-allergic, and non-toxic [9]. Despite all these high-grade properties of GT, this gum have been limitedly applied in bone tisssue engineering and osteogenesis. For this reason, this constituent is a novel component of the scaffold in this study. Osteogenic differentiation of human adipose-derived mesenchymal stem cells cultured on the GT

hydrogel was already proved, thus confirming its application in orthopedics and bone regeneration [10].

In order to utilize this polysaccharide in bone tissue engineering, its structure must be stabilized using biocompatible coupling agents and crosslinkers such as GPTMS (3-glycidoxypropyl) [11]. Not only does this crosslinker increase the consistency of this biopolymer, but also it adjusts its biological properties and optimizes the interfacial interactions of the composites containing GT [12,13]. GPTMS is biologically safe and non-toxic and that facilitates cell adhesion and proliferation.

Although fabrication of a bone tissue engineering scaffold with only two polymer consituents simulates the organic phase of the extracellular matrix and results in cell ingrowth, the bioactive components are still necessary for bone healing. Among these components is Hydroxyapatite (HAp) which is the most important inorganic component of the natural bone that is highly bioactive and non-toxic [14,15]. HAp can improve the mechanical properties of the scaffold and increase both cell proliferation and adhesion by creating hydrophilic surfaces [15]. It also enhances the osteogenic differentiation of the mesenchymal stem cells. In addition, it has good distribution, thus facilitating the interactions between the scaffold and osteogenic cells owing to the relatively high ratio of the surface area to volume.

In order to design a scaffold with the mentioned properties, we must determine the ratio of the scaffold components as well. In this study, attempts were made to design a scaffold with three components and determine the best wt. % of the components in order to obtain the best mechanical and biological properties. To this end, three scaffolds with different wt. % of the components containing Gelatin, Nano-HAp, and Tragacanth were designed to choose the best scaffold with the closest mechanical properties to those of the cortical bone, fine apatite formation, and same biodegradability rate as the cortical bone formation.

In fact, the main objective of this study was to design and fabricate a scaffold simulating cortical bone mechanical, physical, and biological properties based on the interactions among the components.

2. MATERIALS AND METHODS

2.1. Starting Materials

In order to prepare the scaffold, Nano-HAp (CAS 12167-74-7) with the particle size of < 200 nm, Gelatin Type B (obtained from alkaline hydrolysis of insoluble Collagen) from bovine skin, Tragacanth, G1128, (CAS 9000-65-1, EC 232-552-5), and Glutaraldehyde (CAS 111-30-8) were purchased from SIGMA-Aldrich, Germany. In addition, Calciumchlorid (CAS 10043-52-4) and GPTMS (CAS 2530-83-8) were purchased from Merck, Germany and then, Phosphate-Buffered Saline (PBS) with 1X concentration and pH of 7.3 (CAS 11510546) was purchased from Gibco, United Kingdom. Double Distilled (DD) water was used as the solvent for the scaffold components, and SBF was prepared based on the Kokubo method [16].

2.2. Composition of the Scaffolds

In this study, different compositions of the scaffolds were investigated to find the best scaffold with the optimum mechanical, physical, and in vitro biological properties.

As a result, three scaffolds were designed considering the following compositions given in Table 1. All the compositions were inserted as wt. %, and their compositions were designed according to our pre-tests, containing wash out with DD water and soaking in SBF for 28 days. Samples that were not completely deteriorated in the SBF for 28 days were selected for further studies. All the ratios of GPTMS, the crosslinking agent, were constant. The total amount of the cross-linking agent was considered 10 % of the total weight of the polymers used. Of note, GPTMS was selected as the cross-linking agent according to the pre-tests when compared to $CaCl_2$ and Glutaraldehyde mainly because the scaffolds fabricated with different percentages of the other two cross-linkers were washed out in distilled water and completely deteriorated in the SBF solution after one day. It is worth mentioning that the scaffold with the minimum wt. % of Gelatin was deteriorated in the washing process with DD water and therefore, it was omitted. Finally, only two scaffolds with maximum and moderate wt. % of Gelatin remained, hence selected for further studies.

TABLE 1. Compositions of the studied scaffolds

Composition	Gelatin	Tragacanth	nHAp	GPTMS
G1	30.3 %	60.6 %	9.09 %	Fixed
G2	47.5 %	42.05 %	10.42 %	Fixed
G3	64.7 %	23.5 %	11.76 %	Fixed

2.3. Scaffolds Fabrication Technique

Solutions of the scaffold components with equal volumes and different wt. % of the components were prepared. In order to make G1, first, 0.909 g of nHAp was poured into 10 cc of distilled water and mixed on a stirrer to obtain a homogeneous solution. Then, 3.03 g of Gelatin was poured into 10 cc of distilled water. Given the better solulabilituy and more uniformity of gelatin at higher temperatures, the obatined solution was transferred to a heater-stirrer at the temprature of 40-50 °C and mixed for 30 minutes to be completely dissolved. Afterwards, 6.06 g Tragacanth was added to 10 cc of distilled water and mixed with a heater-stirrer to be uniformly dissolved. GPTMS was then added to the gelatin solution and mixed for another 30 minutes. All

mixing processes were done at the speed of 350 rpm. The total amount of GPTMS was considered as 10 % of the total weight of the polymers: (3.03+6.06)*10% = 0.9. Subsequently, 0.9 cc of GPTMS was added to the gelatin solution. These three aqua solutions were incorporated and mixed for 24 hours on a heater-stirrer at the temparature and mixing speed of 40 °C and 350 rpm, respectively. The acquired solution was poured into 3 cc syringes, transferred to the liquid Nitrogen for quick freezing, kept aways from percipitation of nHAp particles, and kept in a -20 °C freezer overnight mainly because nHAp would only be dispersed in the composition. The obtained cylindrical structure was then put in the freeze dryer (Pishtaz Equipment Engineering Co.) for 48 hours to complete the scaffold fabrication procedure.

The same process was repeated for G2 and G3 scaffolds with the mentioned wt. % of the components.

2.4. Experiments

To study the mechanical properties, biocompatibility, degradation rate, and cell attachment, the following experiments were carried out.

2.4.1. Mechanical Testing

The scaffolds were cut into cylindrical shapes with the diameter and height of 10 mm and 20 mm, respectively, with parallel surfaces. The specimens were then transferred to a compressive strength testing device (SANTAM STM-20). Compression tests were repeated with three samples for each scaffold, and the Elastic modulus of the scaffolds were obtained through the following equation:

$$E = \sigma(\varepsilon)/\varepsilon = \frac{F/A_\circ}{\Delta L/L_\circ} = \frac{FL_\circ}{A_\circ \Delta L} \quad (1)$$

2.4.2. Physical Characterizing

The scaffolds were characterized using FTIR, XRD, and SEM prior to and followed by soaking in the SBF solution at different time intervals of 3, 7, 14, 21, and 28 days to evaluate the phases and bonds and make sure whether the bonds between the three components are made and they are crosslinked as well and also, to study the apatite formation in order to evaluate biocompatibility of the scaffolds. The samples were also studied using the Scanning Electron Microscopy (SEM) to monitor their structure and porosity.

2.4.3. In vitro Apatite Formation

Scaffolds used in the non-load bearing bone defects must be attached well to the adjacent bone. This process is not done unless a proper layer of apatite is formed on the surface of the scaffold. In this regard, the apatite layer formation test in Simulated Body Fluid (SBF) was done.

Scaffold cylindrical samples were submerged in the SBF solution for 3, 7, 14, 21, and 28 days. All FTIR, XRD, and SEM experiments were carried out to find information about the chemical composition of the surface, figure out whether or not the apatite layer is formed, and measure the thickness of the apatite layer.

2.4.3.1. FTIR

To prepare the samples for the FTIR spectroscopy (Victor 33, Broker, Germany) with 45 scan per sample, the scaffolds were first grinded, and the obtained powder was mixed with Potassium Bromide (KBr, an inactive material against the IR spectra) to acquire powder particles with the diameters of less than 2 µm. Then, the powder was compressed to obtain shots and exposed to IR spectra to record the FTIR spectra.

Apatite formation was also evaluated using FTIR analysis for the scaffolds prior to and followed by soaking in SBF for 28 days based on a comparison between the obtained spectrum and identified peaks related to Carbonated HAp.

2.4.3.2. SEM

The scaffolds were cut into thin slices with the dimensions of 3 mm, dried well, and covered with a thin layer of gold in order to make them electro-conductive. Then, the samples were placed into the SEM S360-Cambridge 1990, and the obtained images were analyzed to investigate apatite formation on top of the scaffolds. The images were compared for the scaffolds before and after 28 days of simmering in SBF.

2.4.3.3. XRD

The XRD pattern of the scaffold was obtained using Philips PW3710 diffractometer with the X-Ray source of Cu-Kα and step size of 0.02°. It is worth mentioning that λ was obtained as 0.154 nm.

2.4.4. In vitro Biodegradation

Scaffolds were soaked in Phosphate Buffer Saline (PBS) for 3, 7, 14, 21, and 28 days. Then, their weight changes were evaluated.

3. RESULTS AND DISCUSSION

3.1. Mechanical Testing

Since the fabricated scaffolds are meant to be placed in the cortical bones and preferably in non-load bearing sites, their mechanical properties were evaluated using compression test (SANTAM STM-20) at the speed of 1 mm/min. All compression tests were repeated with three samples, and the mean value of their mechanical properties was considered as the result.

Figure 1 shows the elongation of the samples as a function of the applied force for the G2 sample. The elastic modulus as long of peak for each sample was 1.67,

1.31, and 1.39 MPa, and the average Elastic modulus was 1.456 MPa. All mean values of the other mechanical properties related to the samples of G2 and G3 are shown in Table 2. Elongation as a function of force for the G3 sample is given in Figure 2. The compression test was repeated with three samples.

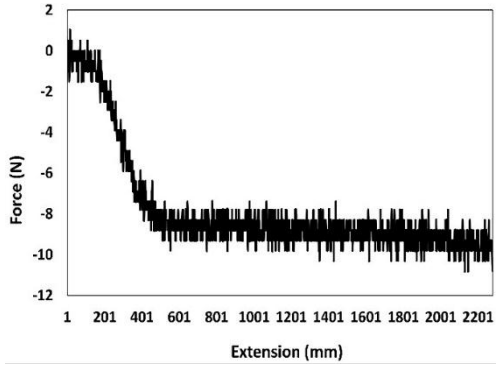

Figure 1. Elongation as long of peak for the G2 sample

TABLE 2. Mean values of the mechanical properties of the G2 and G3 samples

	G2		G3	
Sample	Peak	Break	Peak	Break
Force (N)	-10.8	-10.3	-54	-52.7
Extension (mm)	-5.94	-5.94	-6.04	-6.08
Stress (MPa)	-0.25	-0.23	-1.13	-1.12
Elongation (%)	-43.4	-43.4	-42.27	-42.58
Elong Aft. Brk (%)	-25.15	-26.01	-32.27	-32.68
Energy (J)	-30.6	-30.57	-159.83	-159.5
Bending St. (MPa)	-0.87	-0.83	-4.17	-4.13
Bending Strain	-1.45	-1.45	-1.38	-1.4
Bending Module	0.61	0.58	3.04	2.98

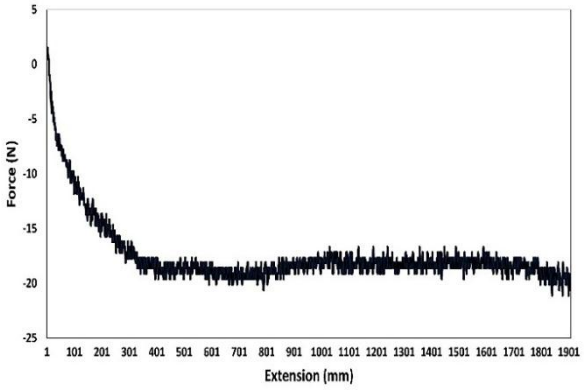

Figure 2. Elongation as long of peak for the G3 sample

According to the results, the mean elastic modulus for the G2 scaffold and the G3 scaffolds were 1.4 MPa and 12.47 MPa, respectively. The elastic modulus of the G2 scaffold is lower than those of the other due to less Gelatin wt. %.

Given that the main crosslinking occurs mostly between Gelatin, Tragacanth, and GPTMS, less wt. % of these two components would result in less crosslinking and lower strength of the scaffold, thus confirming the results from the previous studies emphasizing that Gelatin and GT acted as the binder in ceramic scaffolds [17].

Higher wt. % of nHAP is another reason for higher elastic modulus of the G3 scaffold. To be specific, according to the previous studies [18], an increase in the wt. % of HAp results in higher elastic modulus, which is an outcome of higher scaffold integrity due to less porosity. Higher wt. % of GT in the G2 samples results in higher compression yield strength and compressive strength, and a decrease in the porosity, according to the previous studies [10]. However, higher wt. % of Gelatin and its effect on mechanical properties undermined the role of wt. % of GT in the scaffold.

Based on the results from the mechanical testing, it can be concluded that the G3 sample has closer elastic modulus to that of the trabecular bone, which is in the range of 10-3000 MPa. However, given that the elastic modulus of the trabecular bone decreases by 10 % for every decade of aging due to the changes in the bone density and increase in the anisotropy of bone compressive strength, the G2 sample can be technically a better choice for bone remodeling throughout the healing process based on the tissue engineering approaches. Moreover, damages casued by osteoporosis can have the same effect on the cancellous bone. As a result, the scaffold has less elastic modulus and less compressive strength, hence a better choice for cortical bone substitute. Of note, the compressive strength of the spongy bone is quite low, i.e., approximately 0.036-2.945 MPa [10].

3.2. Physical Characterizing

3.2.1. In vitro Biodegradation

Scaffolds were soaked in the PBS for 3, 7, 14, 21, and 28 days and changes in their weights were evaluated. The degradation value can be obtained through the following formula:

$$\text{Degradation}= \frac{m2-m1}{m1} *100 \quad (2)$$

where m_2 is the sample weight after its exposure to the PBS, and m_1 the initial weight of the sample. Figure 3 refers to the degradation as a function of time for G2 and G3 samples.

According to the degradation results, the degradation percentage increased with time for both sample groups, and the degradation rate of the G2 sample after 28 days was more than that of the other samples mainly because of the lower wt. % of Gelatin and GT since more cross-linking happens between Gelatin, GT, and GPTMS, and G2 has lower wt. % of these two components.

Both G2 and G3 scaffolds were characterized by fair biodegradability as well as 10.3 % and 9.5 % weight loss after 28 days soaking in the PBS, respectively. This is a fair degradation rate because the first two stages of bone remodeling, i.e., resorption and reversal, takes about six to seven weeks to be completed, and the last stage, i.e., bone formation, takes up to four months to completely heal the bone [19].

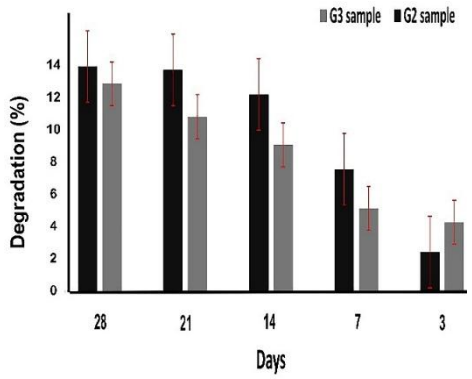

Figure 3. Degradation percentage for the scaffolds in the PBS at different time intervals

Higher weight loss of the G2 sample can be attributed to lower wt. % of nHAP and Gelatin. As stated in the previous studies [16], higher amounts of nHAP would result in less porosity and consequently less degradation due to less diffusion of the PBS into the scaffold. Further, higher wt. % of gelatin in the G3 sample nullified the binding effect of higher wt. % of Tragacanth in the average sample, thus resulting in lower degradation rate. Two or three weeks after the trauma marks the beginning of the transformation of a fragile cartilage like tissue in the defect site into the bone tissue. This process takes about 6 to 12 weeks (6 weeks for the upper limb, and 12 weeks for the load-bearing sites). In fact, since the degradation rate of the scaffolds were close, the G2 scaffold was selected as the optimum one owing to the other properties similar to the cortical bone.

3.2.2. In vitro Apatite Formation

3.2.2.1. SEM Analysis

SEM images from the samples prior to and followed by soaking in the SBF were compared to study whether or not the apatite layer was formed. After 28 days of soaking in the SBF, the G3 sample was completely deteriorated, and the apatite formation was monitored after three days. Then, the G2 samples were dried at the room temperature, cut into thin slices with the dimensions of 3 mm, and covered with a thin layer of gold to make the samples electro-conductive. Next, the samples were put inside the SEM (SEM S360-Cambridge 1990).

Figures 4-7 depcit the SEM images of both sample groups where the apatite layer is clearly visible as the lighter areas. A thick and dense layer of apatite was finally formed on the G3 sample surface, and the porosity of the sample was reduced due to shrinkage caused by higher wt. % of Gelatin.

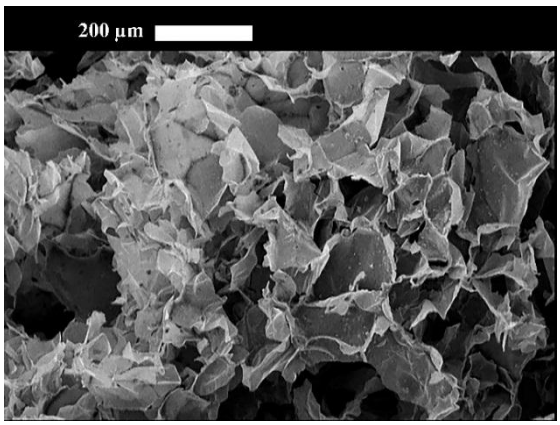

Figure 4. SEM image of the G2 sample before soaking in the SBF

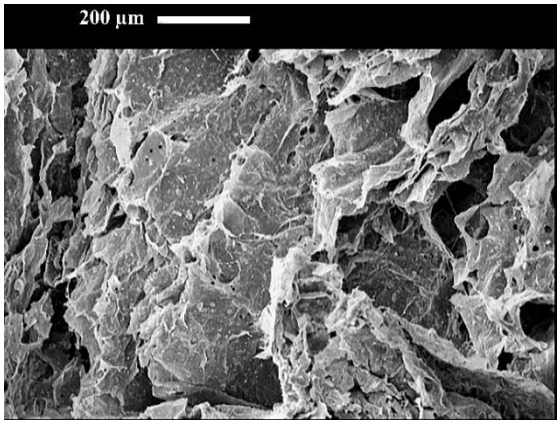

Figure 5. SEM image of the G2 sample after soaking in the SBF for 28 days. Carbonared Nano-HAp percipitates are visible

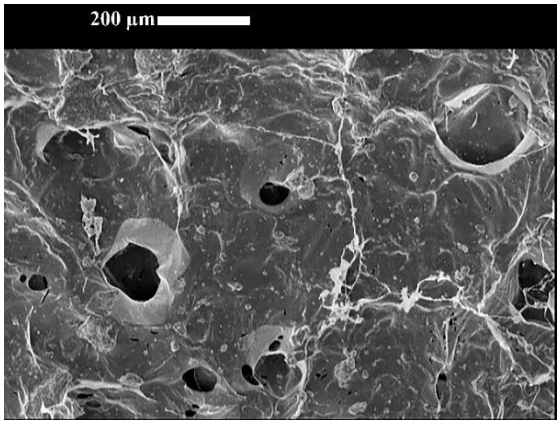

Figure 6. SEM image of the G3 sample before soaking in SBF

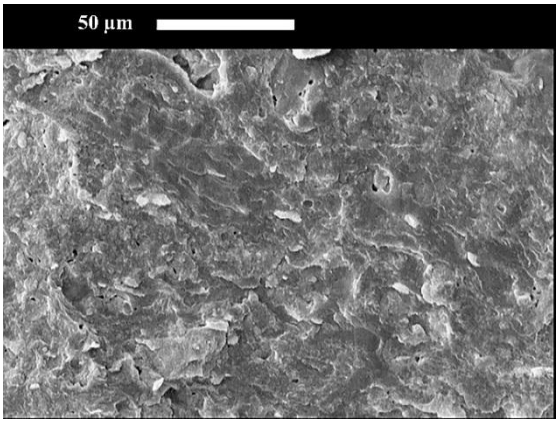

Figure 7. The SEM image of the G3 sample after soaking in the SBF for three days. Carbonated Nano-HAp percipitates are visible

3.2.2.2. XRD Analysis of the Scaffolds

Figures 8 and 9 show the XRD patterns of the G2 and G3 scaffolds, respectively, prior to and followed by soaking in the SBF for 28 days. Given that the G3 scaffold was deteriorated in the SBF after one day, the XRD pattern was obtained only before soaking in the SBF. As indicated in both XRD patterns, a sharp peak around 2θ=32° is observed corresponding to the carbonated HAp for the (211) and (112) atomic planes (according to JCPDS-9-432) which broadens after soaking in the SBF, and the peak width is reduced which is a sign of crystallization of the Carbonated HAp.

3.2.2.3. FTIR Analysis of the Scaffolds

Since the G3 sample was deteriorated in the SBF, its FTIR spectra was obtained only before soaking in the SBF, as shown in Figure 10.

Table 3 confirms the presence of the peaks and their corresponding bonds of the G3 sample.

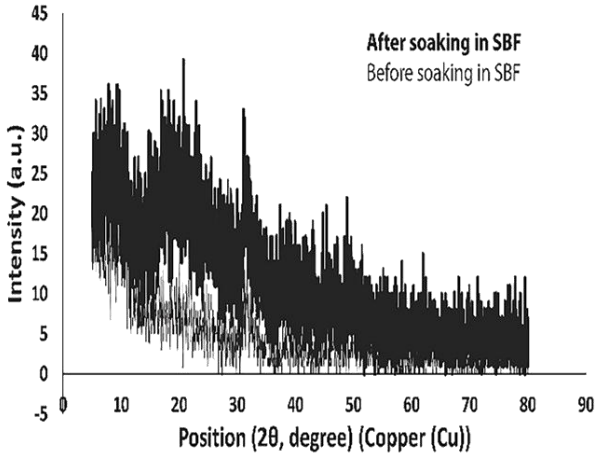

Figure 8. XRD pattern of the G2 sample before and after 28 days soaking in SBF

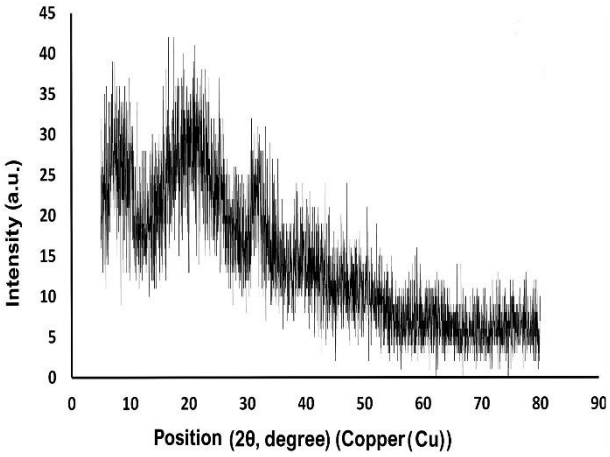

Figure 9. XRD pattern of the G3 sample before and after 28 days soaking in SBF

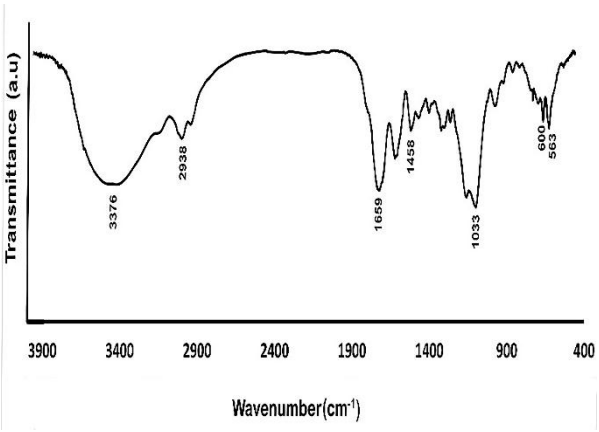

Figure 10. FTIR spectra of the G3 scaffold

TABLE 3. Peaks of FTIR spectra for the G3 sample

Wave No.	Stretching Mode	Ref.
3376	Stretching vibration of O-H groups in Gum Tragacanth	[20]
2938	Symmetric stertching vibrations of methylene groups in Gum Tragacanth	[20]
1659	Amide I regions in Gelatin containing C=O stretching vibration with contribution of C-N bond stretching vibration	[21]
1458	Asymmetric stretching of CO_3^{2-} in nHAp	[22]
1033	Asymmetric stretching of PO_4^{3-} in nHAp	[22]
600	Amide III region in Gelatin representing vibration in the plane of C-N and N-H groups of bound amide or vibration of CH_2 groups	[21]
563	Asymmetric bending vibration of PO_4^{3-} in nHAp	[22]

Table 4 shows the peaks of the FTIR spectra of the G2 sample.

TABLE 4. Peaks of FTIR spectra for the G2 sample

Wave No.	Stretching Mode	Ref.
3345	Stretching vibrations of O–H groups in the gum Tragacanth	[20]
2935	Symmetric stretching vibrations of methylene groups in the gum Tragacanth	[20]
2880	Asymmetric stretching vibrations of methylene groups in Gum Tragacanth	[20]
1662	C–O stretching vibrations of polyols vibration with contribution of C-N bond stretching vibration in Amide I regions of Gelatin	[21]
1551	Amide II regions in Gelatin from N-H bending vibration and C-N stretching vibration	[21]
1454	Ion Stretching of O-H in nHAp	[22]
1240	C–O stretching vibrations of polyols in Gum Tragacanth	[20]
1204	vibration in the plane of C-N and N-H groups of bound amide or vibration of CH2 group in Amide III region of Gelatin	[21]
1092	Asymmetric stretching of PO_4^{3-} in nHAp	[22]
918	Out of plane bending mode CO_3^{2-} in nHAp	[22]
598	Asymmetric bending vibration of PO_4^{3-} in nHAp	[22]
563	Asymmetric bending vibration of PO_4^{3-} in nHAp	[22]

Figure 11 makes a comparison between the FTIR spectra of the G2 sample prior to and followed by soaking in the SBF based on which, it can be concluded that the apatite already began to crystallize since the twin peak at 1092 cm^{-1} in the G2 sample was turned into a single peak. Peaks at around 1400 cm^{-1} are related to Carbonates, and the twin peaks at 1415 cm^{-1} in the sample after soaking is indicative of the Carbonated HAp.

A decrease in the peak intensity at 2940 cm^{-1} in the sample after soaking, compared to that at 2935 cm^{-1} in the sample before soaking which is related to the C-H bonds, shows that the polymer components of the scaffold were absorbed, meaning that the scaffold is being well-degraded.

Moreover, the peak at 1546 cm^{-1} in the spectra followed by soaking is also attributed to the carbonated HAp, and the peaks at 601 and 563 cm^{-1} are attributed to PO_4^{3-}.

Elimination of the peaks at 1240 and 1204 cm^{-1} wavenumbers in the FTIR spectra of the G2 scaffold after soaking in SBF is a sign of polymeric regions of the scaffold since these two wavenumbers are related to GT and Gelatin, respectively.

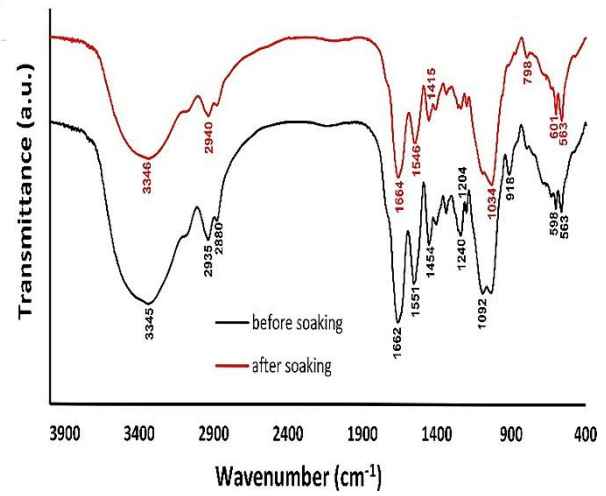

Figure 11. FTIR spectra of the G2 scaffold prior to and followed by soaking in SBF for 28 days

4. CONCLUSION

The current research primarily aimed to design and fabricate three scaffolds with different wt. % components namely Gelatin, Tragacanth, and Nano-HAp. At the end of the study, based on the mechanical, physical and biological experiments, the G2 scaffold, the sample with the moderate wt. % of Gelatin (The scaffold containing 47.5 % Gelatin, 42.05 % Tragacanth, and 10.42 % nHAp), was selected as the optimum sample for bone tissue engineering. The Elastic modulus of this scaffold was measured as 1.45 MPa, which was suitable for spongy or defected bones with osteoporosis. The apatite formation of the mentioned scaffold was proved and investigated using the XRD, FTIR, and SEM analyses. As observed in the SEM images, the apatite layer are clearly visible, and the peaks in the XRD spectra at $2\theta=32°$ demonstrate the carbonated HAp, the main component of the natural bone. Differences in the peak intensities of the FTIR spectra priror to and followed by soaking in the SBF were indicative of the apatite crystalization and polymer components absorption as a result of the scaffold degradation. These results in general proved that the scaffold designed and fabricated in this study could be a promising one for further bone tissue engineering studies.

ACKNOWLEDGEMENTS

The authors would like to acknowledge Mr. Nouraie and Kavousi, the XRD and FTIR lab. Managers.

REFERENCES

1. Feng, P., He, J., Peng, S., Gao, C., Zhao, Z., Xiong, S., Shuai, C., "Characterizations and interfacial reinforcement mechanisms of multicomponent biopolymer based scaffold", ***Materials Science and Engineering: C***, Vol. 100, (2019), 809-825. https://doi.org/10.1016/j.msec.2019.03.030
2. Ma, P., Wu, W., Wei, Y., Ren, L., Lin, S., Wu, J., "Biomimetic gelatin/chitosan/polyvinyl alcohol/nano-hydroxyapatite scaffolds for bone tissue engineering", ***Materials & Design***, Vol. 207, (2021), 109865. https://doi.org/10.1016/j.matdes.2021.109865
3. Hesaraki, S., Nouri-Felekori, M., Nezafati, N., Borhan, S., "Preparation, characterization, and in vitro biological performance of novel porous GPTMS-coupled tragacanth/nano-bioactive glass bone tissue scaffolds", ***Materials Today Communications***, Vol. 27, (2021), 102335. https://doi.org/10.1016/j.mtcomm.2021.102335
4. Wubneh, A., Tsekoura, E.K., Ayranci, C., Uludağ, H., "Current state of fabrication technologies and materials for bone tissue engineering", ***Acta Biomaterialia***, Vol. 80, (2018), 1-30. https://doi.org/10.1016/j.actbio.2018.09.031
5. Shafiee, S., Ahangar, H. A., Saffar, A., "Taguchi method optimization for synthesis of Fe_3O_4@ chitosan/Tragacanth Gum nanocomposite as a drug delivery system", ***Carbohydrate Polymers***, Vol. 222, (2019), 114982. https://doi.org/10.1016/j.carbpol.2019.114982
6. Hajinasrollah, K., Habibi, S., Nazockdast, H., "Fabrication of gelatin–chitosan–gum tragacanth with thermal annealing cross-linking strategy", ***Journal of Engineered Fibers and Fabrics***, Vol. 14, (2019), 1558925019881142. https://doi.org/10.1177%2F1558925019881142
7. Apoorva, A., Rameshbabu, A. P., Dasgupta, S., Dhara, S., Padmavati, M., "Novel pH-sensitive alginate hydrogel delivery system reinforced with gum tragacanth for intestinal targeting of nutraceuticals", ***International Journal of Biological Macromolecules***, Vol. 147, (2020), 675-687. https://doi.org/10.1016/j.ijbiomac.2020.01.027
8. Singh, B., Sharma, K., Dutt, S., "Dietary fiber tragacanth gum based hydrogels for use in drug delivery applications", ***Bioactive Carbohydrates and Dietary Fibre***, Vol. 21, (2020), 100208. https://doi.org/10.1016/j.bcdf.2019.100208
9. Mohammadi, M. R., Kargozar, S., Bahrami, S. H., Rabbani, S., "An excellent nanofibrous matrix based on gum tragacanth-poly (ε-caprolactone)-poly (vinyl alcohol) for application in diabetic wound healing", ***Polymer Degradation and Stability***, Vol. 174, (2020), 109105. https://doi.org/10.1016/j.polymdegradstab.2020.109105
10. Lett, J. A., Sundareswari, M., Ravichandran, K., Latha, B., Sagadevan, S., "Fabrication and characterization of porous scaffolds for bone replacements using gum tragacanth", ***Materials Science and Engineering: C***, Vol. 96, (2019), 487-495. https://doi.org/10.1016/j.msec.2018.11.082
11. Rasti, M., Hesaraki, S., Nezafati, N., "Effects of GPTMS concentration and powder to liquid ratio on the flowability and biodegradation behaviors of 45S5 bioglass/tragacanth bioactive composite pastes", ***Journal of Applied Polymer Science***, Vol. 136, No. 22, (2019), 47604. https://doi.org/10.1002/app.47604
12. Shuai, C., Yu, L., Feng, P., Gao, C., Peng, S., "Interfacial reinforcement in bioceramic/biopolymer composite bone scaffold: The role of coupling agent", ***Colloids and Surfaces B: Biointerfaces***, Vol. 193, (2020), 111083. https://doi.org/10.1016/j.colsurfb.2020.111083
13. Nouri-Felekori, M., Khakbiz, M., Nezafati, N., Mohammadi, J., Eslaminejad, M. B., Fani, N., "Characterization and multiscale modeling of novel calcium phosphate composites containing hydroxyapatite whiskers and gelatin microspheres", ***Journal of Alloys and Compounds***, Vol. 832, (2020), 154938. https://doi.org/10.1016/j.jallcom.2020.154938
14. Chocholata, P., Kulda, V., Babuska, V., "Fabrication of scaffolds for bone-tissue regeneration", ***Materials***, Vol. 12, No. 4, (2019), 568. https://doi.org/10.3390/ma12040568
15. Yılmaz, E., Kabataş, F., Gökçe, A., Fındık, F., "Production and characterization of a bone-like porous Ti/Ti-hydroxyapatite functionally graded material", ***Journal of Materials Engineering and Performance***, Vol. 29, No. 10, (2020), 6455-6467. https://doi.org/10.1007/s11665-020-05165-2
16. Kokubo, T., Kushitani, H., Sakka, S., Kitsugi, T., Yamamuro, T., "Solutions able to reproduce in vivo surface-structure changes in bioactive glass-ceramic A-W3", ***Journal of Biomedical Materials Research***, Vol. 24, No. 6, (1990), 721-734. https://doi.org/10.1002/jbm.820240607
17. Feng, W., Enyan, G., Enmin, S., Ping, Z., Jinhua, L., "Structure and properties of bone-like-nanohydroxyapatite/gelatin/polyvinyl alcohol composites", ***Advances in Bioscience and Biotechnology***, Vol. 1, No,. 3, (2010), 185-189. https://doi.org/10.4236/abb.2010.13026
18. Razali, K. R., Nasir, N. M., Cheng, E. M., Mamat, N., Mazalan, M., Wahab, Y., Roslan, M. M., "The effect of gelatin and hydroxyapatite ratios on the scaffolds' porosity and mechanical properties", In ***2014 IEEE Conference on Biomedical Engineering and Sciences (IECBES)***, Kuala Lumpur, Malaysia, December 2014, IEEE, (2014), 256-259. https://doi.org/10.1109/IECBES.2014.7047497
19. Hadjidakis, D. J., Androulakis, I. I., "Bone remodeling", ***Annals of the New York Academy of Sciences***, Vol. 1092, No. 1, (2006), 385-396. https://doi.org/10.1196/annals.1365.035
20. Kora, A. J., Arunachalam, J|., "Green fabrication of silver nanoparticles by gum tragacanth (Astragalus gummifer): a dual functional reductant and stabilizer", ***Journal of Nanomaterials***, Vol. 2012, (2012), 869765. https://doi.org/10.1155/2012/869765
21. Pradini, D., Juwono, H., Madurani, K. A., Kurniawan, F., "A preliminary study of identification halal gelatin using quartz crystal microbalance (QCM) sensor", ***Malaysian Journal of Fundamental and Applied Sciences***, Vol. 14, No. 3, (2018), 325-330. https://doi.org/10.11113/mjfas.v14n3.942
22. Arunseshan, C., Suresh, S., Arivuoli, D., "Synthesis and characterization of nano-hydroxyapatite (n-HAP) using the wet chemical technique", ***International Journal of Physical Sciences***, Vol. 8, 32, (2013), 1639-1645. https://doi.org/10.1016/j.compositesa.2008.05.018

Advanced Ceramics Progress: Vol. 8, No. 1, (Winter 2022) 27-35

Materials and Energy Research Center
MERC

Contents lists available at ACERP

Advanced Ceramics Progress

Journal Homepage: www.acerp.ir

Original Research Article

Characterization of Iranian Ancient Colored Glazed Ceramic Tiles of Safavid Era

Javad Fahim [a], Ebrahim Ghasemi [b,*], Maryam Hosseini Zori [c]

[a] *PhD, Department of Mechanical Engineering, Faculty of Mechatronics, Karaj Branch, Islamic Azad University, Karaj, Alborz, Iran*
[b] *Associate Professor, Department of Inorganic Pigments and Glazes, Faculty of Dyes and Pigments, Institute for Color Science and Technology (ICST), Tehran, Tehran, Iran*
[c] *Assistant professor, Department of Inorganic Pigments and Glazes, Faculty of Dyes and Pigments, Institute for Color Science and Technology (ICST), Tehran, Tehran, Iran*

* Corresponding Author Email: eghasemi@icrc.ac.ir (E. Ghasemi)

URL: https://www.acerp.ir/article_151935.html

ARTICLE INFO

Article History:

Received 1 May 2022
Received in revised form 17 June 2022
Accepted 19 June 2022

Keywords:

Egyptian Green
Safavid Era
Glazed Ceramics
Tiles
Copper

ABSTRACT

Investigation of the chemical compositions of pigments in glazed ancient ceramic tiles is of great importance from the monuments restoration point of view. In this regard, the current research aimed to investigate the chemical compositions and color charactristics of pigments in six glazed ancient ceramic tiles (Samples B1-B6) collected from Abdolazim Hasani Shrine (Safavid era), Ray, Iran. The results from X-ray Probe Micro Analyzer (XPMA), X-Ray Diffraction (XRD) patterns, and Energy Dispersive X-ray Spectroscopy (EDS) spectra revealed that the glazes were silica-based, containing 38.85 to 50.89 wt. % silicon in Samples B3 and B1, respectively, with lime, quarts, wollastonite, and cristobalite as the main phases. Raman spectroscopy also confirmed the presence of quartz, wollastonite, and tridymite along with chalk, gypsum, calcite, copper oxide, and green earth. The particle sizes of the pigments measured through Scanning Electron Microscopy (SEM) varied from 0.6 µm in Sample B1 to 5.5 µm in Sample B3. High intensity reflectance was also observed in the range of 490-560 nm, confirming the green color of the samples with different shades. In addition, CIE L*a*b* parameters clearly showed the correlation between the green color and concentration of Cu^{2+} ions within the silica-rich amorphous phase. Therefore, the presence of wollastonite, tridymite, and copper oxide in the samples under study was obviously indicative of presence of Egyptian green pigments in the glazes.

https://doi.org/10.30501/acp.2022.339876.1088

1. INTRODUCTION

Undoubtedly, Safavid era in Iran (1501-1732) is known as a period of shiny colored ceramic glazes in the world. However, the history of colored glazes dates back to ancient Egypt 4000 BC [1]. The variety of colors and geometries of the tiles flourished in the Safavid era. Unfortunately, there are very few limited papers of references investigating the compositions, colors, and glazes of ceramic tiles from the Safavid heritage. Most glazed ceramics inherited from the ruling period of Safavid dynesty are in blue or green-blue color.

Throughout the old kingdom (2600BC), Egyptian artisans fabricated a blue pigment, called the Egyptian blue, which is a mixture of calcium, silicon, and copper along with a soda flux. This pigment was used instead of

Please cite this article as: Fahim, J., Ghasemi, E., Hosseini Zori, M., "Characterization of Iranian Ancient Colored Glazed Ceramic Tiles of Safavid Era", ***Advanced Ceramics Progress***, Vol. 8, No. 1, (2022), 27-35. https://doi.org/10.30501/acp.2022.339876.1088

lapis-lazuli all around the Mediterranean region. However, the fabrication technology of the menyioned pigment was lost after the seventh century AD [2]. On the contrary, the synthetic pigment called the Egyptian green was produced from different proportions of the same components used for fabricating the Egyptian blue pigment [3–6]. As known, the diversity of production conditions (firing temperature, atmosphere, and cooling rate [6]) significantly affects the resulting properties of the pigment; however, a silicate enriched compound is expected as a final product. There are no ancient recipes available for the production of this green pigment [5]. Pagés-Camagna et al. [6] identified this type of pigment in a number of ceramic tiles from the Old Kingdom (3rd Millennium BCE) to the 21st Dynasty (10th Century BCE). Ullrich [7] discovered the Egyptian Green color on the bust of Nefertiti excavated at Tell el Amarna in the Tomb of Tutankhamen.

Bianchetti et al. [8] studied the fabrication of Egyptian blue and green frit using pure chemicals and natural raw Egyptian materials under different experimental conditions. They also pointed to the dependency of the recorded colors on the chemical composition and melting conditions.

A number of researchers produced a green pigment similar to para-wollastonite ($CaSiO_3$) together with a copper-bearing glass phase by altering the fabrication conditions to obtain Egyptian blue and subsequently Egyptian green [3-6]. Egyptian green (green frit) is a heterogeneous material characterized by the presence of para-wollastonite which is stable at 950-1150 °C [9]. It is a complex pigment which is usually obtained from Egyptian blue pigment $CaCuSi_4O_{10}$ (cuprorivaite) by heating CuO, $CaCO_3$, SiO_2, and Na_2CO_3 at the tempratures above 1000 ºC [10].

Pagés-Camagna et al. [6] investigated the production of Egyptian green pigments and analyzed the chemical and structural properties of raw Egyptian blue and green pigment cakes and pigment samples taken from paintings kept in the Louvre Museum, France. In their research, they took into account the role of firing temperature, atmospheric conditions in the furnace, and cooling rate. Demidenko et al. [11] investigated the microstructure of a material based on natural wollastonite at different sintering temperatures ranging from 850 °C to 1100 °C. They also studied the effect of microstructure on the porosity, shrinkage, water absorption, and mechanical strength.

Pagés-Camagna et al. [12] studied the Egyptian blue and green pigments in archaeological samples using Scanning Electron Microscopy (SEM) images and Raman spectroscopy. They could finally identify tenorite (CuO), confirming that the synthesis of both pigments could be performed in an oxidizing atmosphere. In another research, Pagés-Camagna et al. [13] reported some valuable information on the coloring mechanism of Egyptian blue and green pigments.

Dabanlı et al. [14] investigated the samples of glazed tiles belonging to a monument located in Southeastern Anatolia. They concluded that alkali and lead oxides were the main components of glazes along with small amounts of lead oxide. They also found that the blue/green turquoise colors were obtained from copper while the blue pigment itself was derived from cobalt. Omar [15] investigated the body and glaze layer of the Sapil (public fountain) and Kuttab (school) of Mustafa Sinan monuments. The results from tiles analysis proved the application of local clay mixed with a small amount of lime. They also stated that the alkaline and lead oxides were the main components of the glaze layer with high amount of lead oxide in samples. In addition, the obtained results confirmed the presence of copper oxide contributing to the creation of light blue and green color in the samples under study.

In this research, six samples obtained from green-blue glazed ancient ceramic tiles from Abdolazim Hasani Shrine, Ray, Iran, inherited from the Safavid era (1501-1736) were collected to identify the chemical compositions and nature of their pigments through analytical techniques. In characterizing ancient colored glazes, the pigments in the glaze were identified and investigated through different analytical methods based on available scientific references. The main objective of this study was to determine whether or not the nature of green-blue color pertained to the Egyptian blue.

2. MATERIALS AND METHODS

2.1. Materials

Six green-blue glazed samples, shown in Figure 1, were collected from ancient potteries belonging to the Safavid era from different parts of Abdolazim Hasani Shrine, Ray, Iran.

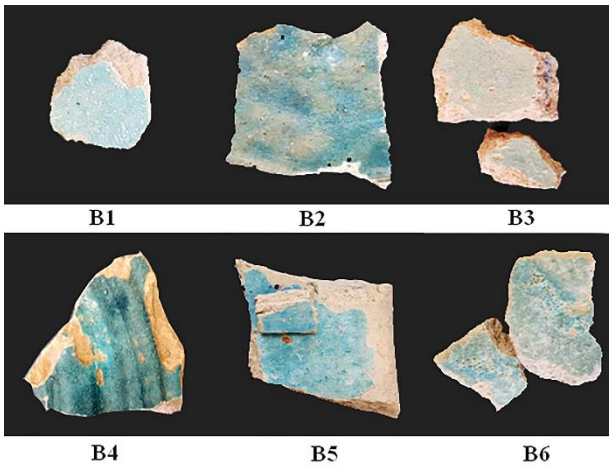

Figure 1. The glazed samples from different parts of Abdolazim Hasani Shrine

2.2. Methods

Followed by collecting the samples, a thin layer of glaze was mechanically removed from their surfaces. The chemical compositions of the samples were analyzed using X-Ray Probe Micro Analyzer (XPMA, HORIBA XGT7200). In addition, the phase composition was characterized through X-ray Diffraction (XRD, Panalytical Expert) method using Cu Kα radiation (λ=1.54 Å). The microscopic studies were performed using SEM (FEI ESEM QUANTA 200) coupled with Energy Dispersive X-ray spectroscopy (EDS, EDAX EDS Silicon Drift, 2017) using Backscattered Electron Emission (BSE). Raman studies on the colored glazed samples were carried out using Confocal Raman Microscope (Xplora Plus, Horiba Co., France). In addition, FTIR studies were carried out using PerkinElmer spectrometer (Spectrum One FTIR, USA). The reflectance spectra were recorded using a 4500L Hunter Lab Mini Scan EZ spectrophotometer. The chromatic values were then expressed as CIE L*a*b*color coordinates under D65/10º Illuminant in the spectral range of 400-700 nm.

Considerations of the Raman spectroscopy calibration were as follows:

Part 1- Calibrating the zero-order position:

The ZERO parameter changed in small increments, e.g., +5 or -5 at a time, considered as the number of nm moving per motor.

Part 2- Calibrating the Raman spectrum:

This calibration stage was done using a known emission line from a Mercury or Neon lamp. Then, the Laser wavelength was altered, and the XY stage movement and Laser Spot Position were calibrated. Finally, the required software for data analysis was installed.

3. RESULTS AND DISCUSSION

3.1. Chemical Composition

Table 1 presents the results from the XPMA analysis (chemical compositions of the elements in glaze samples, and Figure 2 lists the concentration values of the detected elements (in wt. % of their oxides) in Samples B1-B6.

In addition to creating a white hue color, CaO can increase the resistance of the glaze matrix to water, acid, and surface scratches. It also improves the adhesion of glaze to the substrate. It is well known that the copper oxide in ceramics usually creates a green shade; however, in the presence of alkaline and alkaline earth metal oxides such as calcium oxide, potassium oxide, and sodium oxide, it produces blue and green-blue shades [16].

As observed, SiO_2 is the main phase in all samples along with Al_2O_3, Cu_2O, as well as alkaline and alkaline earth metal oxides (i.e. CaO and Na_2O, and K_2O).

TABLE 1. The chemical composition of the elements in the glaze samples B1-B6. The magnitude is as wt. %

	B1	B2	B3	B4	B5	B6
Na_2O	-	13.59	11.94	0.00	0.00	12.64
MgO	0.01	0.01	0.03	0.03	0.00	0.02
Al_2O_3	5.40	3.22	3.58	7.87	2.01	4.89
SiO_2	81.60	73.77	71.46	76.40	85.18	72.54
SO_3	0.18	0.15	0.28	0.15	0.02	0.16
K_2O	1.24	3.35	2.55	3.80	4.49	2.70
CaO	9.87	4.95	8.39	7.10	5.71	5.48
TiO_2	0.02	0.03	0.04	0.03	0.01	0.04
MnO_2	0.06	0.14	0.14	0.06	0.06	0.04
Fe_2O_3	0.18	0.14	0.55	0.17	0.07	0.27
CuO	1.12	0.60	1.00	3.69	1.33	1.18
ZnO	0.10	0.00	0.00	0.06	0.04	0.00
SrO	0.05	0.04	0.04	0.04	0.03	0.05
PbO	0.16	0.00	0.00	0.61	1.09	0.00

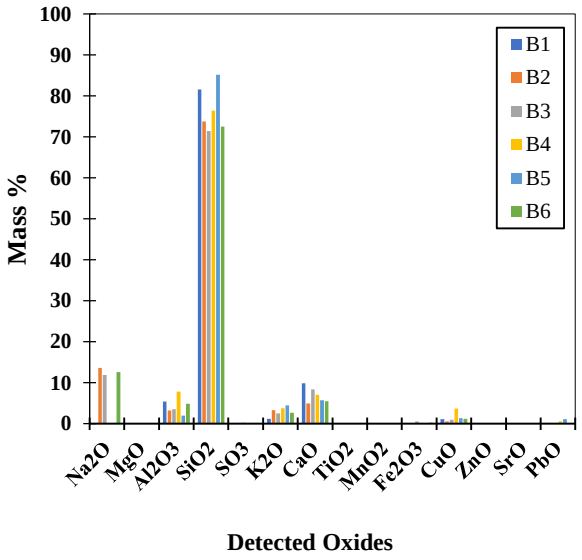

Figure 2. XPMA results demonstrating the concentrations of the detected elements in Samples B1-B6

3.2. X-Ray Diffraction

Table 2 summarizes the main phases identified from the XRD patterns of Samples B1-B6, and Figure 3 demonstrates the XRD Pattern of the ancient colored glazed Samples B1-B6.

TABLE 2. Detected phases in Samples B1-B6

Sample	Main Phases	Chemical Formula
B1	No crystalline phase	-
B2	No crystalline phase	-
B3	Wollastonite, Quartz, lime	$CaSiO_3$, SiO_2, CaO
B4	Wollastonite	$CaSiO_3$
B5	Quartz, lime, Cristobalite	SiO_2, CaO,SiO_2
B6	Quartz, Cristobalite	SiO_2, SiO_2

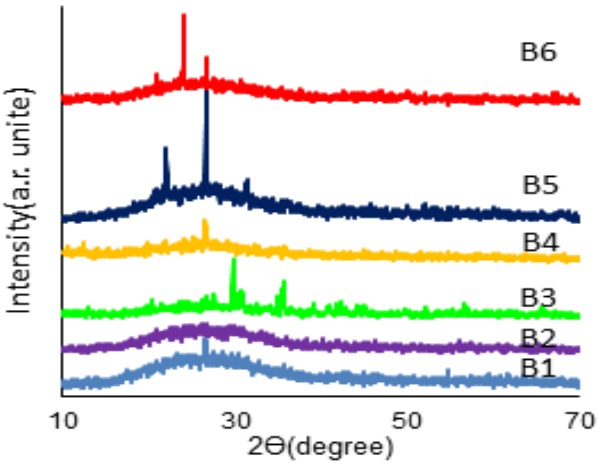

Figure 3. XRD Pattern of the ancient colored glazed Samples B1-B6

While no crystalline phases are observed in the XRD patterns of these samples, three mineral phases of lime, quartz, and wollastonite (calcium silicate) were detected in Sample B3. According to the findings, Sample B4 was only composed of wollastonite phase B3. The presence of wollastonite in the colored glazes can be important evidence for the presence of Egyptian green pigments in the glaze formulation [6,10,16]. The XRD patterns of Samples B5 and B6 also confirm the presence of quartz, lime, and cristobalite. However, the wollastonite phase in these samples was not detected due to its low concentration. As mentioned in the methodology section, the procedure of the separation of glaze from the surface of ceramics was in such a way that the adhesion of the body to the glaze should be probable. This is why some parts of glaze are crystalline while some others are not.

As reported by Pagés-Camagna et al. [6], Egyptian green glazes must have been fired at higher temperatures than Egyptian blue ones. As a result, the cristobalite phase can be identified in the Egyptian green glazes. In other words, cristobalite can be the considered as a main characteristic of Egyptian green [6,10,16].

3.3. Microstructure

Figure 4 demonstrates the SEM images of the six samples according to which, the samples are porous with heterogeneous microstructure. Small white pigment particles (0.6 µm for samples B1 and B6, 1.25 µm for samples B2 and B5, 4.5 µm for sample B4, and 5.5 µm for sample B3) are recognizable on the surface of the glaze that was eroded due to the aging and long-term exposure to severe environmental conditions such as wind. In Sample B3, the glaze surface has many bubbles, hence not uniform, and there is a significant difference between the erosion of the glaze matrix and that of other phases such as quartz and wollastonite. Samples B1 and B2, however, have a relatively uniform eroded surface. Higher degrees of erosion is observed on the surface of Samples B3 to B6 probably due to the presence of crystalline phases in the glazed ceramic tiles.

SEM-EDS results for the glaze matrix and white particles (shown as white spots in Figure 4) are presented in Tables 3 and 4, respectively.

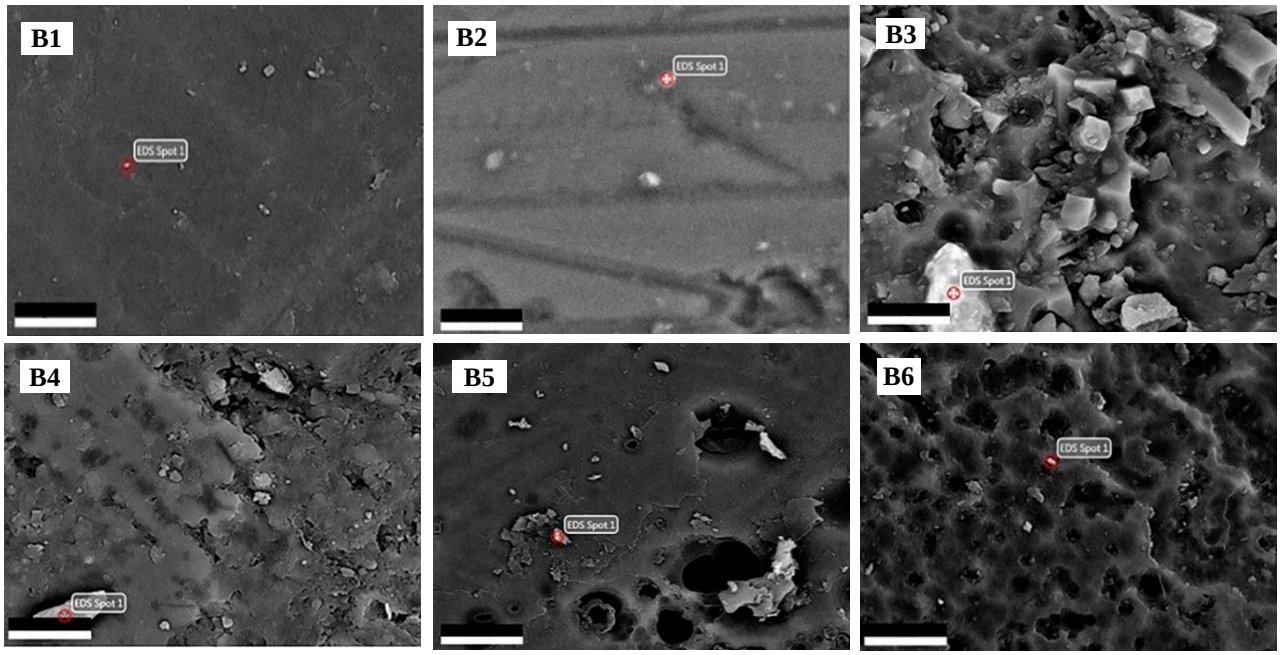

Figure 4. Back-scattered SEM images of the glazed samples at 5000X. EDS spots are shown in each image. The scale bar is 5 µm

TABLE 3. EDS analysis of the glaze matrix (wt. %)

Sample	O	Na	Mg	Al	Si	K	Ca	Fe	Cu	Sn
B1	23.55	3.29	1.41	3.62	50.89	2.46	7.71	3.78	3.28	-
B2	25.27	9.49	2.44	2.84	45.25	4.81	6.07	1.31	2.52	-
B3	29.94	4.66	3.78	3.3	38.85	2.5	9.79	4.53	2.64	-
B4	28.58	5.03	3.62	5.74	39.58	3.69	4.99	2.27	6.5	-
B5	27.2	4.83	1.86	2.47	46.29	6.24	6.93	0.94	3.24	-
B6	20.95	7.6	1.94	3.1	49.62	3.92	5.93	1.79	5.14	-
Average	25.9	5.8	2.5	3.5	45.1	3.9	6.9	2.4	3.9	-
Standard Deviation	3.3	2.3	1.0	1.2	5.0	1.4	1.7	1.4	1.6	-

TABLE 4. EDS analysis of white particles shown in the SEM images in Figure 4 (wt. %)

Sample	O	Na	Mg	Al	Si	K	Ca	Fe	Cu	Sn
B1	25.1	8.4	4.3	3.2	46.3	1.6	6.8	1.0	2.1	-
B2	24.8	10.0	3.3	2.9	36.6	2.9	4.1	13.3	2.0	-
B3	12.4	4.8	1.2	1.5	20.4	1.0	3.4	1.6	1.4	52.3
B4	31.6	6.9	4.4	5.0	38.6	2.9	5.1	2.0	3.5	-
B5	33.5	6.1	2.6	3.5	41.1	4.6	5.2	0.81	2.6	-
B6	30.3	8.8	3.1	3.5	36.4	2.7	10.9	1.1	3.3	-
Average	26.3	7.5	3.1	3.3	36.6	2.6	5.9	1.6	2.6	26.3
Standard Deviation	7.7	1.9	1.2	1.1	8.7	1.2	2.7	1.0	0.8	7.7

The average and standard deviations are also compared in Figure 5. According to this figure, the glazes are silica-based containing different amounts of silicon from 38.85 to 50.89 wt. % for Samples B3 and B1, respectively. The glazes also contain other alkaline and alkaline earth elements such as calcium, sodium, and potassium. Copper was also detected in all the samples ranging from 2.52 wt. % for sample B2 to 6.5 wt. % for sample B4.

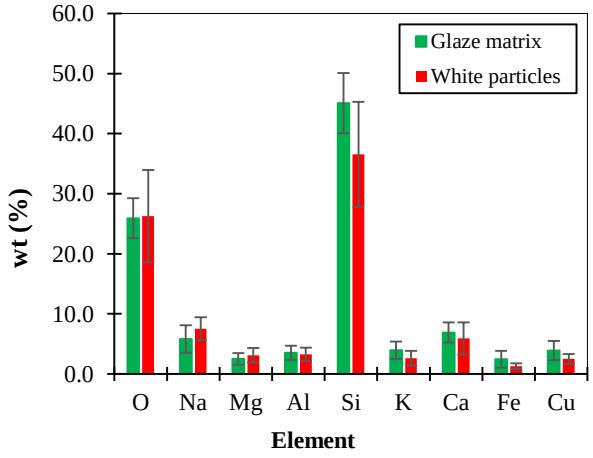

Figure 5. Comparison between the average and standard deviations of different elements in the glaze matrix and white particles, as listed in tables 3 and 4

According to Figure 5, the concentration of silicon in the white particles (46.34 wt. %) is lower than that in the glaze matrix (e.g. for sample B1, 46.34 wt. % and 50.89 wt. %, respectively). The same trend was also observed for Al, K, Ca, Fe, and Cu elements in all six samples. The higher Fe content of white particles in Sample B2 is inicative of the fabrication of this pigment using iron-rich raw materials

Sample B3 contained high concentration of tin (52.34 wt. %) probably due to the presence of tin in the copper source (e.g., tin bronze). Oudbashi et al. [17] also reported the presence of tin element in their samples. White particles in Sample B6 contained calcium with high concentration of about 10.86 % which may be attributed to the utilization of Ca-rich raw materials such as calcite ($CaCO_3$) or CaO in the fabrication of this pigment.

The distribution of the constituents in the glaze matrix and white particles was also investigated for Sample B2, as a representative sample, using line scan and element profile plot, as shown in Figure 6.

As observed, while moving from point A to point B, the concentration of Si (in wt. %) decreased until reaching a white particle and then increased again in the Si-rich matrix. Since white particle is supposed to be an Egyptian green pigment (calcium silicate), the silicon concentration decreased while those of Ca and O increased. Evidently, copper has uniform distribution throughout the sample (i.e., both glaze matrix and white particles). The same trend was observed for these elements in other five samples that are not shown here.

The CaO/CuO ratio can be caluclated using SEM-EDS analysis of bulk compositions of the glazed samples given in Table 5 where it is observed that the bulk lime concentration is normally greater than that of the bulk copper oxide. Of note, the CaO/CuO ratio is greater than 1.5. However, due to loss of material through weathering and possible contamination during ancient discoveries, the differences in the CaO/CuO ratios are less explicit in some samples. The obtained results are in accordance with the results obtained by Hatton et al. [18].

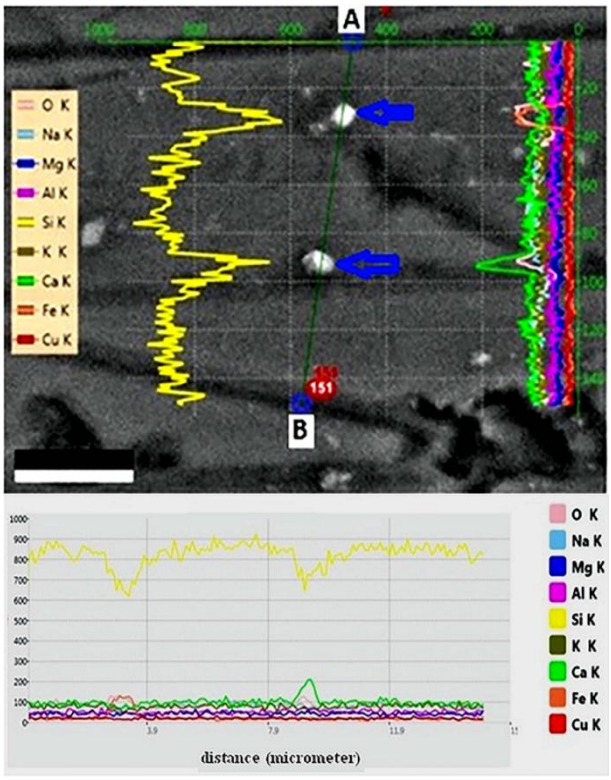

Figure 6. Line scan and element profile plot of glaze matrix and white particles for B2 sample

Another noticeable feature is that these samples contain high concentration of soda (Na_2O). Moreover, in this research, the green-blue colored glaze samples are characterized by high flux concentrations, i.e., Na_2O plus K_2O between 5.3 % and 14.1 %, respectively, in Samples B1 and B2. This result is also in agreement with the results obtained by Pagés-Camagna et al. [6].

3.4. Raman Spectroscopy

Raman spectroscopy was used for the characterization of the ancient green-blue glazed samples. It is a reliable, fast, sensitive and nondestructive test method which measures different vibrational modes, thus providing complementary information on the analyzed materials. Figure 7 shows the Raman spectroscopy spectra of the glazed samples. Two weak bands are observed at 150 cm^{-1} and 180 cm^{-1} mainly due to the presence of chalk [19] and gypsum [20], respectively. The peak at around 260 cm^{-1} is attributed to the wollastonite crystalline phase [21] which is usually found in Egyptian green pigment used in the ancient glazed ceramic tiles. The weak bands around 406 cm^{-1}, 391 cm^{-1}, and 253 cm^{-1} are also attributed to ν(Cu-Cl) stretching [22], ν(O-Cu-O) symmetric stretching, and ν(O-Cu-O) bending [23], respectively. The bands at around 300 cm^{-1} and 360 cm^{-1} correspond to copper oxide [24] while those around at 350 cm^{-1} and 380 cm^{-1} belong to quartz [25-27]. In addition, the band around at 360 cm^{-1} is attributed to calcite [28,29].

There are two bands at around 425 cm^{-1} and 460 cm^{-1} which can be attributed to the tridymite [21] and quartz [25-29], respectively. Bianchetti et al. [8] reported that tridymite was a dominant crystalline phase in the Egyptian green pigment that was produced at temperatures higher than 950 ºC.

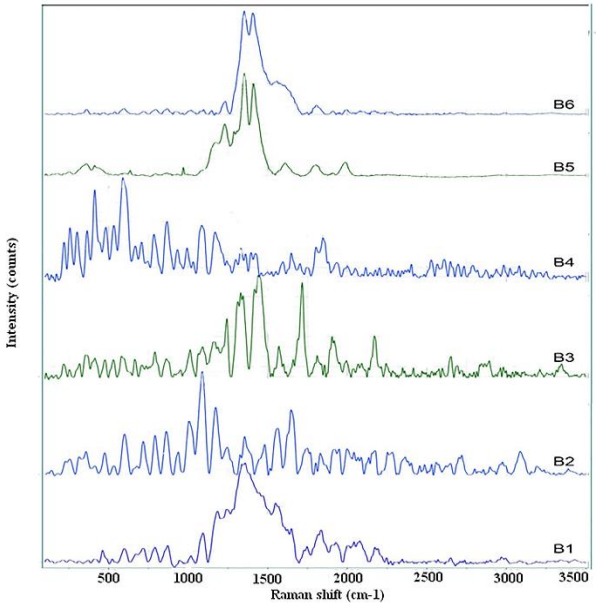

Figure 7. Raman spectra of the B1-B6 glazed samples

The two bands at around 470 cm^{-1} and 750 cm^{-1} in Sample B3 is associated with the SnO_2 [30] due to the presence of about 52.34 wt. % tin in white particles. In addition, there are other weak and medium bands at around 540 cm^{-1} and 710 cm^{-1} which belong to the green earth [31] while those at 590 cm^{-1} and 600 cm^{-1} correspond to the Egyptian green [20,32] and copper oxide [24], respectively. Raman bands at around 717 cm^{-1}, 780cm^{-1} , 865 cm^{-1}, 930 cm^{-1}, and 940 cm^{-1} are attributed to the calcite [28, 29], tridymite [21], allophone [33,34], and chrysocolla [35], respectively.

In contrast to the XRD patterns according to which, cristobalite phase was only detected in Samples B5 and B6, this phase was found in Samples B1-B6 according to Raman bands at around 410 cm^{-1}, 420 cm^{-1}, 598 cm^{-1}, 780 cm^{-1}, 790 cm^{-1}, and 1075 cm^{-1} [36-38], respectively, thus confirming the presence of the Egyptian green pigment in the formulation of all the investigated ancient glazed ceramic tiles. The bands at 1020 cm^{-1}, 1085 cm^{-1}, and 1170 cm^{-1} can be attributed to the wollastonite [32], calcite [28-29], and quartz [26-29], respectively.

Moreover, the Raman bands at around 1235 cm^{-1}, 1356 cm^{-1}, and 1458 cm^{-1} correspond to the Green earth [31]. The weak and medium peaks at around 1445 cm^{-1} and 1550 cm^{-1} may also be attributed to the Verdigris [39]

TABLE 5. Bulk Chemical compositions of green-blue colored glaze samples (EDS analysis normalized to 100 %)

Sample Code	SiO_2	CuO	CaO	Na_2O	K_2O	MgO	Al_2O_3	Fe_2O_3	CaO/CuO
B1	62.99	3.14	5.82	2.64	2.69	0.96	13.43	8.31	1.85
B2	61.62	2.65	5.04	8.39	5.78	1.72	11.59	3.17	1.89
B3	53.95	2.83	8.30	4.20	3.06	2.73	13.74	11.17	2.92
B4	51.12	2.60	3.94	4.22	4.21	2.43	22.26	5.21	1.51

while the band at around 1480 cm^{-1} results from the vibration stretching of C-C bond [40]. Of note, the Raman bands at around 17549 cm^{-1} and 1940 cm^{-1} may be attributed to C-O vibration stretching [41] while the band at around 1645 cm^{-1} can be associated with the OH stretching mode in water. Moreover, the Raman bands in the range of 2000-4000 cm^{-1} are attributed to the vibration stretching of hydroxyl and water [42,43].

3.5. Colorimetry

Figure 8 and Table 6 present the reflectance spectra and CIE L*a*b* values of the studied ancient glazed ceramic tiles, respectively. Table 6 also lists the average values of a* and b*. As observed in Figure 8, there is a high intensity reflectance spectrum in the range of 490-560 nm. Therefore, it can be concluded that the samples are green with different hues.

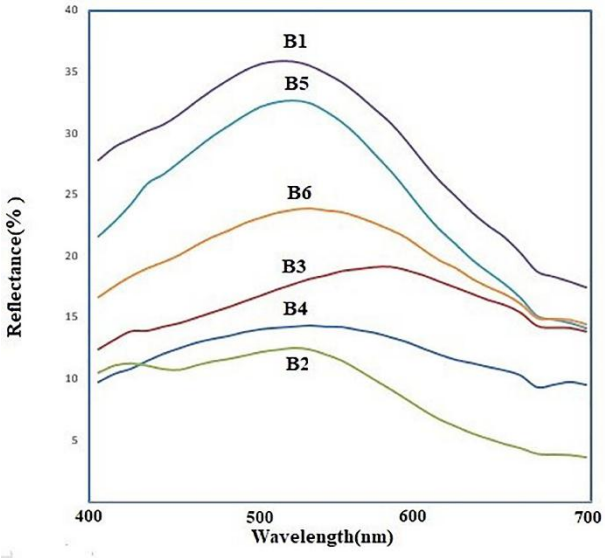

Figure 8. Reflectance spectra of the green-blue glazed samples

TABLE 6. Colorimetric parameters (L*a*b*) of the ancient glazed ceramic tiles based on D65 observer

Sample	L*	a*	b*	c	Cu (wt. %)
B1	63.53	-10.49	0.44	10.5	3.28
B2	38.39	-11.78	-2.41	12.03	2.52
B3	49.47	-2.45	7.15	7.55	2.64
B4	43.48	-5.38	2.7	6.02	6.5
B5	60.47	-12.47	1.31	12.54	3.24
B6	54.27	-6.95	3.67	7.86	5.14

The copper concentration in the raw material plays an important role in achieving better green shades (higher a* and c* values) in these glazes. For example, c* = 12.5 and c* = 10.5 were obtained for 3.2 wt. % and 3.3 wt. % copper in Sample B5 and B1, respectively. On the contrary, Cu contents higher than this value (3.3) produce a poor green shade (e.g. c* = 6 and c* = 7.86 for 6.5 wt. % and 5.14 wt. % copper in Samples B4 and B6. The same results were obtained for copper contents lower than 3.3 wt. % (for example, in Sample B3). In Sample B2 (Cu = 2.52 wt. % and c* = 12.03), however, the pigment is Egyptian blue since b* = -2.41. To be specific, the green color is produced due to the presence of Cu^{2+} metallic ion in an octahedral structure in the amorphous silica-rich matrix [44].

4. CONCLUSION

In this research, six green-blue ancient glazed ceramic tiles collected from Abdolazim Hasani Shrine, Ray, Iran, were investigated using the XPMA, XRD, FTIR, and Raman spectroscopy. The obtained results confirmed the presence of three main phases of tridymite, cristobalite, and wollastonite, the main constituents of Egyptian green pigments. Colorimetry analysis confirmed that the presence of Cu^{2+} ion in an octahedral structure within amorphous silica-rich matrix was responsible for the observed green hue. In addition, the SEM-EDS revealed the uniform and homogeneous distribution of copper throughout the glaze matrix.

ACKNOWLEDGEMENTS

We would like to express our gratitude to Iran National Science Foundation (INSF) for supporting this research under grant no. 98027092, and from Institute for color science and technology (ICRC) who provided facilities that greatly assisted the research.

REFERENCES

1. Mokhtarshahi Sani, R., "A Conceptual Understanding for Teaching the History of Islamic Architecture: An Iranian (Persian) Perspective", ***International Journal of Architectural Research***, Vol. 3, No. 1 , (2009), 233-244. https://www.researchgate.net/publication/26597708_A_Conceptual_Understanding_for_Teaching_the_History_of_Islamic_Arch

itecture_An_Iranian_Persian_Perspective/fulltext/0e605659f0c46d4f0ab1bf3e/A-Conceptual-Understanding-for-Teaching-the-History-of-Islamic-Architecture-An-Iranian-Persian-Perspective.pdf?origin=publication_detail
2. Delamare, F., "Sur les processus physiques intervenant lors de la synthèse du bleu égyptien: Réflexion à propos de la composition de pigments bleus gallo-romains", ***ArchéoSciences, revue d'Archéométrie***, Vol. 21, No. 1, (1997), 103-119. https://doi.org/10.3406/arsci.1997.952
3. Eastaugh, N., Walsh, V., Chaplin, T., Siddall, R., ***Pigment Compendium: A Dictionary and Optical Microscopy of Historical Pigments***, Burlington, VT, Butterworth-Heinemann, (2008). https://doi.org/10.4324/9780080943596
4. Scott, D. A., ***Copper and Bronze in Art: Corrosion, Colorants, Conservation***, Getty Publications, (2002). https://www.getty.edu/publications/virtuallibrary/temp/9780892366385.pdf
5. Wiedemann, H. G., Bayer, G., "The bust of Nefertiti", ***Analytical Chemistry***, Vol. 54, No. 4, (1982), 619A-628A. https://doi.org/10.1021/ac00241a790
6. Pagés-Camagna, S., Colinart, S., "The Egyptian Green pigment: Its manufacturing process and links to Egyptian Blue", ***Archaeometry***, Vol. 45, No. 4, (2003), 637-658. https://doi.org/10.1046/j.1475-4754.2003.00134.x
7. Ullrich, D., "Egyptian Blue and Green Frit: Characterization, History and Occurrence, Synthesis", In ***Pact***, Vol. 17, No. II.3.1, (1987), 323-332. http://www.univeur.org/cuebc/downloads/Pubblicazioni%20scaricabili/PACT%2017%20-%20Datation-Caract%C3%A9risation%20des%20peintures%20pari%C3%A9tales%20et%20murales/16%20Ullrich.pdf
8. Bianchetti, P., Talarico, F., Viglianoa, M. G., Ali, M. F., "Production and characterization of Egyptian blue and Egyptian green frit", ***Journal of Cultural Heritage***, Vol. 1, No. 2, (2000), 179-188. https://doi.org/10.1016/S1296-2074(00)00165-5
9. Abdel-Ghani, M. H., ***A Multi-Instrument Investigation of Pigments, Binders and Varnishes from Egyptian Paintings (AD 1300-1900): Molecular and Elemental Analysis Using Raman, GC-MS and SEM-EDX Techniques***, Doctoral dissertation, University of Bradford, (2009). http://hdl.handle.net/10454/4315
10. Gražėnaitė, E., Kiuberis, J., Beganskienė, A., Senvaitienė, J., Kareiva, A., "XRD and FTIR characterization of historical green pigments and their lead-based glazes", ***Chemija***, Vol. 25, No. 4, (2014), 199–205. http://mokslozurnalai.lmaleidykla.lt/publ/0235-7216/2014/4/199%E2%80%93205.pdf
11. Demidenko, N. I., Tel'nova, G. B., "Microstructure and properties of a material based on natural wollastonite", ***Glass and Ceramics***, Vol. 61, No. 5-6, (2004), 183-186. https://doi.org/10.1023/B:GLAC.0000043088.65135.11
12. Pagès-Camagna, S., Colinart, S., Coupry, C., "Fabrication Processes of Archaeological Egyptian Blue and Green Pigments Enlightened by Raman Microscopy and Scanning Electron Microscopy", ***Journal of Raman Spectroscopy***, Vol. 30, No. 4, (1999), 313-317. https://doi.org/10.1002/(SICI)1097-4555(199904)30:4<313::AID-JRS381>3.0.CO;2-B
13. Pagès-Camagna, S., Reiche, I., Brouder, C., Cabaret, D., Rossano, S., Kanngießer, B., Erko, A., "New insights into the color origin of archaeological Egyptian blue and green by XAFS at the Cu K-edge", ***X-Ray Spectrometry: An International Journal***, Vol. 35, No. 2, (2006), 141-145. https://doi.org/10.1002/xrs.885
14. Dabanlı, Ö., Yıldız, D., Bayazit, M., "Composition and Phase Analysis On Glazed Tiles of Southeast Anatolia: Production Process Identification", ***Mediterranean Archaeology & Archaeometry***, Vol. 21, No. 3, (2021), 1-22. https://doi.org/10.5281/zenodo.5545709
15. Omar, S., "Characterization of The Ottoman Ceramic Tiles in the Facade of Mustafa Sinans Sapil (Cairo, Egypt)", ***Scientific Culture***, Vol. 8, No. 2, (2022), 1-15. https://doi.org/10.5281/zenodo.6323156
16. Mahmoud, H. M., Papadopoulou, L., "Archaeometric Analysis of Pigments from the Tomb of Nakht-Djehuty (TT189), El-Qurna Necropolis, Upper Egypt", ***ArcheoSciences, Revue d'archéométrie***, Vol. 37, (2013), 19-33. https://doi.org/10.4000/archeosciences.3967
17. Oudbashi, O., Hessari, M., "A "western" imported technology: An analytical study of the Achaemenid Egyptian blue objects", ***Journal of Cultural Heritage***, Vol. 47, (2021), 246-256. https://doi.org/10.1016/j.culher.2020.11.001
18. Hatton, G. D., Shortland, A. J., Tite, M. S., "The production technology of Egyptian blue and green frits from second millennium BC Egypt and Mesopotamia", ***Journal of Archaeological Science***, Vol. 35, No. 6, (2008), 1591-1604. https://doi.org/10.1016/j.jas.2007.11.008
19. Ion, R. M., Turcanu-Caruţiu, D., Fierăscu, R. C., Fierăscu, I., Bunghez, I. R., Ion, M. L., Teodorescu, S., Vasilievici, G., Rădiţoiu, V., "Caoxite-hydroxyapatite composition as consolidating material for the chalk stone from Basarabi–Murfatlar churches ensemble", ***Applied Surface Science***, Vol. 358, (2015), 612-618. https://doi.org/10.1016/j.apsusc.2015.08.196
20. Charola, A. E., Pühringer, J., Steiger, M., "Gypsum: a review of its role in the deterioration of building materials", ***Environmental Geology***, Vol. 52, No. 2, (2007), 339-352. https://doi.org/10.1007/s00254-006-0566-9
21. Coccato, A., Bersani, D., Coudray, A., Sanyova, J., Moens, L., Vandenabeele, P., "Raman spectroscopy of green minerals and reaction products with an application in Cultural Heritage research", ***Journal of Raman Spectroscopy***, Vol. 47, No. 12, (2016), 1429-1443. https://doi.org/10.1002/jrs.4956
22. Frost, R. L., Martens, W., Kloprogge, J. T., Williams, P. A., "Raman spectroscopy of the basic copper chloride minerals atacamite and paratacamite: implications for the study of copper, brass and bronze ceramic tiles of archaeological significance", ***Journal of Raman Spectroscopy***, Vol. 33, No. 10, (2002), 801-806. https://doi.org/10.1002/jrs.921
23. Liu, X. D., Hagihala, M., Zheng, X. G., Guo, Q. X., "Vibrational spectroscopic properties of botallackite-structure basic copper halides", ***Vibrational Spectroscopy***, Vol. 56, No. 2, (2011), 177-183. https://doi.org/10.1016/j.vibspec.2011.02.002
24. Deng, Y., Handoko, A. D., Du, Y., Xi, S., Yeo, B. S., "In Situ Raman Spectroscopy of Copper and Copper Oxide Surfaces during Electrochemical Oxygen Evolution Reaction: Identification of CuIII Oxides as Catalytically Active Species", ***Acs Catalysis***, Vol. 6, No. 4, (2016), 2473-2481. https://doi.org/10.1021/acscatal.6b00205
25. Gillet, P., Le Cléac'h, A., Madon, M., "High-temperature raman spectroscopy of SiO_2 and GeO_2 Polymorphs: Anharmonicity and thermodynamic properties at high-temperatures", ***Journal of Geophysical Research: Solid Earth***, Vol. 95, No. B13, (1990), 21635-21655. https://doi.org/10.1029/JB095iB13p21635
26. Gillet, P., "Raman spectroscopy at high pressure and high temperature. Phase transitions and thermodynamic properties of minerals", ***Physics and Chemistry of Minerals***, Vol. 23, No. 4, (1996), 263-275. https://doi.org/10.1007/BF00207767
27. Hemley, R. J., "Pressure Dependence of Raman Spectra of SiO_2 Polymorphs: α-Quartz, Coesite, and Stishovite", In Manghnani, M. H. and Syono, Y. (Eds.), ***High-Pressure Research in Mineral Physics: A Volume in Honor of Syun-iti Akimoto***, Tokyo, Terra Scientific Publishing Company (TERRAPUB), Washington D.C., American Geophysical Union, Vol. 39, (1987), 347-359. https://doi.org/10.1029/GM039p0347
28. De La Pierre, M., Carteret, C., Maschio, L., André, E., Orlando, R., Dovesi, R., "The Raman spectrum of $CaCO_3$ polymorphs calcite and aragonite: A combined experimental and computational study", ***The Journal of Chemical Physics***, Vol. 140, No. 16, (2014), 164509. https://doi.org/10.1063/1.4871900
29. Gunasekaran, S., Anbalagan, G., Pandi, S., "Raman and infrared spectra of carbonates of calcite structure", ***Journal of Raman Spectroscopy***, Vol. 37, No. 9, (2006), 892-899. https://doi.org/10.1002/jrs.1518
30. Herrera, L. K., Videla, H. A., "Surface analysis and materials characterization for the study of bio deterioration and weathering

effects on cultural property", ***International Biodeterioration & Biodegradation***, Vol. 63, No. 7, (2009), 813-822. https://doi.org/10.1016/j.ibiod.2009.05.002
31. Ospitali, F., Bersani, D., Di Lonardo, G., Lottici, P. P., "'Green earths': vibrational and elemental characterization of glauconites, celadonites and historical pigments", ***Journal of Raman Spectroscopy***, Vol. 39, No. 8, (2008), 1066-1073. https://doi.org/10.1002/jrs.1983
32. Huang, E., Chen, C. H., Huang, T., Lin, E. H., Xu, J. A., "Raman spectroscopic characteristics of Mg-Fe-Ca pyroxenes", ***American Mineralogist***, Vol. 85, No. 3-4, (2000), 473-479. https://doi.org/10.2138/am-2000-0408
33. Bishop, J. L., Ethbrampe, E. B., Bish, D. L., Abidin, Z. L., Baker, L. L., Matsue, N., Henmi, T., "Spectral and Hydration Properties of Allophane and Imogolite", ***Clays and Clay Minerals***, Vol. 61, No. 1, (2013), 57-74. https://doi.org/10.1346/CCMN.2013.0610105
34. Friedlander, L. R., Glotch, T. D., Bish, D. L., Dyar, M. D., Sharp, T. G., Sklute, E. C., Michalski, J. R., "Structural and spectroscopic changes to natural non tronite induced by experimental impacts between 10 and 40GPa", ***Journal of Geophysical Research: Planets***, Vol. 120, No. 5, (2015), 888-912. https://doi.org/10.1002/2014JE004638
35. Derbyshire, A., Withnall, R., "Pigment analysis of portrait miniatures using Raman microscopy", ***Journal of Raman Spectroscopy***, Vol. 30, No. 3, (1999), 185-188. https://doi.org/10.1002/(SICI)1097-4555(199903)30:3<185::AID-JRS357>3.0.CO;2-U
36. Bates, J. B., "Raman Spectra of α and β Cristobalite", ***The Journal of Chemical Physics***, Vol. 57, No. 9, (1972), 4042-4047. https://doi.org/10.1063/1.1678878
37. Kingma, K. J., Heymley, R. J., "Raman spectroscopic study of microcrystalline silica", ***American Mineralogist***, Vol. 79, No. 3-4, (1994), 269-273. https://eurekamag.com/research/019/844/019844826.php
38. Liang, Y., Miranda, C. R., Scandolo, S., "Infrared and Raman spectra of silica polymorphs from an ab initio parametrized polarizable force field", ***The Journal of Chemical Physics***, Vol. 125, No. 19, (2006), 194524. https://doi.org/10.1063/1.2390709
39. San Andrés, M., De la Roja, J. M., Baonza, V. G., Sancho, N., "Verdigris pigment: a mixture of compounds. Input from Raman spectroscopy", ***Journal of Raman Spectroscopy***, Vol. 41, No. 11, (2010), 1468-1476. https://doi.org/10.1002/jrs.2786
40. Shenderova, O. A., Gruen, D. M., ***Ultrananocrystalline Diamond: Synthesis, Properties, and Applications***, 2nd Ed., Norwich, New York, William Andrew, (2012). https://doi.org/10.1016/C2010-0-67069-6
41. Xu, W., Sun, Y., Dong, X., Li, S., Wang, H., Xue, J., Zheng, X., "Local order and vibrational coupling of the C=O Stretching Mode of γ-Caprolactone in liquid binary mixtures", ***Scientific Reports***, Vol. 7, No. 1, (2017), 12182. https://doi.org/10.1038/s41598-017-12030-1
42. Sergeeva, A. V., Zhitova, E. S., Nuzhdaev, A. A., Zolotarev, A. A., Bocharov, V. N., Ismagilova, R. M., "Infrared and Raman Spectroscopy of Ammoniovoltaite, $(NH_4)_2Fe^{2+}_5Fe^{3+}_3Al(SO_4)_{12}(H_2O)_{18}$", ***Minerals***, Vol. 10, No. 9, (2020), 781. https://doi.org/10.3390/min10090781
43. Kolesov, B., "Raman investigation of H_2O molecule and hydroxyl groups in the channels of hemimorphite", ***American Mineralogist***, Vol. 91, No. 8-9, (2006), 1355-1362. https://doi.org/10.2138/am.2006.2179
44. Keppler, H., "Crystal field spectra and geochemistry of transition metal ion in silicate melts and glasses", ***American Mineralogist***, Vol. 77, No. 1-2, (1992), 62-75. http://www.minsocam.org/ammin/AM77/AM77_62.pdf

Advanced Ceramics Progress: Vol. 8, No. 1, (Winter 2022) 36-43

Materials and Energy Research Center
MERC

Contents lists available at ACERP

Advanced Ceramics Progress

Journal Homepage: www.acerp.ir

Original Research Article

Effect of Temperature on the Low-Pressure Chemical Vapor Deposition of Graphene

Aziz Noori [a], Mohammad Javad Eshraghi [b], Asieh Sadat Kazemi [c, *]

[a] *MSc Student, Department of Physics, Iran University of Science and Technology (IUST), Tehran, Tehran, Iran*
[b] *Associate Professor, Department of Semiconductors, Materials and Energy Research Center (MERC), Meshkindasht, Alborz, Iran*
[c] *Assistant Professor, Department of Physics, Iran University of Science and Technology (IUST), Tehran, Tehran, Iran*

* Corresponding Author Email: asiehsadat_kazemi@iust.ac.ir (A. S. Kazemi)

URL: https://www.acerp.ir/article_153519.html

ARTICLE INFO

Article History:

Received 30 May 2022
Received in revised form 28 June 2022
Accepted 17 July 2022

Keywords:

Graphene
Chemical Vapor Deposition
Growth Temperature
Raman Spectroscopy
Atomic Force Microscopy

ABSTRACT

Large area fabrication of graphene, as a leading two-dimensional material as well as an allotrope of carbon, is a challenging requirement prior to its preparation for applications. Chemical Vapor Deposition (CVD) is one of the most effective and promising methods for high-scale and high-quality synthesis of graphene. In this study, graphene layers were grown on copper (Cu) sheets using low-pressure CVD technique at 930 °C, 870 °C, and 760 °C. Raman spectroscopy, Field Emission Scanning Electron Microscopy (FESEM), Optical Microscopy (OM) and Atomic Force Microscopy (AFM) were employed in this study to investigate the effect of the process temperature on the structural properties, morphology, grain boundaries, continuity, purity, and number of layers. The results from analyses revealed that at higher temperatures, the continuity and quality of the layers and number of grain boundaries were higher and lower, respectively. In contrast, at lower temperatures, the nucleation and discontinuity of the deposited layers were relatively high. The surface roughness of the graphene sheets increased with a decrease in temperature.

https://doi.org/10.30501/acp.2022.343786.1090

1. INTRODUCTION

Two-Dimensional (2D) materials have attracted considerable attention due to their properties that are superior to those of their 3D counterparts. These materials are regarded as the potential candidates for replacement of conventional resources in many fields of technology. Further, they have introduced new applications in some areas, but a complete replacement of these materials faces several challenges such as ensuring the mass production, high purity, and efficient utilization [1,2].

A leading member of the 2D family [2,3], graphene, is a unique material due to its excellent properties such as high electrical and thermal conductivity [5], high density [6], high optical conductivity [7], and excellent mechanical properties [8,9]. A layer of carbon atoms in graphene is packed in a honeycomb network with sp^2 hybridized orbitals and a bond length of 0.142 nm [8,9].

Please cite this article as: Noori, A., Eshraghi, M. J., Kazemi, A., "Effect of Temperature on the Low-Pressure Chemical Vapor Deposition of Graphene", ***Advanced Ceramics Progress***, Vol. 8, No. 1, (2022), 36-45. https://doi.org/10.30501/acp.2022.343786.1090

Graphene can be fabricated using different methods such as mechanical exfoliation [11], electrochemical exfoliation [12], liquid-phase exfoliation [13], peer growth on silicon carbide (SiC) [14], unzipping of carbon nanotubes [15], and graphene oxide reduction [16]. Exfoliation methods used for graphene production produce very small flakes with random thickness values while reduction methods would form several layers. These are not continuous and still have residues left behind from the synthesis method. However, large area graphene with controlled number of layers can be obtained by Chemical Vapor Deposition (CVD) [17]. In CVD, the required carbon atoms are separated from the precursor gas under high temperature and low pressure and then bonded with a flat metal sheet [18]. CVD is an extensive bottom-up method for synthesizing multilayer and monolayer graphene films. This approach outperforms other methods in terms of its ease of installation in laboratories, successful long-term use in industrial environments, high potential for large-scale production, and beneficial environmental and economic factors [19]. The process and types of different chemical reactions that occur in a CVD chamber are controlled by many complex factors including system regulation, furnace configuration, gas bare materials, gas ratios, chamber pressure, gas flow, reaction temperature, and growth time [20,21].

There are several types of CVD methods available today that can be used to synthesize graphene-based materials. Following its first isolation via micromechanical exfoliation in 2004, larger area graphene was successfully obtained using Low-Pressure CVD (LPCVD) [22]. Historically, CVD growth of the crystalline graphite on Ni was first reported in 1966 [23] and later, graphite was deposited on Pt using CVD [24]. Ever since, LPCVD has been used to grow graphene with the advantage of obtaining more uniform sheets with few layers [25].

Depending on the growth conditions, different CVD methods can be classified into several main types based on temperature, pressure, precursor nature, gas flow, wall/bed temperature, deposition time, and activation energy [26,27]. Among the mentioned factors, temperature plays a vital role in CVD growth of graphene since it provides the required activation energy to decompose the carbon source and prepare the substrate surface. For instance, the required temperature for methane decomposition is about 1000 °C [28]; therefore, graphene cannot be formed below this temperature. However, graphene can be synthesized at lower temperatures using other materials in the growth process [29-31]. Under the same laboratory conditions, temperature variations cause changes in the growth quality, number of layers, and continuity of the grown layers. Chaitoglou et al. [32] explored the effect of temperature on the CVD graphene growth on Cu. In their research, the temperature varied from 970 °C to 1070 °C, and no roughness study was conducted. In another study, the optical transmittance spectra were used to determine the number of the graphene layers grown at 400-1000 °C via CVD. Lower temperatures resulted in lower quality graphene films [33]. Zheng et al. [34] reported catalytic metal engineering to reduce the growth temperature to 700 °C using Cu-C alloy on SiO_2/Si substrate and CVD growth of continuous single-layer graphene on Cu by sequential melting-resolidification-recrystallization in the temperature range of 980-1060 °C. The latter required a complicated and costly process, yielding the results comparable to those of the usual CVD methods.

Here, graphene was grown by LPCVD method in a homemade LPCVD setup at temperatures around and well below the usual temperature (1000 °C) required for decomposition of the carbon precursor. Cu substrate was used as the catalyst and methane (CH_4), as a carbon precursor. The dependency of temperature on the growth quality, continuity, and number of graphene layers was investigated at 930, 870, and 760 °C using different surface analysis methods. While Raman spectra and FESEM results confirmed the formation of graphene sheets, surface roughness parameters obtained from atomic force microscopy images yielded novel results regarding the as-grown graphene sheets on Cu. Many large area graphene sheets are characterized by high roughness values that limit their applications, hence roughness control based on growth parameters is very beneficial.

2. MATERIALS AND METHODS

In this study, 99.99 % H_2 and 99.9 % CH_4 were used as the assistant and carbon source gases, respectively, due to the following reasons: a) hydrogen is widely used in the annealing phases to remove the oxide layer on the metal surfaces, and b) it plays a key role in absorbing H_2 from CH_4 [17]. Methane has a single bond and lower bond energy than a carbon precursor with a double and triple bond whereas acetylene with its triple bond character can react with unbonded electrons of other elements in the environment. Therefore, unwanted corrosive and toxic compounds may be produced from these reactions [35]. In this study, Cu foils with a thickness of 30 µm were used as the substrate, and the thermal decomposition of methane was reduced by 930, 870, and 760 °C to control the growth procedure in the presence of Cu as the catalyst substrate. Here, Cu was selected for the growth process due to the lower solubility of C atoms in Cu. It is known that C solubility in Ni is higher. Furthermore, thin film Cu catalyst sheets are readily available and inexpensive [36].

The foils were cut into sheets of 20×50 mm^2 in size. Cu sheets were initially immersed in acetic acid (99.9 %, Merck) for 10 min to remove surface oxides and then washed in ethanol for five min in an ultrasonic bath to

remove impurities and contaminations. Cu sheets were then air-dried for two minutes. Finally, they were transferred via an alumina boat into a quartz chamber in the furnace.

Figure 1 shows the schematics of the home-made LPCVD system which is used for growing graphene on the Cu sheets. As indicated in this figure, this setup consists of a tubular furnace, Mass Flow Controllers (MFC) for controlling gas flows, a vacuum gauge for controlling the deposition pressure, and a rotary vacuum pump with a volume capacity of 80 m^3/h for evacuating the by-products.

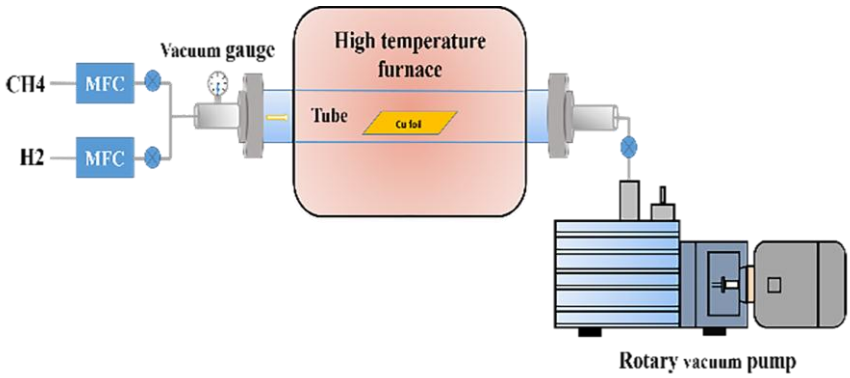

Figure 1. Schematics of the LPCVD setup for graphene growth

CH_4 and H_2 flow rates were set at 35 and 7 (standard cubic centimeter/minute) sccm, respectively, to maintain the flow ratio of 5:1. The initial pressure of the chamber was set at 0.35 mbar. At 200 °C, H_2 was allowed into the furnace to prevent Cu oxidation. CH_4 entered the chamber at the desired coating temperature. At the end of deposition, CH_4 flow was stopped, and the furnace cool-down stage was performed in the H_2 atmosphere. Finally, the samples were extracted from the furnace at the ambient temperature. Of note, the samples grown at 930, 870, and 760 °C are named S1-S3, respectively, hereafter. In addition to the fabrication of Samples S1-S3 at different temperatures, and for a comparative study, a Cu sheet was annealed at 930 °C in the presence of H_2 and in the absence of CH_4. This sample is called bare-Cu hereafter. The time required for the growth process for all samples was fixed at 30 min. The specific values of the growth temperatures were obtained from experimental trials.

Optical microscopy (Nano Raga), Field Emission Scanning Electron Microscopy (FESEM-TESCAN Mira3 operated at 15 kV), and Atomic Force Microscopy (AFM-Advanced Ara Pajauhesh) were used to characterize the structural and surface properties of the obtained graphene sheets. Raman spectroscopy (Teksan 530-700 nm wavelength) was also used to ensure the formation of graphene.

3. RESULTS AND DISCUSSION

Carbon atoms settle together on a Cu sheet during the CVD growth of graphene, as indicated in Figure 2.

During the growth mechanism, Cu, as the metal catalyst, determined graphene's precipitation rate and was exploited to reduce the energy barrier of the reactions. It should be noted that C atoms are slowly adsorbed on the Cu surface. With CH_4 entrance in the furnace and the increase of the temperature to values required for the decomposition of hydrocarbon bonds, and C atoms precipitate as a solid on the Cu surface while H atoms bond together and leave the chamber as gas. C atoms left behind on the Cu surface start to form in-plane σ bonds (i.e., covalent bonds where each C atom relates to three other C atoms) and cover the whole Cu sheet continuously in a single layer [37]. If the growth time is long enough, a second or even a third layer may form. In this situation, van der Waals force of attraction is responsible to hold the layers together. Usually, a large number of C atoms, more than what is needed to form a single layer, gather near the grain boundaries; therefore, the quality of the graphene reduces in these areas [38].

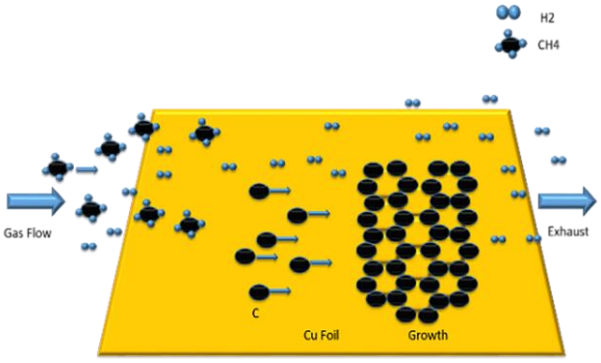

Figure 2. Schematics of LPCVD graphene growth mechanism on a Cu sheet

According to the FESEM images of the grown graphene samples shown in Figure 3 (top row), dark regions correspond to higher number of layers while bright regions correspond to lower number of layers. At higher growth temperatures, Cu surface becomes smoother in the lower number of grain boundaries. Higher temperatures are close to the melting point of Cu, thus providing much better growth conditions. At lower temperatures, higher surface roughness and larger number of grain boundaries would result in more nucleation and slow down the growth procedure [39]. According to the FESEM images, graphene domains are not continuous, hence more time is required to gain a continuous region of graphene. Of note, the number of graphene layers increases over time. In addition, increasing the growth time diminishes the growth process and creates anisotropic layers. These layers damage the existing layers. Here, the hydrogen flow, pressure, and evacuation rate (L/h) were adequate. Hydrogen controls the shape and size of the domains by breaking the hydrocarbon bonds. The pressure mainly affects the durability time of carbon atoms on the Cu surface. One of the reasons we worked at lower pressures was to prevent the saturation of carbon atoms and their nucleation on the Cu surface. By controlling these conditions, monolayer graphene with continuous layers can be achieved [40]. Optical images in Figure 3 (bottom row) show larger carbon crystallites in S1 with respect to S2 and S3. The grain boundaries in S2 and S3 are much more evident than in S1.

Raman spectra were taken from four random points on the graphene grown on the Cu sheets. Figure 4 shows the average the mentioned spectra for samples S1-S3. The Raman spectrum of the perfect single-layer graphene includes sp^2 hybridization with two peaks at 1580 cm^{-1} and 2700 cm^{-1} that are attributed to G and 2D bands, respectively [41].

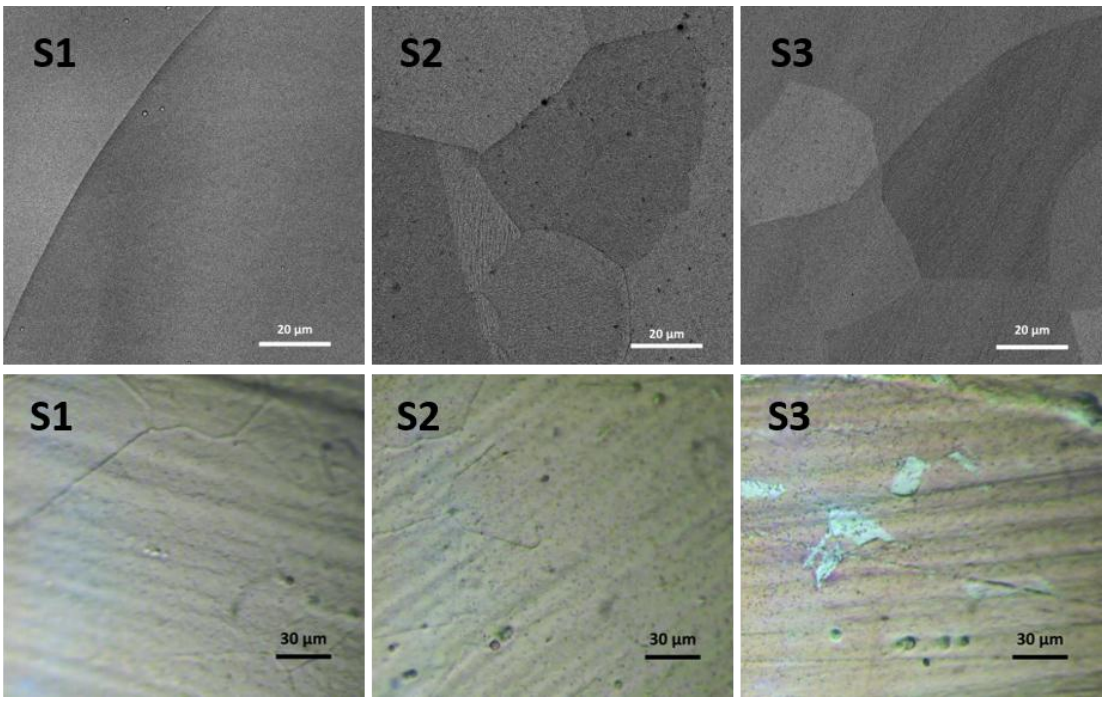

Figure 3. (Top row) FESEM images and (bottom row) optical images of S1-930 °C, S2-870 °C, and S3-760 °C, respectively

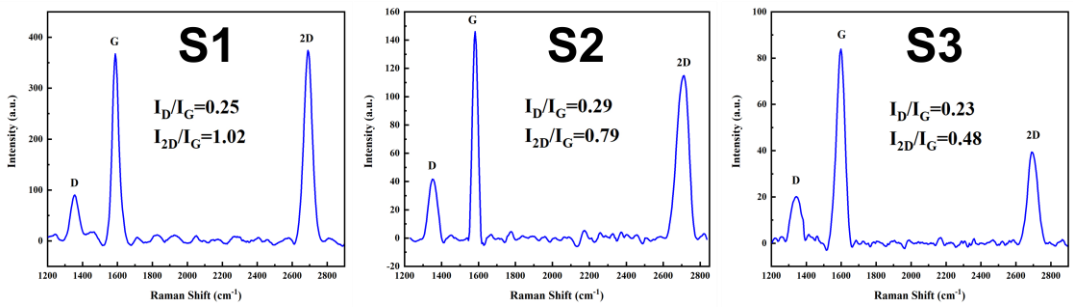

Figure 4. (Top row) FESEM images and (bottom row) optical images of S1-930 °C, S2-870 °C, and S3-760 °C, respectively

D band is observed when sufficient number of structural defects are reached for the graphene that leads to the intensification of the D band [42]. The ratio of I_{2D}/I_G=1.02, in sample S1 is larger than those of other samples due to its higher growth temperature which in turn leads to faster breaking of the bonds between H and C atoms and smoothing of the roughness on the substrate surface [32]. A comparison of the FESEM images of S1 with those of other samples shows that S1 consists of fewer layers. According to the averaged Raman spectrum analysis of S2, I_{2D}/I_G=0.79, which is less than that of S1. This result is consistent with the thickness and number of grain boundaries of the two samples shown in the FESEM images. According to the Raman spectrum of S3, I_{2D}/I_G = 0.48 which is lower than that of other samples. FESEM image of sample S3 showed more discontinuities and higher number of grain boundaries. The results obtained here are consistent with those acquired in previous studies [43]. Accordingly, at higher growth temperatures, I_{2D}/I_G ratio will increase which is indicative of a larger area of monolayer graphene. At higher growth temperatures, lower activation energy is required to break C-H bonds, thus resulting in the reduction of substrate roughness and the reduction of substrate grain boundaries [44]. S. Shukrullah et al. [45] investigated the effect of temperature on the activation energy. The coatings created therein were treated by CVD. The properties of the obtained coatings showed that the activation energy is inversely related to growth temperature, calculated by the following equation, known as the Arrhenius relation:

$$K = Ae^{-\frac{E_a}{RT}} \quad (1)$$

where K is the growth rate coefficient, E_a the activation energy, A the Arrhenius constant, R the global gas constant, and T the process temperature.

One of the important and comprehensive methods for identifying the structure of graphene and its morphological characteristics is AFM. The continuity of the grown layer and presence of impurities and surface roughness were confirmed through AFM and relevant analyses [46].

Roughness characterization is a very important tool before and after graphene transfer on the desired substrate. Many large-area graphene sheets suffer high roughness values that undermine their applications in electronic devices or even the separation membrane techniques. Therefore, controlling roughness via growth parameters is highly advantageous [47].

For a comparative study, the surface of the bare Cu sheet annealed at 930 °C was characterized in contact mode along with S1-S3 in tapping mode, all equipped with silicon nitride cantilevers. Figure 5 demonstrates a 3D view of the bare Cu and three graphene samples (S1-S3). As observed, the surface roughness in bare Cu, which was not exposed to methane, is higher than in the graphene-grown samples.

However, more quantitatively from roughness parameters extracted from topography images with SPIP software (Table 1), bare Cu is less rough than S3 probably due to the much lower annealing temperature Sample S3 went through than bare Cu did. Note that C crystallite structures on the surfaces of S1-S3 also increase the value of the roughness parameters while the bare Cu surface with no crystallites has relatively higher roughness values. In samples S1-S3, the average surface roughness or **Sa** increases from S1 to S3. **Sa**, is one of the most commonly used roughness parameters [48], and it is the average of the deviations of the mean plane. Another roughness parameter derived from the AFM topography images is **Sq** which is the standard deviation of the height distribution, also known as RMS roughness.

TABLE 1. Roughness parameters of bare Cu and graphene covered S1-S3, data extracted from AFM topographic images

parameters	Bare Cu	S1	S2	S3	Unit
Sa	20.4	6.9	16.9	21.3	nm
Sq	26.0	9.9	21.5	31.3	nm

Changes in this quantity are similar to changes in **Sa** in S1-S3. It is clear that increasing the growth temperature contributes to reduction in the deep structural roughness in the Cu sheet. Figure 6 shows 2D topographic and phase images of the samples. No trace of graphene is detected in the topographic or phase images of the bare Cu sample. According to the topographic images of samples S1-S3, some elements are observed on these surfaces, confirming the presence of a material different from the Cu sheet. Further, the surface structure in S1-S3 is significantly changed compared to that in the bare Cu which can be confirmed in the relevant phase images. In addition to the graphene grains, thicker carbon hexagonal structures can be seen on these surfaces, which is consistent with the findings of FESEM.

In addition, the number of impurities on these surfaces and thickness of the carbon crystallites (as bright spots) are in good agreement with the Raman spectroscopic findings for each sample. According to the phase images, the formation of grain boundaries in the grown graphene layers is evident. In S3, carbon crystallites as islands of thicker graphene (consisting of more layers) are obviously seen.

Figure 6 indicates the surface morphology of the samples, and Figure 4 shows the ratio of $I_{2D}/I_{G,}$ indicating the higher graphene coverage and more uniformity in samples S1-S3 followed by increasing growth temperature. This result is in agreement with the AFM results. In addition, based on the results from the topographic AFM images and Table 1, it can be concluded that the surface roughness decreases with an increase in the temperature. According to these results, there is a direct impact on the growth quality of graphene

mainly due to the sufficient energy provided to break the bond between hydrogen and carbon. At higher temperatures, this energy is given more to the carbon source gas that improves the growth coating quality and uniformity. In reality, several problems may arise such as limitation of the use of materials with lower melting points and high cost of experiments at high temperatures. Given these problems, another mechanism should be taken into account to produce the energy needed for breaking the bond between hydrogen and carbon. Consequently, high temperatures are not required for CVD graphene. This can be considered as the future research focus in this field.

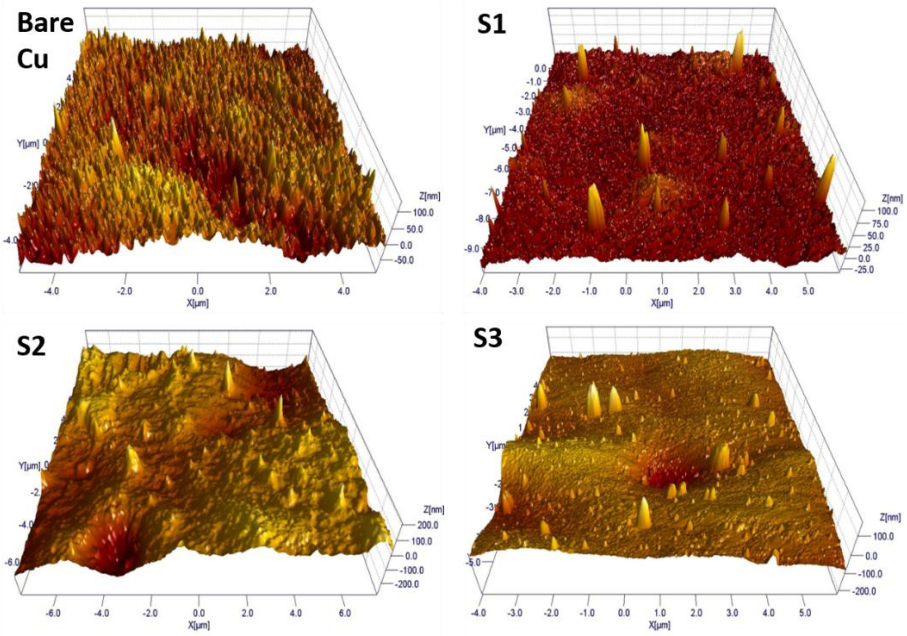

Figure 5. 3D images of the bare Cu and graphene grown in S1-S3. The size of all images is 10×10 μm^2

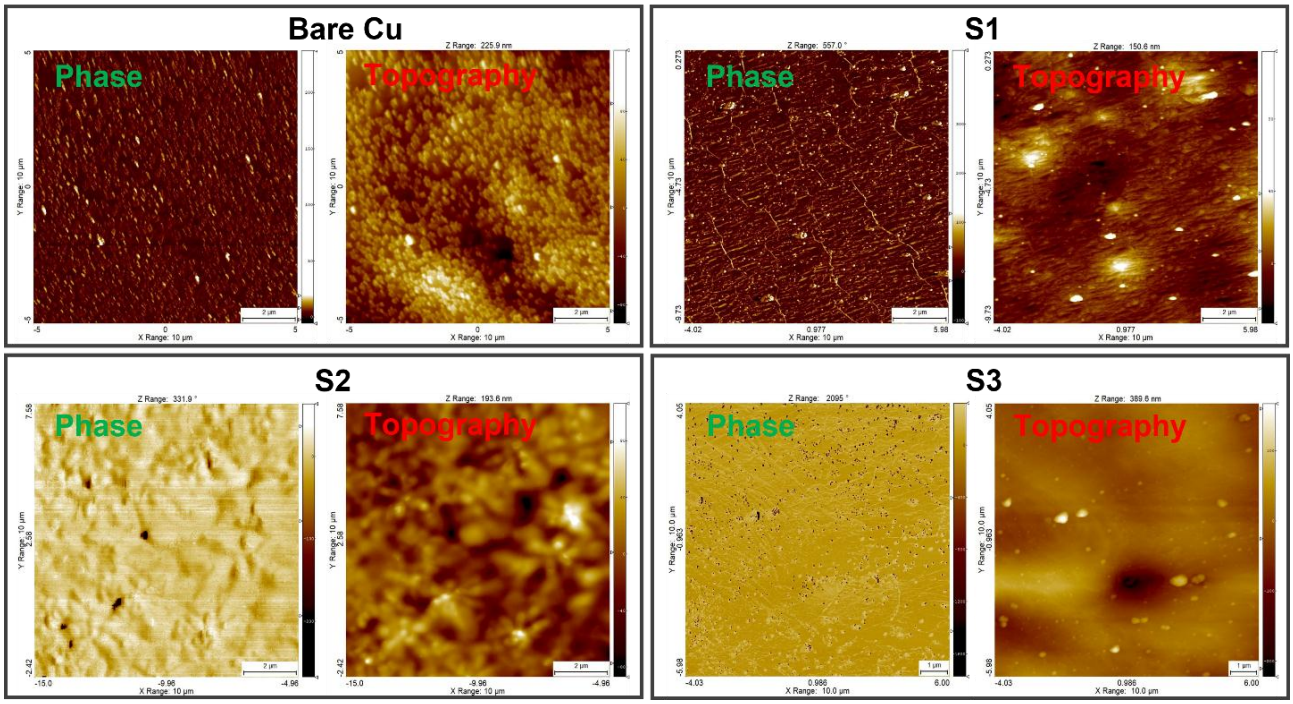

Figure 6. 2D topographic and the corresponding phase images of bare Cu and graphene covered S1-S3. All images are 10×10 μm^2

4. CONCLUSION

In this study, graphene was synthesized based on the LPCVD method using methane and hydrogen gas compounds on Cu catalysts at temperatures below 1000 °C. To this end, the conditions were optimized by keeping other growth parameters constant. According to the optical and FESEM analyses, the sample grown at 930 °C were characterized by better continuity and larger surface area than other samples. Based on the Raman spectroscopy analyses, it can be concluded that the ratio of I_{2D}/I_G at higher temperatures was higher than that at lower temperatures which, in this case, was indicative of the lower number of layers. The surface roughness from the AFM topographic images of the sample grown at 930 °C (6.935 nm) was less than that of the other two samples at 870 °C (16.953 nm) and 760 °C (21.328 nm). The measured roughness of the bare Cu (20.485 nm) was higher than S1 and S2 samples yet slightly lower than S3 sample. The obtained results confirmed the higher possibility of obtaining smoother graphene with better quality at higher temperatures.

ACKNOWLEDGEMENTS

The authors would like to thank National Elites Foundation No. 15/10002 in Iran for the financial support they provided towards this work.

REFERENCES

1. Wang, X., Song, Z., Wen, W., Liu, H., Wu, J., Dang, C., Hossain, M., Iqbal, M. A., Xie, L., "Potential 2D materials with phase transitions: structure, synthesis, and device applications", ***Advanced Materials***, Vol. 31, No. 45, (2019), 1804682. https://doi.org/10.1002/adma.201804682
2. Saraei, A., Eshraghi, M., Massoudi, A., "Investigation of resistive switching in anodized titanium dioxide thin films", ***Advanced Ceramics Progress***, Vol. 2, No. 3, (2016), 34-37. https://doi.org/10.30501/acp.2016.70029
3. Trivedi, S., Lobo, K., Matte, H. R., "Synthesis, properties, and applications of graphene", ***Fundamentals and Sensing Applications of 2D Materials***, (2019), 25-90. https://doi.org/10.1016/B978-0-08-102577-2.00003-8
4. Shi, G., Araby, S., Gibson, C. T., Meng, Q., Zhu, S., Ma, J., "Graphene platelets and their polymer composites: fabrication, structure, properties, and applications", ***Advanced Functional Materials***, Vol. 28, No. 19, (2018), 1706705. https://doi.org/10.1002/adfm.201706705
5. Malekpour, H., Chang, K. H., Chen, J. C., Lu, C. Y., Nika, D. L., Novoselov, K. S., Balandin, A. A., "Thermal conductivity of graphene laminate", ***Nano Letters***, Vol. 14, No. 9, (2014), 5155-5161. https://doi.org/10.1021/nl501996v
6. Li, W., Gao, S., Wu, L., Qiu, S., Guo, Y., Geng, X., Chen, M., Liao, S., Zhu, C., Gong, Y., Long, M., Xu, J., Wei, X., Sun, M., Liu, L., "High-density three-dimension graphene macroscopic objects for high-capacity removal of heavy metal ions", ***Scientific Reports***, Vol. 3, No. 1, (2013), 1-6. https://doi.org/10.1038/srep02125
7. Mak, K. F., Sfeir, M. Y., Wu, Y., Lui, C. H., Misewich, J. A., Heinz, T. F., "Measurement of the optical conductivity of graphene", ***Physical Review Letters***, Vol. 101, No. 19, (2008), 196405. https://doi.org/10.1103/PhysRevLett.101.196405
8. Papageorgiou, D. G., Kinloch, I. A., Young, R. J., "Mechanical properties of graphene and graphene-based nanocomposites", ***Progress in Materials Science***, Vol. 90, (2017), 75-127. https://doi.org/10.1016/j.pmatsci.2017.07.004
9. Samiee, M., Seyedraoufi, Z. S., Shajari, Y., "Dry and wet wear characteristic of TiO_2 thin film prepared by magnetic sputtering in ringer solution", ***Advanced Ceramics Progress***, Vol. 5, No. 4, (2019), 30-37. https://doi.org/10.30501/acp.2019.103893
10. Qiu, Y., Zhang, Y., Ademiloye, A. S., Wu, Z., "Molecular dynamics simulations of single-layer and rotated double-layer graphene sheets under a high velocity impact by fullerene", ***Computational Materials Science***, Vol. 182, (2020), 109798. https://doi.org/10.1016/j.commatsci.2020.109798
11. Yi, M., Shen, Z., "A review on mechanical exfoliation for the scalable production of graphene", ***Journal of Materials Chemistry A***, Vol. 3, No. 22, (2015), 11700-11715. https://doi.org/10.1039/C5TA00252D
12. Yu, P., Lowe, S. E., Simon, G. P., Zhong, Y. L., "Electrochemical exfoliation of graphite and production of functional graphene", ***Current Opinion in Colloid & Interface Science***, Vol. 20, No. 5-6, (2015), 329-338. https://doi.org/10.1016/j.cocis.2015.10.007
13. Xu, Y., Cao, H., Xue, Y., Li, B., Cai, W., "Liquid-phase exfoliation of graphene: an overview on exfoliation media, techniques, and challenges", ***Nanomaterials***, Vol. 8, No. 11, (2018), 942. https://doi.org/10.3390/nano8110942
14. Yazdi, G. R., Iakimov, T., Yakimova, R., "Epitaxial graphene on SiC: a review of growth and characterization", ***Crystals***, Vol. 6, No. 5, (2016), 53. https://doi.org/10.3390/cryst6050053
15. Kumar, A., Sharma, K., Dixit, A. R., "Carbon nanotube-and graphene-reinforced multiphase polymeric composites: review on their properties and applications", ***Journal of Materials Science***, Vol. 55, No. 7, (2020), 2682-2724. https://doi.org/10.1007/s10853-019-04196-y
16. Guex, L. G., Sacchi, B., Peuvot, K. F., Andersson, R. L., Pourrahimi, A. M., Ström, V., Farris, S., Olsson, R. T., "Experimental review: chemical reduction of graphene oxide (GO) to reduced graphene oxide (rGO) by aqueous chemistry", ***Nanoscale***, Vol. 9, No. 27, (2017), 9562-9571. https://doi.org/10.1039/C7NR02943H
17. Muñoz, R., Gómez-Aleixandre, C., "Review of CVD synthesis of graphene", ***Chemical Vapor Deposition***, Vol. 19, No. 10-11-12, (2013), 297-322. https://doi.org/10.1002/cvde.201300051
18. Bhuyan, M., Alam, S., Uddin, M., Islam, M., Bipasha, F. A., Hossain, S. S., "Synthesis of graphene", ***International Nano Letters***, Vol. 6, No. 2, (2016), 65-83. https://doi.org/10.1007/s40089-015-0176-1
19. Yang, X., Zhang, G., Prakash, J., Chen, Z., Gauthier, M., Sun, S., "Chemical vapour deposition of graphene: Layer control, the transfer process, characterisation, and related applications", ***International Reviews in Physical Chemistry***, Vol. 38, No. 2, (2019), 149-199. https://doi.org/10.1080/0144235X.2019.1634319
20. Venkatesan, S., Visvalingam, B., Mannathusamy, G., Viswanathan, V., Rao, A. G., "Effect of chemical vapor deposition parameters on the diameter of multi-walled carbon nanotubes", ***International Nano Letters***, Vol. 8, No. 4, (2018), 297-308. https://doi.org/10.1007/s40089-018-0252-4
21. Fallahazad, P., Naderi, N., Eshraghi, M. J., Massoudi, A., "Optimization of Chemical Texturing of Silicon Wafers Using Different Concentrations of Sodium Hydroxide in Etching Solution", ***Advanced Ceramics Progress***, Vol. 3, No. 3, (2017), 16-18. https://doi.org/10.30501/acp.2017.90753
22. Coraux, J., N 'Diaye, A. T., Busse, C., Michely, T., "Structural coherency of graphene on Ir (111)", ***Nano Letters***, Vol. 8, No. 2,

(2008), 565-570. https://doi.org/10.1021/nl0728874

23. Karu, A. E., Beer, M., "Pyrolytic formation of highly crystalline graphite films", ***Journal of Applied Physics***, Vol. 37, No. 5, (1966), 2179-2181. https://doi.org/10.1063/1.1708759
24. Land, T.A., Michely, T., Behm, R. J., Hemminger, J. C., Comsa, G., "STM investigation of single layer graphite structures produced on Pt (111) by hydrocarbon decomposition", ***Surface science***, Vol. 264, No. 3, (1992), 261-270. https://doi.org/10.1016/0039-6028(92)90183-7
25. Ullah, Z., Riaz, S., Li, Q., Atiq, S., Saleem, M., Azhar, M., Naseem, S., Liu, L., "A comparative study of graphene growth by APCVD, LPCVD and PECVD", ***Materials Research Express***, Vol. 5, No. 3, (2018), 035606. https://doi.org/10.1088/2053-1591/aab7b4
26. Ferrari, A. C., Bonaccorso, F., Fal'Ko, V., Novoselov, K. S., Roche, S., Bøggild, P., Borini, S., Koppens, F. H., Palermo, V., Pugno, N., Garrido, J. A., "Science and technology roadmap for graphene, related two-dimensional crystals, and hybrid systems", ***Nanoscale***, Vol. 7, No. 11, (2015), 4598-4810. https://doi.org/10.1039/C4NR01600A
27. Hamidi, S., Rahimipour, M. R., Eshraghi, M. J., Esfahani, H., "Optimization of Heat Treatment Cycles in Sub-atmospheric LiF-NaF-KF Based Fluoride Ion Cleaning for Removing Oxide Layers in Cracks of IN738-LC", ***Advanced Ceramics Progress***, Vol. 7, No. 1, (2021), 18-24. https://doi.org/10.30501/acp.2021.251522.1046
28. Taira, T., Obata, S., Saiki, K., "Nucleation site in CVD graphene growth investigated by radiation-mode optical microscopy", ***Applied Physics Express***, Vol. 10, No. 5, (2017), 055502. https://doi.org/10.7567/APEX.10.055502
29. Yao, Y., Li, Z., Lin, Z., Moon, K. S., Agar, J., Wong, C., "Controlled growth of multilayer, few-layer, and single-layer graphene on metal substrates", ***The Journal of Physical Chemistry C***, Vol. 115, No. 13, (2011), 5232-5238. https://doi.org/10.1021/jp109002p
30. Guermoune, A., Chari, T., Popescu, F., Sabri, S. S., Guillemette, J., Skulason, H. S., Szkopek, T., Siaj, M., "Chemical vapor deposition synthesis of graphene on copper with methanol, ethanol, and propanol precursors", ***Carbon***, Vol. 49, No. 13, (2011), 4204-4210. https://doi.org/10.1016/j.carbon.2011.05.054
31. Zhang, B., Lee, W. H., Piner, R., Kholmanov, I., Wu, Y., Li, H., Ji, H., Ruoff, R. S., "Low-temperature chemical vapor deposition growth of graphene from toluene on electropolished copper foils", ***ACS Nano***, Vol. 6, No. 3, (2012), 2471-2476. https://doi.org/10.1021/nn204827h
32. Chaitoglou, S., Bertran, E., "Effect of temperature on graphene grown by chemical vapor deposition", ***Journal of Materials Science***, Vol. 52, No. 13, (2017), 8348-8356. https://doi.org/10.1007/s10853-017-1054-1
33. Li, Z., Wu, P., Wang, C., Fan, X., Zhang, W., Zhai, X., Zeng, C., Li, Z., Yang, J., Hou, J., "Low-temperature growth of graphene by chemical vapor deposition using solid and liquid carbon sources", ***ACS Nano***, Vol. 5, No. 4, (2011), 3385-3390. https://doi.org/10.1021/nn200854p
34. Zheng, L., Cheng, X., Ye, P., Shen, L., Wang, Q., Zhang, D., Gu, Z., Zhou, W., Wu, D., Yu, Y., "Decreasing graphene synthesis temperature by catalytic metal engineering and thermal processing", ***RSC Advances***, Vol. 8, No. 3, (2018), 1477-1480. https://doi.org/10.1039/C7RA11654C
35. Mahyuddina, A., Ismaila, A. K., Firdaus, M., Omara, A. H. K., "Recent Progress on CVD Growth of Graphene from a Liquid Carbon Precursor", ***Malaysian Journal of Fundamental and Applied Sciences***, Vol. 17, No. 3, (2021), 262-273. https://doi.org/10.11113/mjfas.v17n3.2080
36. Huang, M., Ruoff, R. S., "Growth of single-layer and multilayer graphene on Cu/Ni alloy substrates", ***Accounts of Chemical Research***, Vol. 53, No. 4, (2020), 800-811. https://doi.org/10.1021/acs.accounts.9b00643
37. Seah, C. M., Chai, S. P., Mohamed, A. R., "Mechanisms of graphene growth by chemical vapour deposition on transition metals", ***Carbon***, Vol. 70, (2014), 1-21. https://doi.org/10.1016/j.carbon.2013.12.073
38. Vlassiouk, I., Smirnov, S., Regmi, M., Surwade, S. P., Srivastava, N., Feenstra, R., Eres, G., Parish, C., Lavrik, N., Datskos, P., Dai, S., "Graphene nucleation density on copper: fundamental role of background pressure", ***The Journal of Physical Chemistry C***, Vol. 117, No. 37, (2013), 18919-18926. https://doi.org/10.1021/jp4047648
39. Xing, S., Wu, W., Wang, Y., Bao, J., Pei, S. S., "Kinetic study of graphene growth: Temperature perspective on growth rate and film thickness by chemical vapor deposition", ***Chemical Physics Letters***, Vol. 580, (2013), 62-66. https://doi.org/10.1016/j.cplett.2013.06.047
40. Kim, H., Mattevi, C., Calvo, M. R., Oberg, J. C., Artiglia, L., Agnoli, S., Hirjibehedin, C. F., Chhowalla, M., Saiz, E., "Activation energy paths for graphene nucleation and growth on Cu", ***ACS Nano***, Vol. 6, No. 4, (2012), 3614-3623. https://doi.org/10.1021/nn3008965
41. Malard, L. M., Pimenta, M. A., Dresselhaus, G., Dresselhaus, M. S., "Raman spectroscopy in graphene", ***Physics Reports***, Vol. 473, No. 5-6, (2009), 51-87. https://doi.org/10.1016/j.physrep.2009.02.003
42. Thomsen, C., Reich, S., "Double resonant Raman scattering in graphite", ***Physical Review Letters***, Vol. 85, No. 24, (2000), 5214. https://doi.org/10.1103/PHYSREVLETT.85.5214
43. Wu, J. B., Lin, M. L., Cong, X., Liu, H. N., Tan, P. H., "Raman spectroscopy of graphene-based materials and its applications in related devices", ***Chemical Society Reviews***, Vol. 47, No. 5, (2018), 1822-1873. https://doi.org/10.1039/C6CS00915H
44. Zhang, Y. Y., Gu, Y., "Mechanical properties of graphene: Effects of layer number, temperature and isotope", ***Computational Materials Science***, Vol. 71, (2013), 197-200. https://doi.org/10.1016/j.commatsci.2013.01.032
45. Shukrullah, S., Mohamed, N. M., Shaharun, M. S., Saheed, M. S. M., Irshad, M. I., "Effect of CVD process temperature on activation energy and structural growth of MWCNTs", ***Metallurgical and Materials Transactions A***, Vol. 47, No. 3, (2016), 1413-1424. https://doi.org/10.1007/s11661-015-3303-8
46. Shen, Z., Li, J., Yi, M., Zhang, X., Ma, S., "Preparation of graphene by jet cavitation", ***Nanotechnology***, Vol. 22, No. 36, (2011), 365306. https://doi.org/10.1088/0957-4484/22/36/365306
47. Sharma, I., Dhakate, S. R., Subhedar, K. M., "CVD growth of continuous and spatially uniform single layer graphene across the grain boundary of preferred (111) oriented copper processed by sequential melting–resolidification–recrystallization", ***Materials Chemistry Frontiers***, Vol. 2, No. 6, (2018), 1137-1145. https://doi.org/10.1039/C8QM00082D
48. Yao, Y., Ren, L., Gao, S., Li, S., "Histogram method for reliable thickness measurements of graphene films using atomic force microscopy (AFM)", ***Journal of Materials Science & Technology***, Vol. 33, No. 8, (2017), 815-820. https://doi.org/10.1016/j.jmst.2016.07.020

Advanced Ceramics Progress: Vol. 8, No. 1, (Winter 2022) 44-55

Materials and Energy Research Center
MERC

Contents lists available at ACERP

Advanced Ceramics Progress

Journal Homepage: www.acerp.ir

Review Article

A Review on the Application of Nanoparticles for Targeted Gene Delivery

Solmaz Moniri Javadhesari [a,*], Masoud Jabraili [b], Mohaddeseh Koohi [c]

[a] *Assistant Professor, Department of Cellular and Molecular Biology, Faculty of Basic Sciences, Azarbaijan Shahid Madani University, Tabriz, East Azerbaijan, Iran*

[b] *MSc Student, Department of Cellular and Molecular Biology, Faculty of Basic Sciences, Azarbaijan Shahid Madani University, Tabriz, East Azerbaijan, Iran*

[c] *MSc, Department of Cellular and Molecular Biology, Faculty of Basic Sciences, Azarbaijan Shahid Madani University, Tabriz, East Azerbaijan, Iran*

* Corresponding Author Email: solmazmoniri@gmail.com (S. Moniri Javadhesari)

URL: https://www.acerp.ir/article_153518.html

ARTICLE INFO

Article History:

Received 6 June 2022
Received in revised form 10 July 2022
Accepted 17 July 2022

Keywords:

Nanoparticles
Gene Therapy
DNA
SiRNA
Targeted Nucleic Acid Delivery

ABSTRACT

Gene therapy is an attractive approach to treatment of diseases with genetic or non-genetic origins. This procedure is based on the delivery of genetic materials, mainly DNA or small interfering RNA (siRNA), to the target cells or tissues. Due to the presence of physical and chemical barriers in the internal environment and cells of the body such as degrading enzymes in the circulatory system or electrical charge of the cell membrane, transfection of the naked nucleic acids is inefficient. In order to overcome this problem, different types of gene transfer carriers were developed. Of note, nanoparticle-based carriers have attracted considerable attention owing to their particular properties. Nanoparticles (NPs) are available in different types, each with its own specific advantages and disadvantages. Some of their advantages such as their small size have made NPs a potential candidate for eliminating obstacles to the genetic material delivery. However, these NPs have several limitations. The current study aimed to introduce different types of NPs used in the delivery of genetic materials and examine the basic aspects of the fabrication, characterization, and functionalization of NPs. Further, it briefly summarized the advantages and disadvantages of each approach to gene delivery by means of NPs. Finally, it suggested some applications of the nanoparticle-based gene therapies in the clinical trials.

https://doi.org/10.30501/acp.2022.345741.1091

1. INTRODUCTION

Gene therapy is defined as the direct transfer of genetic materials to cells and tissues affected by either inherited or acquired diseases [1,2]. This procedure is considered to be a potential candidate for treatment or prevention of diseases resulting from defective gene expression [3]. This strategy involves introduction of genes (Figure 1) into the target tissues or cells to alter the expression of endogenous genes for therapeutic purposes or prevent further development of the associated disease [4]. Gene therapy is used not only for genetic disorders but also for other complex diseases such as viral infections (human immunodeficiency virus), autoimmune diseases (rheumatoid arthritis), coronary heart disease, cancer, diabetes, arterial disease, neurodegenerative disorders, hemophilia, AIDS, asthma, etc. [1,5].

The therapeutic molecules include nucleic acids,

Please cite this article as: Moniri Javadhesari, S., Jabraili, M., Koohi, M., "A Review on the Application of Nanoparticles for Targeted Gene Delivery", ***Advanced Ceramics Progress***, Vol. 8, No. 1, (2022), 44-55. https://doi.org/10.30501/acp.2022.345741.1091

antagonist oligonucleotides, and small interfering RNAs (siRNAs) facilitate the replacement of damaged gene or down regulation of undesirable gene expressions [3,6].

These molecules are large in size, easily degradable by enzymes, and characterized by anionic nature, characteristics that make their delivery quite difficult. In this regard, carriers play a significant role in the gene delivery to the target cells or tissues [3]. Hence, the existence of nucleic acid-transferring vectors is necessary to facilitate the transport of nucleic acid molecules to the cells [1].

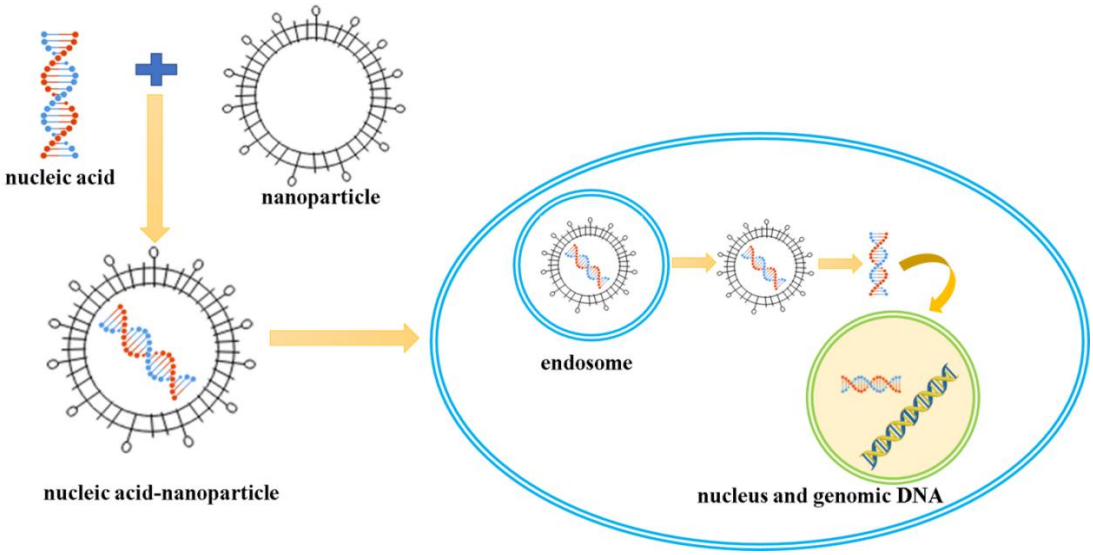

Figure 1. Nucleic acid delivery using nanoparticles

In general, there are two different methods of gene delivery depending on the carrier's characteristics namely the viral-mediated gene transfer and nonviral gene transfer using artificial carriers [7]. The effectiveness of the viral vectors in the delivery of nucleic acids is greater than that of non-viral ones. However, the carriers of viral vectors might considerably threaten the patients' health while the non-viral carriers of genes are inherently safer than the vectors of viruses [1,8].

In addition, these viral carriers have other limitations such as limited cell targeting and gene transport capacity as well as relatively high large-scale production costs. Non-viral carriers carry a wide range of nucleic acids, hence they are robust that can be used for large-scale production [3]. In ideal situations, gene transfer systems should be stable, biologically compatible, non-toxic, and highly efficient transfection systems. Nanoparticles (NPs) are ideal platforms that can be used among different nonviral nucleic acid carriers [7].

NPs, usually referred to as the dispersed or solid particles ranging from 1 to 100 nm in size, were found to be effective tools for gene delivery. NPs with quite small sizes can travel in the circulatory system and pass throgh many physiological barriers.

The high ratio of the surface area to the volume facilitates modification of the surface of particles with functional groups to control the pharmaco-kinetics and bio-distribution of the particles [9]. NPs are categorized into four main groups namely the polymer-based, lipid-based, inorganic, and hybrid NPs (Figure 2) [1,4].

This study presents a review of the different types of NPs, ways of NP production, clinical development of gene-transferring NPs, and toxicity of NPs.

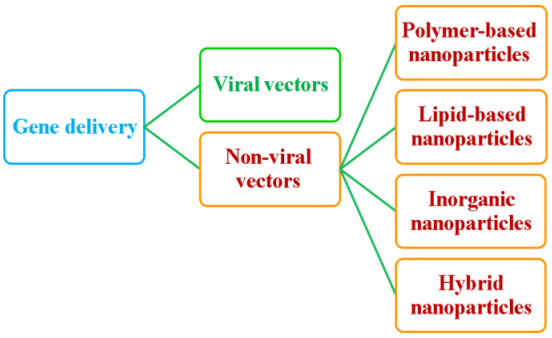

Figure 2. Gene delivery approaches

2. DIFFERENT TYPES OF NPS

2.1. Polymer-Based NPs

There is a positive charge in the spine in these polymers that supports their interactions with the negatively charged anionic nucleic acid materials. The binding of the cationic polymers to the DNA molecules can form nanometric complexes called the polyplexes [1]. Such NPs can be produced using biopolymers or synthetic

polymers [10]. Biopolymers are defined as the macromolecules produced from living organisms that are divided into three groups namely the proteins, polysaccharides, and nucleic acids [1].

Proteins with natural origin such as albumin, collagen, gelatin (a natural protein obtained from the degeneration of collagen with great biodegradability and biocompatibility in physiological conditions [11]), elastin, β-casein, fibronectin, zein, and silk protein are commonly used to produce biomaterial NPs [1,12]. A polypeptide polymer called the Poly-L-Lysine (PLL) is the earliest polymer as for non-viral gene delivery carrier [12]. Polysaccharides as another group of biopolymers are long molecules of carbohydrate that are made of repeating units of monosaccharide. These materials contain chitosan, pullulan, hyaluronic acid, alginate (a natural polysaccharide obtained from brown algae which is composed of alpha-l-guluronic acid and beta-d-mannuronic acid units [13]), dextran, cyclodextrin, heparin, and lignin [1,12]. Synthetic polymer-based NPs have also drawn considerable attention in recent years [14]. Polylactic Glycolic Acid (PLGA)-based NPs, polyethyleneimine (PEI), dendrimers, Polyethylene Glycol-Cationic Polylactide (PEG-CPLA) copolymers, and Polyion Complex Micelles (PIC) are some examples of synthetic polymers [1,12].

Polyethylenimine is able to condense the DNAs into a polyplex, hence widely used as a gene transferring vector [12]. There are two types of polyethylenimines available called the branched and linear with different molecular weights [3]. Dendrimer is a three-dimensional polymer characterized by a spherical structure with many branches. Polyamines, polyamides, or polyesters are the frequently used dendrimers. Polyamidoamines (PAMAMs) are also the most commonly used dendrimers [1,15].

2.2. Lipid-Based NPs

Cationic lipids, cationic solid lipids, cationic liposomes, cationic emulsions, lipidoids, and gemini surfactants are the lipid-based NPs generally used for gene delivery [1,12]. Cationic lipids are positively charged molecules of amphiphilic such as dioleoyl trimethylammonium propane (DOTAP) and Dioleylpropyl trimethylammonium chloride (DOTMA) [1]. Cationic liposomes are liposomes containing a positively charged lipid and a helper lipid that can keep nucleic acids from enzymatic deterioration in the bloodstream and interact with cell membranes with negative charge to intense internaling cell [1].

The main components used for fabrication of liposomes are 1,2-dioctadecanoyl-sn-glycero-3-phospho ethanolamine (DSPE) and dioleoylphosphatidylcholine (DOPC) or dioleoylphosphatidylethanolamine (DOPE) [7,9]. Solid Lipid NPs (SLNs) or cationic solid lipid core-shells are made from high-melting temperature lipid molecules as the core of the particle and surfactants as the shells around the particles [1]. Production of cationic emulsions involves a hydrophobic oil phase covered with cationic lipids [1]. Lipidoids or Lipidoid Nano-Particles (LNPs) are small molecules similar to the lipids that have recently been explored as the RNA interference gene transferring vehicles [12].

Gemini surfactants are basic structures composed of more than two polar head groups and two hydrophobic tails connected by a molecule as the space creator [12]. Gemini are found in four main types of surfactants namely the m-s-m (N, N-bis (dimethyl alkyl)-α, ω-alkanediammonium), peptide-stabilized, carbohydrate-based, and disulfide-bearing gemini surfactants [12].

2.3. Inorganic NPs

There are different types of inorganic NPs including Carbon Nano-Tubes (CNTs), graphene oxide, calcium phosphate NPs, Magnetic Nano-Particles (MNPs), silica NPs, Gold Nano-Particles (GNPs), silver NPs, and Quantum Dots (QDs) that are often used as the carriers for nucleic acid transportation [1,12]. In addition, zinc oxide NPs (ZnO NPs) are regularly utilized as different biomolecules delivery vehicles (gene, drug, etc.) [16]. CNTs are nanosized fibers with high specific surfaces [17]. Owing to their needle-like nanostructure, CNTs can traverse through the plasma membrane easily in an endocytosis way without causing considerable cell death [1]. They are usually insoluble materials that need surface functionalization for their stablization in solvents. Considerable attention has been paid to the CNTs (with either single- or multi-walls) owing to their wide applications in the field of gene therapy [9]. Magnetic NPs are another type of synthetic particles in submicron size that react with magnetic fields [1]. For example, super paramagnetic iron oxide NPs (Fe_3O_4) or SPIONs are used in these nucleic acid transferring systems [9].

Calcium phosphate NPs are extensively used for gene transfection as the in vitro that have been thoroughly inspected as an advanced non-viral nucleic acid delivery. Application of silica NPs have been recently suggested as the non-viral vectors of in vivo gene delivery [1]. Metallic NPs, especailly gold NPs, are superior to their counterparts in terms of their simplicity of the synthesis method, high efficiency in gene transfection, and high capability of their surfaces in undergoing chemical modifications [1].

QDs are successfully used for in vivo and in vitro gene transfection. These vectors are approximately spherical semiconductor NPs characterized by core-shell structures [1]. QDs are also called nanocrystals mainly because they are nanometer-sized monodisperse crystals [12].

Graphene is an attractive nanomaterial. This allotrope of carbon enjoys favorable thermal, optical, and electrical advantageous properties. For instance, Graphene Oxide (GO) in protection of nucleotides from cleavage, makes it a proper gene delivery vector [1,18].

2.4. Hybrid NPs

Hybrid NPs are divided into two groups of multi-layer and Liposome-Polycation-DNA (LPD) NPs. LPD NPs are primarily manufactured through the spontaneous reorganization of the lipid layer around the polycationic DNA core, and arrangement of polycations and polyanions Layer-by-Layer (LbL) results in the fabrication of multi-layer NPs. Contrary to the cationic polypeptides like histone, poly-L-lysine, and protamine that are able to flexibly package the DNA molecule, polycations in multi-layer NPs are condensing polyanions (e.g., DNA) in highly compressed nanometric structures [1,19]. There are other types of hybrid vectors. For instance, theranostic nanomaterials comprises both organic and inorganic NPs and provides specific disease management nanosystems by combining different NP platforms (therapeutic and diagnostic capabilities) into one biocompatible and biodegradable NP [7]. In fact, theranostic nanosystems are multifunctional [20]. Of note, hybrids of polysaccharides and proteins are sometimes utilized to fabricate gene delivery carriers. NPs based on the core-shell structures of Albumin-chitosan-DNA are inquired for gene transportation purposes. Further, dendrimer-like hybrid silica NPs are functionalized nano-scale carriers that can be appropriate candidates for simultaneous and efficient delivery of different types of drugs or genes with different sizes [1]. A list of NPs that are developed for gene delivery puposes are summarized in Table 1.

TABLE 1. Different types of NPs developed for gene delivery

Type of NPs	Materials that have been used	Ref(s)
Polymer-based NPs	Collagen	[1]
	Elastin	[1],[12]
	Fibronectin	[1]
	Silk proteins	[1],[9],[12]
	Albumin	[1],[12]
	β-casein	[1]
	Zein	[1],[12]
	Gelatin	[12]
	Poly-L-lysine (PLL)	[12]
	Chitosan	[1],[7]
	Alginate	[1]
	Heparin	[1]
	Hyaluronic acid	[1]
	Pullulan	[1]
	Dextran	[1]
	Cyclodextrins	[12]
	Lignin	[12]
	Polyethylenimine	[1],[12]
	Dendrimers	[1],[15]
	Poly lactic-co-glycolic acid (PLGA)	[1]
	PEG-CPLA copolymers	[12]
	Polyion complex micelles (PICs)	[1]
Lipid-based NPs	Liposomes	[1]
	Cationic lipids	[1]
	Cationic solid lipids	[1]
	Cationic emulsions	[1]
	Lipidoids	[12]
	Gemini surfactants	[12]
Inorganic NPs	Carbon nanotubes (CNTs)	[1],[12]
	Magnetic NPs (MNPs)	[1],[12]
	Calcium phosphate	[1],[12]
	Silica	[1]
	Gold	[1],[12]
	Silver	[12]
	ZnO	[16]
	Quantum dots (QDs)	[1],[12]
	Graphene oxide	[12]

3. FABRICATION OF NPS

Advancement of clinically felicitous NPs for gene therapy still faces many problems such as biocompatibility and biodegradation, aggregation of NPs in physiological fluids, non-specific adsorption by non-target tissues, inefficient extravasation to reach desired tissues, unwanted entrance to the target cells, and endosomal escape [4].

Fabrication of the commonly used NPs is elaborated in the following with the main emphasis on some approaches that help overcome the mentioned problems.

3.1. Polyethylenimine

PEI is a cationic polymer that is commonly used as an effective nucleic acid delivery vector. As observed in Figure 3, there are two branched or linear forms of PEI. Gene transferring efficacy and cellular toxicity of PEI originally depend on its size, molecular weight, and polymer:nucleic acid charge ratio. In this regard, several researches highlighted that PEI with higher molecular weight (> 25 kDa) was more toxic than small and medium-sized polymers (5-25 kDa), hence less effective at gene delivery [9].

Typically, aziridine monomers are polymerized in aqueous or alcoholic solutions in order to prepare branched polyethylenimine polymers. Initial concentration of the components and temperature of the reaction are two key regulators in the procedure of constructing PEI of different molecular sizes that finally lead to production of randomly branched polymers. Similarly, linear structures of polyethylenimine result from the polymerization of cationic ring and unrolled ethyl-2-oxazoline to poly (2-ethyl-2-oxazoline). In this procedure, partial hydrolysis with an acid or base catalyst lead to the generation of linear polyethylenimines. The molecular weight and degree of branching can be controlled by changing the conditions of each process. Essentially, such high-charge polymers are proved to be ideal vectors for condensation of nucleic acids and transfer of genes in vitro and in vivo. However, high charges can cause damages to the cells and tissues due to their toxic nature. In general, the effectiveness of the PEI-based vectors can be affected by some parameters namely

the positive charge density, degree of branching, molecular weight, cross-linking, buffering capacity, etc. These parameters directly affect the DNA binding properties of the PEI, surface charge magnitude, and size of the prepared compounds [3].

PEIs with different molecular weights ranging from 430 to 800,000 Da were investigated in terms of their efficiency in gene transfer, and the transfection efficacy of 25 kDa PEI was found to be the best in vitro.

The cytotoxicity of the PEI results from the polymer aggregation on the surface of cells. On the contrary, less cytotoxicity of the low molecular weight PEI results from the diminished surface charge [21]. The stability of the PEI polyplex can be enhanced by modifying the periphery of the Polymer. The serum-tolerant capacity of the polyplex can be significantly improved by introducing hydroxyl groups. In addition, PEGylation as the most commonly used method can create a hydrophilic outer layer that lessens non-specific interactions with serum components and clearance by phagocytosis mechanism [7].

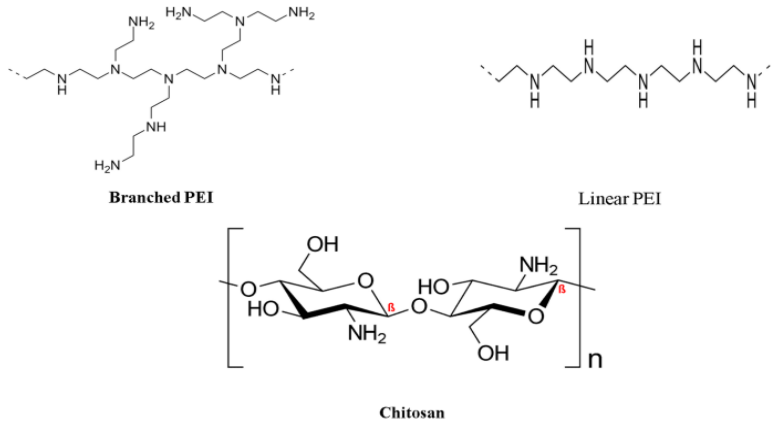

Figure 3. Structures of branched PEI, linear PEI [23], and chitosan [24]

3.2. Chitosan

Chitosan is derived from chitin which is the main component of cell walls of fungi, exoskeletons of crustacean and insect, and scales of fish. It is a positively charged polymer made of (1–4)-2-amino-2-deoxy-β-D-glucan (Figure 3) [22]. Owing to its cationic nature, the chitosan polyelectrolytes facilitate strong electrostatic interactions with mucus, mucosal surfaces with negative charges, and negatively charged macromolecules such as the DNA. In addition, presence of amine groups in the structure of chitosan made this biocompatible, biodegradable, and non-toxic polymer applicable as an attractive vector for non-viral gene transfer. Chitosan can form small stable particles (20 to 500 nm) with the plasmid DNA, and its binding efficacy depends on the molecular weight as well as the degree of deacetylation. Chitosan shows higher protective ability against DNase digestion and better biocompatibility than other polymers such as PEI. In the beginning, the efficacy of the DNA transfection by means of chitosan was slow; however, the transfection efficiency increased over time with lowering cytotoxic consequences in vivo [1].

Chitosan is a biologically degradable polymer, yet its limited transfection efficiency confines its application as a gene transferring vector [7]. Chitosan NPs can be chemically modified initiating from the base polymers or produced NPs. To this end, reactive hydroxyl and amino groups of chitosan are used at different temperatures in different alkaline conditions. Among the examples are alkylation, thiolation, carboxylation, quaternization, and PEGylation.

Chemical modifications is primarily performed as an additional process to improve the solubility, efficiency of encapsulation, and enzyme inhibition and adhesion properties [22].

3.3. Dendrimers

The role of dendrimers in gene, siRNAs, and antisense oligonucleotides transfer was also investigated in some studies. The positively charged surface groups of dendrimers can interact with negatively charged nucleic acids. Spherical nanoscopic polymers of PAMAM are a type of dendrimer generally used for nucleic acid transfection. Small dendrimers can provide better DNA binding efficiency than larger dendrimers.

In a study, a unique complex of PAMAM could cross the Blood-Brain Barrier (BBB). In fact, a peptide was derived from the glycoprotein of Rabies virus (named RVG29 peptide)[1] which is bound to PAMAM via bifunctional PEG as well as a system compounded with nucleic acids to generate PAMAMPEGRVG29/DNA NPs.

PAMAMPEGRVG29/DNA NPs confirmed more efficient crossing through the BBB than the

[1] The sequence of RVG29 is YTIWMPENPRPGTPCDIFTNSRGKRASNGC

PAMAM/DNA in the in vitro BBB model57. It was taken up endocytotically by the endothelial cells of brain capillaries, a phenomenon that can be inhibited by free RVG29 [9].

3.4. Liposomes

Liposomal formulations optimized for gene transfer are usually composed of a complex of charged and neutral lipids (helper lipid), often DOPE or DOPC. These neutral lipids help form the lipid bilayer of liposome [9,12]. In DNA-binding studies mediated by N-(1-(2,3-dioleoyloxy) propyl)-N,N,N-trimethylammonium chloride (DOTAP), DNA was not efficiently combined with liposomes made without DOPE [9].

Cationic liposomes modified by grafting PEG or PEG-introduction methods demonstrated that in the presence of serum, the transfection efficiency of the conventional liposomal compounds was diminished while the related efficacy of the PEG-added compounds was retained. In addition, the transfection efficacy of the traditional gene delivery compounds considerably decreased during storage. However, the transfection efficiency remained stable for the PEG-containing liposomal gene transfer compounds even after storage for two weeks [25].

3.5. Gold NPs

Gold NPs (Au-NPs) possess flexible surfaces that support their functionalization. This allows nucleic acids to be directly compbined with gold NPs. Coating of gold NPs with antibacterial Peptides (PEP) or Transactivators (Tat) of transcriptional peptides can be used for more efficient gene delivery to the stem cells [12].

For gold NPs, increasing the particle-to-DNA ratio (20:1) notably improved the transfection efficiency. Sandhu et al. studied gene transfer using gold NPs modified by N,N,Ntrimethyl(11-mercaptoundecyl) ammonium chloride and alkyl thiol in different chain sizes. Based on the best formulation for NP in their study, the transfection efficiency was about eight times more than that of the PEI [9].

3.6. Carbon Nanotubes

The small size of the CNTs and their chemical inactivity are attractive features for gene transfer but their hydrophobicity makes them less soluble in aqueous solution, thus limiting their applicability in biological systems. CNTs can be synthesized through covalent or non-covalent interactions to improve their dispersion and solubility. Oxidations and cyclo-additions are the two most ordinary covalent functionalization reactions. Another approach to non-covalent functionalization of CNTs is coating with amphipathic molecules such as Sodium Dodecyl Sulfate (SDS) or proteins [12]. Covalent modification of carbon nanotubes can be carried out using the 1,3-dipolar cycloaddition reaction of azomethine ylides. Both Single- and Multi-Walled Carbon Nanotubes (SWNT and MWNT) are functionalized with a pyrrolidine ring equipped with a free oligoethylene glycol moiety attached to the nitrogen at amino-terminal. Attachment of this functional group significantly increases the solubility of CNTs, especially in aqueous solutions [26].

4. MECHANISMS OF DNA-NP BINDING

One of the main applications of NP-based approaches is developing sensitive and specific medical diagnostics and delivery of nucleic acids to cells or tissues. Specific or non-specific molecular binding between nucleic acid molecules and NPs can provide high sensitivity. Covalent bindings between nucleic acids and NP surfaces are formed by anchor groups (–OH, –SH—COOH, or NH_2). In general, thiolated oligonucleotides can functionalize gold (Au) or silver (Ag) NPs to generate nucleic acid NP probes for specific recognition of complementary nucleic acid sequences in testing DNA mutations and polymorphism studies. In addition, non-covalent adsorption between nucleic acids and NPs result in non-specific interactions. Similar to the nucleic acid-protein interactions in vivo, this approach requires the affinity of non-covalent binding to control nucleic acid release in gene regulation or therapy. In this regard, a better understanding of the interactions between nucleic acids and NPs at the atomic level plays a crucial role in developing such approaches. Researchers declared that binding of short ss-DNA of 24-mer to 13 nm gold NPs could significantly prevent aggregation while complementary hybridized oligomers failed in stabilization of the gold NPs, thus resulting in aggregation of Au-NPs in saline mixtures [27].

Evaluation of the affinity with the deoxynucleosides-Au-NP binding confirmed the strong affinity between the four deoxynucleosides namely the Adenine, Thymine, Guanine, and Cytosine. Contrarily, the thymine showed the weakest affinity with the gold surface among the others. The negative charge distributed on the backbone of nucleic acid molecules mediate their adsorption on NP surfaces through the Fe-O-P interactions. Researches highlighted the crucial role of electrostatic interactions and hydrogen bonds formation in the adsorption of DNA/RNA to IONPs (iron oxide NPs) [28].

4.1. DNA–Gold NP Binding

Given that Au-NPs have negative charge on their surface, they are regarded as the selective vectors for delivery of ss-DNAs. The binding of the gold NPs to the ds-DNA is not favorable due to the higher repulsion between ds-DNA and negative charges on the surface of gold NPs. The longer ss-DNAs cause weaker interactions with Au-NPs, and binding of long ss-DNA molecules to gold NPs occurs just at high temperatures. In addition, the size of NPs is a significant part of interaction between

DNA and NPs [27,29].

4.2. DNA–Silver NP Binding

Silver NPs were functionalized to detect specific sequences of nucleic acids. Then, NPs of oligonucleotide-Ag provide ultrasensitive DNA detection systems. The results from several studies referred to the sequence-dependent interactions of DNA and Ag-NPs, thus suggesting the close affinity between nucleotides and silver NPs with variable attraction strength as the order C > G > A > T. It was also found that Ag NPs could efficiently bind to the ds-/ss-DNA molecules. As a result of the potential of negative zeta of the Ag-NPs, an electrostatic attraction between Ag-NPs and negatively charged DNA backbone would seem unlikely.

Accordingly, DNA-Ag complexes were formed through coordination coupling. Silver NPs could interact with N7 atoms of purines (A & G) and N3 atoms of pyrimidines (T & C) [30,31].

4.3. DNA-CNT Binding

Different nanomaterials of carbon were studied with the main focus on the DNA-NP binding, and the findings revealed that single-walled CNTs were bound to ss-DNAs. Molecular simulation studies also suggested that torsional and electrostatic interactions of DNA backbone may drive wrapping of DNA molecule around SWNTs in order to form compact helices that can be used in gene therapy approaches [32,33].

5. THE APPLICATION OF NPS IN GENOME EDITING

In recent years, a versatile genome editing system known as CRISPR-Cas9 (Clustered Regularly Interspaced Short Palindromic Repeats and CRISPR-associated protein 9 (Cas9)) has emerged as an efficient tool to carry out precise mutations and gene targeting. It can perform gene replacements, gene deletions/ insertions, and single base pair conversions [34].

Since the nuclear genome is the target of CRISPR/Cas9 complex, the components of this system are required to be transported to the nucleus. In this regard, CRISPR/Cas9 is needed to pass through the barriers of cellular and nuclear membrane and nanocarriers can fulfill this purpose. For example, nanocarriers based on polymers such as block polymer PEG-b-PLGA, lipid-based NPs, chitosan, and PEI or Au-NPs can transfer the CRISPR/Cas9 complex into nucleus [35].

6. DEVELOPMENT OF NPS FOR GENE DELIVERY AND CLINICAL APPLICATIONS

Gene therapy is the methodology of correcting genetic errors in living organisms either by delivery of exogenous integrating/non-integrating nucleic acids or modification of the gene expression to prevent or treat the disease. Recently, a wide variety of NPs have been functionalized for delivery of DNA and RNA to the cells or tissues of interest. These novel Nano-systems can be utilized as alternatives for viral vectors. Gene delivery through nanomaterials enjoys several advantages such as lower immune response than that of viral vectors, highly flexible design, low cytotoxicity, and feasibility of targeted gene delivery to the cells and tissues in vivo and in vitro [36].

Two basic approaches to gene therapy are (i) introduction of a functional gene in order to recover the function of related defective gene and (ii) antisense technology that is the delivery of interfering RNAs such as siRNA, micro RNA (miRNA) or short hairpin RNA (shRNA) to modulate post transcriptional gene expression by degrading the mRNA of interest or repressing its translation, or through Antisense Oligo-Nucleotides (AONS) that are single stranded nucleic acids directly finding their complementary sequences of mRNAs without the aid of auxiliary cellular mechanisms. The second approach is usually employed to treat tumors or other genetic disorders caused by upregulation of specific genes [36,37].

Nanomaterials are the delivery vectors for small RNA molecules [37]. For novel nanomaterials, the approaches to gene delivery are still developing. In this respect, the key challenges are how to make a balance between transfection efficiency, targeting specificity, particle size, biodegradability, and cytotoxicity as well as their short- and long-term fates in the environment [38].

Application of nucleic acid delivery in clinics is still in its infancy, and the FDA has not yet approved the NP-based gene therapy [1,4]. In the following, several cases of clinical applications of NPs in gene transfer are introduced (Figure 4).

A study took into account the HER2 expression based on some cancerous cells as a principal for developing the targeted NPs. HER2 is a tumor marker gene that is commonly upregulated in certain tumors such as ovarian and breast cancer. A monoclonal antibody called the Herceptin (HER) can selectively recognize HER2 and target the HER2+ cancerous cells [7]. Magnetic antifouling iron oxide NPs (IONPs) coated with block copolymer poly(ethylene oxide)-block-poly (γ-methacryloxypropyltrimethoxysilane) (PEObPγMPS) was also utilized to improve cell targeting by reducing non-specific uptake. Attachment of Herceptin, the antibody of HER2 or a single-chain fragment (ScFv) of anti-epidermal growth factor receptor (ScFvEGFR) antibody to the IONPs coated with PEO-b-PγMPS resulted in HER2- or EGFR-targeting IONPs (anti-HER2-IONP or ScFvEGFR-IONP). In vitro studies demonstrated that anti-HER2-IONPs could specifically bind to SK-BR-3, a HER2 overexpressing breast cancer

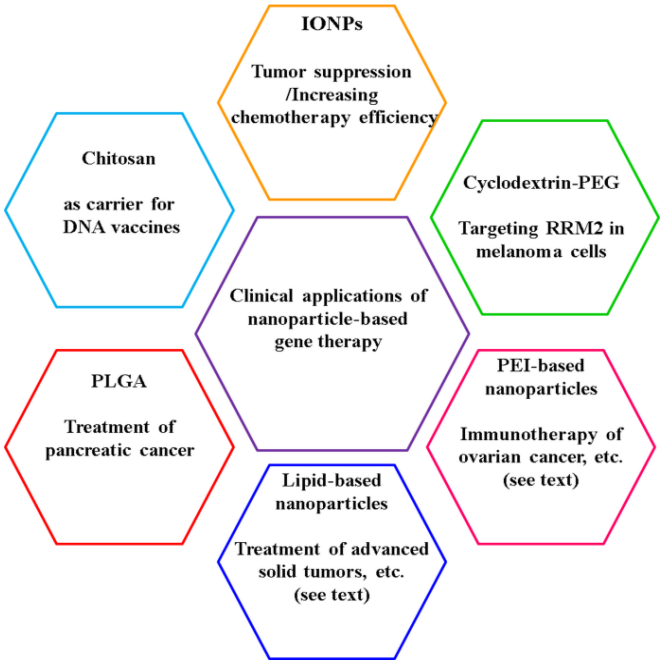

Figure 4. Clinical applications of nanoparticle-based gene therapy

cell line, but it failed to bind to the HER2 underexpressing MDA-MB231 cell line. Furthermore, ScFvEGFR-IONPs exhibited strong reactivity with EGFR-positive MDA-MB231 human breast cancer cell line but not with an EGFR-negative human breast cancer cell line, i.e., MDA-MB453. Transmission electron microscopy was employed to demonstrate the internalization of NPs targeting the receptors of cancerous cells. Of note, non-specific uptake of IONPs by macrophages of RAW264.7 mouse was reduced for both antibody-conjugated and non-antibody-conjugated NPs in vitro. The produced IONPs exhibited long persistence in blood circulation with the half-life of 11.6 hours in serum and lowered accumulation in spleen and liver of mice. Administration of ScFvEGFR-IONPs into the circulatory system of mice bearing EGFR-Positive breast cancer 4T1 mammary carcinoma showed a reduction in the magnetic resonance imaging signals in the tumors at 24 hours after administration due to the accumulation of the targeted IONPs [39]. These targeted IONPs can be complexed with therapeutic nucleic acids and applied as site specific gene delivery vectors to carry the nucleic acids for disease treatment purposes.

Davis et al. reported he first gene delivery system based on the NPs, called CALAA-01 in a Phase I clinical trial for cancer. CALAA01 is made of a polymer containing cyclodextrin, siRNA that target M2 subunit of ribonucleotide reductase (RRM2), PEG stereostabilizer agent, and ligand that target the transferrin for attachment of NPs to the transferrin receptors that are upregulated on the cancer cells 71. According to the results, the systemic administration of this "drug" carried the siRNA component into the melanoma cells and potentially showed the antiproliferative effect on the multiple types of cancerous cells [4].

IONPs are a group of NPs that can carry the targeted nucleic acids, basically in the form of plasmid DNA or siRNA, in order to regulate the altered expression of genes resulting from the carcinogenesis process. It should be noted that the IONPs have the potential to improve the efficiency of gene therapy. The complexes of IONP-gene make feasible the delivery of nucleic acids to the organ of interest such as a tumor and function against the tumor either directly or indirecyly.

In the direct delivery, IONPs that are bound to siRNA (siPLK1) act on a cell cycle-specific serine/threonine kinas (pololike kinase-1) and two peptides (MUC1 and) are injected into tumor-bearing mice. Then, the IONPs accumulate in the tumor, efficiently silence PLK1, and suppress the tumor by increasing apoptosis.

In the indirect delivery, IONPs that carry the phosphatase and tensin homolog (PTEN) gene increase the sensitivity of A549 / CDDP lung cancer cells to cisplatin treatment, indicating that PTEN can be effectively utilized against cisplatin-resistant lung cancer cells [40].

Inorganic MNPs are commonly used for gene delivery. Typically, MNPs in combination with a delivery platform encapsulate nucleic acids and facilitate their uptake by cells. However, the efficacy of the MNPs as nucleic acid carriers or drug delivery vectors depends on the modification of the outer surface of the NPs to permit binding of target molecules. The desired therapeutic molecules are attached to the NPs by cleavable linkers or

electrostatic attraction between the magnetic NP and target molecule. Novel reseraches have been conducted on how to find ultra-small and biologically compatible magnetic NPs that assist genetically modified cells such as macrophages and monocytes with efficient uptake by tumors after systemic administration [41].

In gene therapy, silica-based carriers are preferred to other non-viral/viral vectors due to their high safety level, flexibly modifiable surface and structure, great stability, and affordable costs. Silane is a versatile material with high combinatory features with lipids, polymers, and inorganic NPs. Silica NPs provide high loading capacities, efficient nucleic acid interaction and protection, specific tissue targeting, and cargo releasing. In this regards, several gene therapy approaches have been recently developed based on the silica NPs, e.g., forward and reverse transfection as well as sedimentation agents (non-porous NPs). Silica-based gene therapy yielded promising results both in vitro and in vivo for therapy or imaging purposes [42].

PEG – PEI - Cholesterol (PEGPEIcholesterol) was successfully developed as a carrier for gene transfer in the immunotherapy of epithelial ovarian with upregulated cytokine interleukin 12. Moreover, some gene therapy approaches with the main focus on the NPs are commonly employed in clinical trials such as PEI-based NPs which is used for treatment of ovarian, bladder, and pancreatic cancers, lipid-based NPs for treatment of advanced solid tumors, transthyretin amyloidosis, hepatocellular carcinoma, liver metastases, and lung cancer [4].

Poly (lactic-co-glycolic acid) (PLGA) is a synthetic polyester with favorable properties including thermoplasticity, biocompatibility, and aliphatic nature. Specific formulations were proposed based on this polymer and its relevant homopolymers, poly (lactic acid) (PLA), and poly (glycolic acid) (PGA). The potential of the PLGA NPs as nanocystems for drug delivery was proved for many therapeutic agents including proteins, antioxidant drugs, anti-inflammatory, antibiotics, antiseptics, and chemotherapeutic agents. Then, it can be suitable for targeting tumors and/or DNA [43]. For example, clinical evaluation of the PLGA-based NPs are under consideration for the treatment of pancreatic cancer [4].

Chitosan-based NPs can used for delivery of both DNA and siRNA. Studies highlighted the potential of chitosan NPs as the DNA vaccine carrier and adjuvant for effective immunization through a non-invasive nasal route [44].

6.1. The Effect of the Size of NPs on Gene Therapy

The size of NPs is considered as a significant factor in their in vivo/vitro applications that also affects their cellular delivery, efficacy of transfection, bio-distribution, and cytotoxicity. The NPs of 200 nm or less in size typically benefits endocytosis mediated by clathrin, and those of more than 200 nm in size are usually transferred through caveolar endocytosis. As shown, the NPs with the size of 100 nm and less efficiently enter a wide variety of cell lines while the NPs of 50 nm in size are the optimum size for uptake by cells. However, the impact of NP size on the transfection efficiency is, to some extent, conflicting. There are reports on the higher efficiency of transfection with smaller NPs (< 200 nm) while some others show the better transfection efficacy of larger NPs (> 200 nm). In addition, smaller NPs have larger surface areas capable of exposing higher percentage of molecules on their surface that led to high cytotoxicity of these NPs. Furthermore, small NPs, particularly NPs coated by biocompatible polymers (such as PEG), were found to be persistant in the blood circulatory system for a long time, and NPs conjugated to the targeting ligands showed better cellular penetrance. Overall, it can be concluded that the NPs with the size of 100 nm and smaller coated by biologically compatible polymers and attached to the targeting ligands can play a critical role in ensuring the success of nucleic acid transfer in clinical concerns [45].

7. TOXICITY OF NPS

NPs have great potential for improving gene therapy; however, their toxicity-related risks are inevitable. Determination of the toxicity and safety profile of a NP system for clinical utilization can be significantly challenging given the variety of factors involved including the size, shape, composition, stability, surface chemistry, electromagnetic properties of the nanopartciles as well as the genetic and existing conditions of the intended individual. Depending on the composition and size of the NPs, they can induce irreversible cell damages through oxidative stress and/or organelle damage [9]. Moreover, NPs can induce intracellular calcium (Ca^{2+}) perturbation in homeostasis, thus resulting in molecular actions attributed to energy and metabolic imbalances as well as cellular dysfunction [46].

The physicochemical properties of the developed NPs notably affect how they interact with the target cells and determine their potential overall toxicity. A better understanding of these properties can facilitate the fabrication of safer less toxic NPs [46].

Indeed, most inorganic NPs are biologically toxic. To be specific, while lipid-based and hybrid NPs are toxic in high doses, NPs based on polymers are less toxic to cells [1]. For example, the toxicity of the CNTs depends on their size. In animals, while single-walled CNTs are taken up easily by macrophages, the multi-walled CNTs have a carcinogenic effect similar to that of the asbestos after injection into a peritoneal cavity. However, when accumulated in the liver in the long run, single-walled CNTs will cause disturbance in some biochemical

parameters in the form of alanine transaminase, aspartate transaminase, LDH, malondialdehyde, and glutathione and alter the organ indices among the laboratory animals [47].

There are evidence of the adverse health effects of long exposure to NPs on the brain (neurodegenerative diseases such as Alzheimer's disease and Parkinson's disease), cardiovascular diseases (Hypertension, atherosclerosis, thrombosis, arrhythmia, vasoconstriction, heart disease), lungs (emphysema, asthma, cancer), gastrointestinal system (colon cancer, Crohn's disease), and skin (dermatitis, autoimmune disease) [9].

8. CONCLUSION

Gene delivery to cells or tissues is a critical step in gene therapy of diseases with genetic or non-genetic origin in order to treat or alter the molecular mechanisms that cause different diseases. Transferring the genetic materials to the cells is bound to a number of biological and other limitations. To overcome these limitations and facilitate gene delivery process, noanoparticle-based carriers have been recently developed. These types of carriers are found in a wide variety including polymer-based, lipid-based, inorganic, and hybrid NPs that can be fabricated through different approaches and functionalized for different purposes. Despite the positive characteristics of each NP, they have some advantages and disadvantages that should be simultaneously taken into consideration in special gene therapy approaches. One of the main problems in the application of NPs as the gene delivery carriers is their toxicity. In this respect, a balance should be made between the advantages and disadvantages of each NP which is a critical step in transferring genetic materials by NPs that may result in the development of specific and safer clinically applicable gene therapy approches that are promising in treating many diseases.

ACKNOWLEDGEMENTS

I would like to thank Azarbaijan Shahid Madani University for financial support of this work.

NOMENCLATURE

Au-NPs	Gold-Nanoparticles
CNTs	Carbon nanotubes
CPLA	Cationic polylactide
CRISPR	Clustered regularly interspaced short palindromic repeats
DOPC	Dioleoyl phosphatidylcholine
DOPE	Dioleoyl phosphatidylethanolamine
DOTAP	Dioleoyl trimethylammonium propane
DOTMA	Dioleoyl propyl trimethylammonium chloride
ds-DNA	Double-stranded DNA
DSPE	1,2-dioctadecanoyl-sn-glycero-3-phosphoethanolamine
EGFR	Epidermal growth factor receptor
FDA	Food and drug administration
GNPs	Gold Nanoparticles
GO	Graphene oxide
HER	Herceptin
IONPs	Iron oxide Nanoparticles
LbL	Layer-by-layer arrangement
LNP	Lipidoid Nanoparticles
LPD	Liposome-polycation-DNA Nanoparticles
miRNA	Micro RNA
MNPs	Magnetic Nanoparticles
MWNTs	Multi-walled carbon nanotubes
NPs	Nanoparticles
PAMAM	Polyamidoamine
pDNA	Plasmid DNA
PEG	Polyethylene glycol
PEG-b-PLGA	Polyethylene glycol-b-poly (lactic-glycolic acid)
PEI	Polyethyleneimine
PGA	Poly glycolic acid
PIC	Polyion complex micelles
PLA	Poly lactic acid
PLGA	Polylactic glycolic acid
PLL	Poly-L-lysine
PTEN	Phosphatase and tensin homolog
QDs	Quantum dots
RRM2	M2 subunit of ribonucleotide reductase
RVG29	Peptide derived from the glycoprotein of rabies virus
SDS	Sodium dodecyl sulfate
shRNA	Short hairpin RNA
siRNA	Small interfering RNA
SLNs	Solid lipid Nanoparticles
SPIONs	Super paramagnetic iron oxide Nanoparticles
ss-DNA	Single-stranded DNA
SWNTs	Single-walled carbon nanotubes

REFERENCES

1. Dizaj, S. M., Jafari, S., Khosroushahi, A. Y., "A Sight on the Current Nanoparticle-Based Gene Delivery Vectors", ***Nanoscale Research Letters***, Vol. 9, No. 1, (2014), 252. https://doi.org/10.1186/1556-276X-9-252
2. Ramamoorth, M., Narvekar, A., "Non Viral Vectors in Gene Therapy- an Overview", ***Journal of Clinical and Diagnostic Research: JCDR***, Vol. 9, No. 1, (2015), GE01-GE06. https://doi.org/10.7860/jcdr/2015/10443.5394
3. Mahato, M., Sharma, A. K., Kumar, P., "4 - Nanoparticles for DNA Delivery", In Nimesh, S., Chandra, R., Gupta, N. (eds.), ***Advances in Nanomedicine for the Delivery of Therapeutic Nucleic Acids***, Woodhead Publishing, (2017), 59-81. https://doi.org/10.1016/B978-0-08-100557-6.00004-3
4. Chen, J., Guo, Z., Tian, H., Chen, X., "Production and Clinical Development of Nanoparticles for Gene Delivery", ***Molecular Therapy-Methods and Clinical Development***, Vol. 3, (2016), 16023. https://doi.org/10.1038/mtm.2016.23
5. Hendriks, W. T., Ruitenberg, M. J., Blits, B., Boer, G. J., Verhaagen, J., "Viral Vector-Mediated Gene Transfer of Neurotrophins to Promote Regeneration of the Injured Spinal Cord", ***Progress in Brain Research***, Vol. 146, (2004), 451-476. https://doi.org/10.1016/S0079-6123(03)46029-9
6. Kher, G., Trehan, S., Misra, A., "7 - Antisense Oligonucleotides and RNA Interference", ***Challenges in Delivery of Therapeutic Genomics and Proteomics***, (2011), 325-386. https://doi.org/10.1016/B978-0-12-384964-9.00007-4
7. Lin, G., Zhang, H., Huang, L., "Smart Polymeric Nanoparticles for Cancer Gene Delivery", ***Molecular Pharmaceutics***, Vol. 12, No. 2, (2015), 314-321. https://doi.org/10.1021/mp500656v

8. Nourim, N., Talebi, M., Palizban, A. A., "Viral and Nonviral Delivery Systems for Gene Delivery", ***Advanced Biomedical Research***, Vol. 1, (2012), 27. https://doi.org/10.4103/2277-9175.98152
9. Choi, Y. S., Lee, M. Y., David, A. E., Park, Y. S., "Nanoparticles for Gene Delivery: Therapeutic and Toxic Effects", ***Molecular & Cellular Toxicology***, Vol. 10, No. 1, (2014), 1-8. https://doi.org/10.1007/s13273-014-0001-3
10. Nitta, S. K., Numata, K., "Biopolymer-Based Nanoparticles for Drug/Gene Delivery and Tissue Engineering", ***International Journal of Molecular Sciences***, Vol. 14, No. 1, (2013), 1629-1654. https://doi.org/10.3390/ijms14011629
11. Ghanbari, M., Salavati-Niasari, M., Mohandes, F., Dolatyar, B., Zeynali, B., "In Vitro Study of Alginate–Gelatin Scaffolds Incorporated with Silica Nanoparticles as Injectable, Biodegradable Hydrogels", ***RSC Advances***, Vol. 11, No. 27, (2021), 16688-16697. https://doi.org/10.1039/D1RA02744A
12. Riley, M. K., Vermerris, W., "Recent Advances in Nanomaterials for Gene Delivery-a Review", ***Nanomaterials***, Vol. 7, No. 5, (2017), 94. https://doi.org/10.3390/nano7050094
13. Ghanbari, M., Salavati-Niasari, M., Mohandes, F., "Thermosensitive Alginate–Gelatin–Nitrogen-Doped Carbon Dots Scaffolds as Potential Injectable Hydrogels for Cartilage Tissue Engineering Applications", ***RSC Advances***, Vol. 11, No. 30, (2021), 18423-18431. https://doi.org/10.1039/D1RA01496J
14. Bolhassani, A., Javanzad, S., Saleh, T., Hashemi, M., Aghasadeghi, M. R., Sadat, S. M., "Polymeric Nanoparticles: Potent Vectors for Vaccine Delivery Targeting Cancer and Infectious Diseases", ***Human Vaccines & Immunotherapeutics***, Vol. 10, No. 2, (2014), 321-332. https://doi.org/10.4161/hv.26796
15. Abbasi, E., Aval, S. F., Akbarzadeh, A., Milani, M., Nasrabadi, H. T., Joo, S. W., Hanifehpour, Y., Nejati-Koshki, K., Pashaei-Asl, R., "Dendrimers: Synthesis, Applications, and Properties", ***Nanoscale Research Letters***, Vol. 9, No. 1, (2014), 247. https://doi.org/10.1186/1556-276x-9-247
16. Ghanbari, M., Sadjadinia, A., Zahmatkesh, N., Mohandes, F., Dolatyar, B., Zeynali, B., Salavati-Niasari, M., "Synthesis and Investigation of Physicochemical Properties of Alginate Dialdehyde/Gelatin/Zno Nanocomposites as Injectable Hydrogels", ***Polymer Testing***, Vol. 110, (2022), 107562. https://doi.org/10.1016/j.polymertesting.2022.107562
17. Cao, Y., Moniri Javadhesari, S., Mohammadnejad, S., khodadustan, E., Raise, A., and Akbarpour, M.R., "Microstructural Characterization and Antibacterial Activity of Carbon Nanotube Decorated with Cu Nanoparticles Synthesized by a Novel Solvothermal Method", ***Ceramics International***, Vol. 47, No. 18, (2021), 25729-25737. https://doi.org/10.1016/j.ceramint.2021.05.299
18. Eshghinejad, P., Farnoush, H., "Mechanical Properties of Electrophoretically Deposited 45S5 Bioglass-Graphene Oxide Composite Coatings", ***Advanced Ceramics Progress***, Vol. 5, No. 4, (2019), 17-23. https://doi.org/10.30501/acp.2019.103586
19. Campani, V., Giarra, S., De Rosa, G., "Lipid-Based Core-Shell Nanoparticles: Evolution and Potentialities in Drug Delivery", ***OpenNano***, Vol. 3, (2018), 5-17. https://doi.org/10.1016/j.onano.2017.12.001
20. Chen, F., Ehlerding, E. B., Cai, W., "Theranostic Nanoparticles", ***Journal of Nuclear Medicine***, Vol. 55, No. 12, (2014), 1919-1922. https://doi.org/10.2967/jnumed.114.146019
21. Morimoto, K., Nishikawa, M., Kawakami, S., Nakano, T., Hattori, Y., Fumoto, S., Yamashita, F., Hashida, M., "Molecular Weight-Dependent Gene Transfection Activity of Unmodified and Galactosylated Polyethyleneimine on Hepatoma Cells and Mouse Liver", ***Molecular Therapy***, Vol. 7, No. 2, (2003), 254-261. https://doi.org/10.1016/s1525-0016(02)00053-9
22. Yanat, M., Schroën, K., "Preparation Methods and Applications of Chitosan Nanoparticles; with an Outlook toward Reinforcement of Biodegradable Packaging", ***Reactive and Functional Polymers***, Vol. 161, (2021), 104849. https://doi.org/10.1016/j.reactfunctpolym.2021.104849
23. ***Polyethylenimine***, (2022). Available at: https://en.wikipedia.org/wiki/Polyethylenimine (Accessed: 20 August 2022)
24. ***Chitosan***, (2022). Available at: https://en.wikipedia.org/wiki/Chitosan (Accessed: 23 August 2022)
25. Kim, J. K., Choi, S. H., Kim, C. O., Park, J. S., Ahn, W. S., Kim, C. K., "Enhancement of Polyethylene Glycol (PEG)-Modified Cationic Liposome-Mediated Gene Deliveries: Effects on Serum Stability and Transfection Efficiency", ***Journal of Pharmacy and Pharmacology***, Vol. 55, No. 4, (2003), 453-460. https://doi.org/10.1211/002235702928
26. Pantarotto, D., Singh, R., McCarthy, D., Erhardt, M., Briand, J. P., Prato, M., Kostarelos, K., Bianco, A., "Functionalized Carbon Nanotubes for Plasmid DNA Gene Delivery", ***Angewandte Chemie International Edition***, Vol. 43, No. 39, (2004), 5242-5246. https://doi.org/10.1002/anie.200460437
27. An, H., Jin, B., "Prospects of Nanoparticle–DNA Binding and Its Implications in Medical Biotechnology", ***Biotechnology Advances***, Vol. 30, No. 6, (2012), 1721-1732. https://doi.org/10.1016/j.biotechadv.2012.03.007
28. Abarca-Cabrera, L., Fraga-García, P., Berensmeier, S., "Bio-Nano Interactions: Binding Proteins, Polysaccharides, Lipids and Nucleic Acids onto Magnetic Nanoparticles", ***Biomaterials Research***, Vol. 25, No. 12, (2021), 1-18. https://doi.org/10.1186/s40824-021-00212-y
29. Gaylord, B. S., Heeger, A. J., Bazan, G. C., "DNA Detection Using Water-Soluble Conjugated Polymers and Peptide Nucleic Acid Probes", ***Proceedings of the National Academy of Sciences***, Vol. 99, No. 17, (2002), 10954-10957. https://doi.org/10.1073/pnas.162375999
30. Basu, S., Jana, S., Pande, S., Pal, T., "Interaction of DNA Bases with Silver Nanoparticles: Assembly Quantified through SPRS and SERS", ***Journal of Colloid and Interface Science***, Vol. 321, No. 2, (2008), 288-293. https://doi.org/10.1016/j.jcis.2008.02.015
31. Rahban, M., Divsalar, A., Saboury, A. A., Golestani, A., "Nanotoxicity and Spectroscopy Studies of Silver Nanoparticle: Calf Thymus DNA and K562 as Targets", ***The Journal of Physical Chemistry C***, Vol. 114, No. 13, (2010), 5798-5803. https://doi.org/10.1021/jp910656g
32. An, H., Jin, B., "DNA Exposure to Buckminsterfullerene (C60): Toward DNA Stability, Reactivity, and Replication", ***Environmental Science and Technology***, Vol. 45, No. 15, (2011), 6608-6616. https://doi.org/10.1021/es2012319
33. An, H., Liu, Q., Ji, Q., Jin, B., "DNA Binding and Aggregation by Carbon Nanoparticles", ***Biochemical and Biophysical Research Communications***, Vol. 393, No. 4, (2010), 571-576. https://doi.org/10.1016/j.bbrc.2010.02.006
34. Zhang, Y., Showalter, A. M., "CRISPR/Cas9 Genome Editing Technology: A Valuable Tool for Understanding Plant Cell Wall Biosynthesis and Function", ***Frontiers in Plant Science***, Vol. 11, (2020), 589517. https://doi.org/10.3389/fpls.2020.589517
35. Duan, L., Ouyang, K., Xu, X., Xu, L., Wen, C., Zhou, X., Qin, Z., Xu, Z., Sun, W., Liang, Y., "Nanoparticle Delivery of CRISPR/Cas9 for Genome Editing", ***Frontiers in Genetics***, Vol. 12, (2021), 673286. https://doi.org/10.3389/fgene.2021.673286
36. Mirón-Barroso, S., Domènech, E. B., Trigueros, S., "Nanotechnology-Based Strategies to Overcome Current Barriers in Gene Delivery", ***International Journal of Molecular Sciences***, Vol. 22, No. 16, (2021), 8537. https://doi.org/10.3390/ijms22168537
37. Ginn, S. L., Alexander, I. E., Edelstein, M. L., Abedi, M. R., Wixon, J., "Gene Therapy Clinical Trials Worldwide to 2012–an Update", ***The Journal of Gene Medicine***, Vol. 15, No. 2, (2013), 65-77. https://doi.org/10.1002/jgm.2698
38. Zeng, L., Li, J., Wang, Y., Qian, C., Chen, Y., Zhang, Q., Wu, W.,

Lin, Z., Liang, J., Shuai, X., Huang, K., "Combination of SiRNA-Directed Kras Oncogene Silencing and Arsenic-Induced Apoptosis Using a Nanomedicine Strategy for the Effective Treatment of Pancreatic Cancer", ***Nanomedicine: Nanotechnology, Biology and Medicine***, Vol. 10, No. 2, (2014), 463-472. https://doi.org/10.1016/j.nano.2013.08.007

39. Chen, H., Wang, L., Yu, Q., Qian, W., Tiwari, D., Yi, H., Wang, A. Y., Huang, J., Yang, L., Mao, H., "Anti-HER2 Antibody and ScFvEGFR-Conjugated Antifouling Magnetic Iron Oxide Nanoparticles for Targeting and Magnetic Resonance Imaging of Breast Cancer", ***International Journal of Nanomedicine***, Vol. 8, No. 1, (2013), 3781-3794. https://doi.org/10.2147/IJN.S49069
40. Alphandéry, E., "Iron Oxide Nanoparticles for Therapeutic Applications", ***Drug Discovery Today***, Vol. 25, No. 1, (2020), 141-149. https://doi.org/10.1016/j.drudis.2019.09.020
41. Majidi, S., Zeinali Sehrig, F., Samiei, M., Milani, M., Abbasi, E., Dadashzadeh, K., Akbarzadeh, A., "Magnetic Nanoparticles: Applications in Gene Delivery and Gene Therapy", ***Artificial Cells, Nanomedicine, and Biotechnology***, Vol. 44, No. 4, (2016), 1186-1193. https://doi.org/10.3109/21691401.2015.1014093
42. Carvalho, A. M., Cordeiro, R. A., Faneca, H., "Silica-Based Gene Delivery Systems: From Design to Therapeutic Applications", ***Pharmaceutics***, Vol. 12, No. 7, (2020), 649. https://www.mdpi.com/1999-4923/12/7/649
43. Rezvantalab, S., Drude, N. I., Moraveji, M. K., Güvener, N., Koons, E. K., Shi, Y., Lammers, T., Kiessling, F., "PLGA-Based Nanoparticles in Cancer Treatment", ***Frontiers in Pharmacology***, Vol. 9, (2018), 1260. https://doi.org/10.3389/fphar.2018.01260
44. Jayakumar, R., Chennazhi, K. P., Muzzarelli, R. A. A., Tamura, H., Nair, S. V., Selvamurugan, N., "Chitosan Conjugated DNA Nanoparticles in Gene Therapy", ***Carbohydrate Polymers***, Vol. 79, No. 1, (2010), 1-8. https://doi.org/10.1016/j.carbpol.2009.08.026
45. Prabha, S., Arya, G., Chandra, R., Ahmed, B., Nimesh, S., "Effect of Size on Biological Properties of Nanoparticles Employed in Gene Delivery", ***Artificial Cells, Nanomedicine, and Biotechnology***, Vol. 44, No. 1, (2016), 83-91. https://doi.org/10.3109/21691401.2014.913054
46. Huang, Y. W., Cambre, M., Lee, H. J., "The Toxicity of Nanoparticles Depends on Multiple Molecular and Physicochemical Mechanisms", ***International Journal of Molecular Sciences***, Vol. 18, No. 12, (2017), 2702. https://doi.org/10.3390/ijms18122702
47. Bahadar, H., Maqbool, F., Niaz, K., Abdollahi, M., "Toxicity of Nanoparticles and an Overview of Current Experimental Models", ***Iranian Biomedical Journal***, Vol. 20, No. 1, (2016), 1-11. https://doi.org/10.7508/ibj.2016.01.001

AIMS AND SCOPE

Advanced Ceramics Progress (ACERP) as an ISC international journal is devoted to elucidating the fundamental aspects of chemistry and physics occurring at a wide range of oxide and nonoxide ceramics and composite materials and their processing, microstructure, properties, and applications. The journal provides a unique venue for publishing new exciting research, focusing on dynamic growth areas in this field.

INSTRUCTIONS FOR AUTHORS

Submission of manuscript represents that it has neither been published nor submitted for publication elsewhere and is result of research carried out by author(s).
Authors are required to include a list describing all the symbols and abbreviations in the manuscript. Use of the international system of measurement units is mandatory.

- On-line submission of manuscripts results in faster publication process and is recommended. Instructions are given in the ACERP web site: www.acerp.ir
- References should be numbered in brackets and appear in sequence through the text. List of references should be given at the end of the manuscript.
- Figures' captions are to be indicated under the illustrations. They should sufficiently explain the figures.
- Illustrations should appear in their appropriate places in the text.
- Tables and diagrams should be submitted in a form suitable for reproduction.
- Photographs and figures should be of high quality saved as jpg files (resolution > 600 dpi).
- Tables, illustrations, figures and diagrams will be normally printed in single column width (8 cm). Exceptionally large ones may be printed across two columns (17 cm).

PAGE CHARGES AND REPRINTS

ACERP subscribers do not need to make any payment for publication and reprints.

AUTHORS CHECKLIST

- Author(s), bio-data including academic degree, affiliation(s), ORCiD(s), and e-mail addresses.
- Manuscript including title, abstract, key words, illustrations, tables with tables' captions, figures with figures' captions, acknowledgement, and list of references.
- MS Word files of the manuscript in the ACERP template and all figures (resolution > 600 dpi).
- Similarity check of the manuscript, copyright forms, and conflict of interest forms

Advanced **Cer**amics **P**rogress,
P.O. Box 31787-316, Meshkin Dasht, Alborz, I. R. Iran
Materials and Energy Research Center, Imam Khomeini Blvd, Meshkin Dasht, Alborz, I. R. of Iran
P.O. Box 14155-4777, Tehran, I. R. Iran
No. 5, Ahuramazda St., Alvand Ave., Argentine Sq., Tehran, Tehran, I. R. of Iran

www.merc.ac.ir - www.icers.ir

Advanced Ceramics Progress

Volume 8, Number 1, Winter 2022

CONTENTS

Journal Home Page: www.acerp.ir